NORTHWESTERN UNIVERSITY

Design and Development of Biomarker-Responsive Transition Metal-Based Magnetic Resonance Imaging Probes

A DISSERTATION

SUBMITTED TO THE GRADUATE SCHOOL
IN PARTIAL FULFILLMENT OF THE REQUIREMENTS

for the degree

DOCTOR OF PHILOSOPHY

Field of Chemistry

By

Kang Du

EVANSTON, ILLINOIS

December 2018

ABSTRACT

Design and Development of Biomarker-Responsive Transition Metal-Based Magnetic Resonance Imaging Probes

Kang Du

The invention of Gd^{III}-based magnetic resonance imaging (MRI) probes substantially expanded the capability of MRI in visualizing details in tissue. Building upon the achievement of Gd^{III}-based complexes, more ideal probes should feature contrast that is responsive to biomarkers, such as redox status and ion concentrations. The abnormality of these biomarkers are oftentimes associated with pathologies. Importantly, the responsive contrast from these probes should be independent of the local probe concentration, in order to avoid ambiguity caused by uneven bio-distribution of the probes, and enable quantitative measurement of the biomarkers.

Transition metal complexes are attractive candidates for responsive MRI probes, due to the highly tunable magnetic and electronic properties of transition metals. This dissertation reports the development of transition metal-based MRI probes for ratiometric quantitation of biomarkers. Chapter One provides a brief introduction of paramagnetic chemical exchange saturation transfer (PARACEST) and the advantages and design criteria of PARACEST probes. Chapter Two describes a case study in which a Cu^{II}_2 PARACEST probe was enabled by magnetic coupling. Such result suggests that magnetic coupling can reduce electronic relaxation time (τ_s), allowing a much broader range of metals to be considered for PARACEST probes. Building on the strategy developed in Chapter Two, Chapter Three demonstrates that a Fe_2 probe, which is NMR-active in both the $Fe^{II}Fe^{II}$ and $Fe^{II}Fe^{III}$ states, can quantitate solution redox status in a concentration-independent manner. Chapter Four applies the magnetic coupling strategy to reduce the intrinsic

relaxivity of Gd^{III} complexes by decreasing the τ_s of the Gd^{III} center. This study forms the foundation for designing responsive Gd^{III}-based probes with low background signals. In addition to manipulating the electronic properties of transition metals, Chapter Five demonstrates the utilization of the magnetic anisotropy of Co^{II} to distinguish Ca^{2+} and Na^{+} in solution. The resulting Ca^{2+} to Na^{+} CEST intensity ratio provides a concentration-independent parameter for quantitating Ca^{2+}, which is a prominent biomarker for bone-related diseases.

ACKNOWLEDGEMENT

I would like to first thank Prof. Dave Harris for accepting me into his group. I learned a lot about synthetic inorganic techniques from Dave either through his demonstration or from stories he told us. Dave also said many inspirational things, either quoting others or from himself, that I still remember very well. For example “it is curiosity that drive human society forwards” and “a good idea is not most valuable, a person who can turn the idea into reality is most valuable”. Okay, his exact words might have better word choices, but the meanings are surely the same. I also want to thank Prof. Danna Freedman, Prof. Julia Kalow, Prof. Tom O’Halloran and Prof. Chad Mirkin for serving in my defense/qualification committee, from whom I received a lot constructive advices.

I would like to thank Prof. Joe Zadrozny for his friendship, encouragement and inspiration. I was very impressed by Joe’s broad scientific curiosity and his consistent lunch choice (chicken pot pie). Conversations with Joe, the topics of which range from chemistry, physiology to geology, were always inspirational and oftentimes resulted in new directions of projects. Joe is also gifted in making figures. The TOC for Chapter Three includes several of his suggestions.

I also want to thank Dr. Ie-Rang Jeon, who tended to talk to me in French without noticing that it wasn’t English. I remembered Ie-Rang spend hours siting through several of my qualification practices and pointing out that essentially the only thing I wrote correctly was my name. I surely wouldn’t have passed qualification exam without her help.

I am very fortunate to have all the friends from both the Harris and Freedman groups to share both sorrow and joy with in the past six years. So I want to say “thank you” to Dr. Alex Gaudette, Dr. Audrey Gallagher (who is talented in making up nicknames), Prof. John Anderson, Dr. Jordan

DeGayner (who eventually will swim slower than I am), Dr. Jung Yoon Lee, Dr. Luke Liu (world-class crystallographer), Agnes Thorarinsdottir (who will eventually get the Guinness world record for longest supplemental information), Ella Wang, Ben Coleman, Dr. David Zee, Jesse Park, Scott Tatro, Dr. Michael Graham (best roommate), Majed Fataftah (who only had one most insignificant win against me in pingpong), Scott Coste, Dr. Sam Clarke, Ryan Klein, Dr. James Walsh, Tyler Pearson, Raymond Yu, Dr. Allison Altman, Dr. Lei Sun.

Next I want to thank Prof. Tom Meade and his group, Dr. Laura Lilley, Dr. Luke Vistain, Dr. Keith MacRenaris, Dr. Ruby Krueger and everyone else in the group for helpful discussion and assistance in experiments.

I thank Dr. Yongbo Zhang in IMSERC and Dr. Peter Mirau from AFRL for their help and knowledge in NMR.

Last but not least, I certainly wouldn't have accomplished what I did in the past six years without the love and support from my family (Xiaowu Liang, Qinghui Du and Tong Shang). I lost some quality times with them while I was working towards my Ph.D. and I hope I will have better time management to make up for those times. I hope I made them proud.

TABLE OF CONTENTS

LIST OF FIGURES

LIST OF TABLES

Chapter One: Introduction

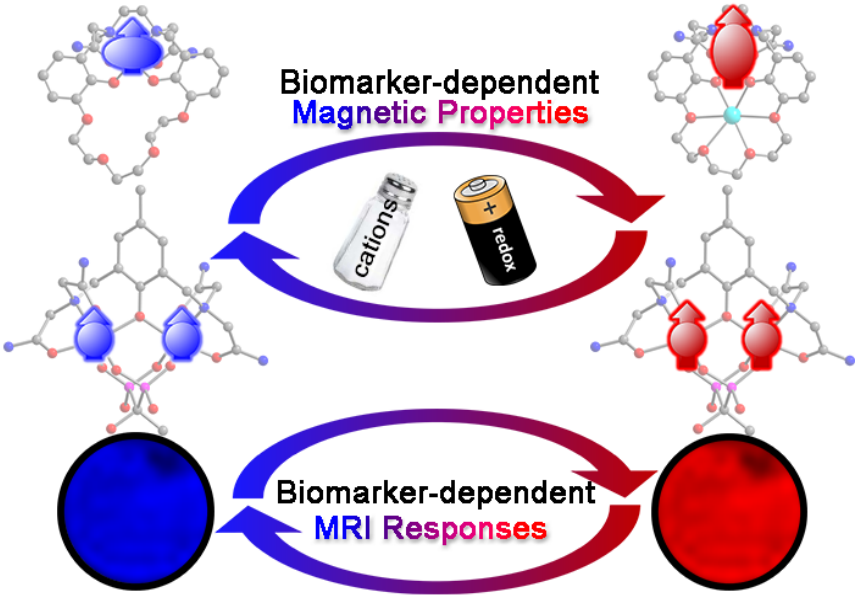

Magnetic resonance imaging (MRI) has become one of the most powerful diagnostic methods in medicine. It is a non-invasive technique with unlimited penetration depth of tissues, capable of generating images with high spatiotemporal resolution.[1] Due to the different abundance of H_2O in various types of tissues, MRI probes are oftentimes administrated to enhance signal. These probes reduce the spin-lattice relaxation time (T_1) of protons on H_2O molecules, leading to more rapid acquisitions and stronger H_2O nuclear magnetic resonance (NMR) signals. The Gd^{III} ion has a well-isolated $S = {}^7/_2$ electronic ground state and long electronic relaxation time ($\tau_s \approx 10^{-9}$ s) at room temperature under 1.5 T (magnetic field for conventional MRI scanners).[2] Because of the nearly-optimal electronic properties of Gd^{III}, clinical MRI probes are predominantly Gd^{III}-based complexes.[3] Several parameters (see Figure 1.1), such as the number of coordinating H_2O (q), rotational time (τ_r) and water residence time (τ_m) have been synthetically tuned by modification of the ligands to maximize the effectiveness of the probes to reduce T_1, as measured by relaxivity, r_1.[4]

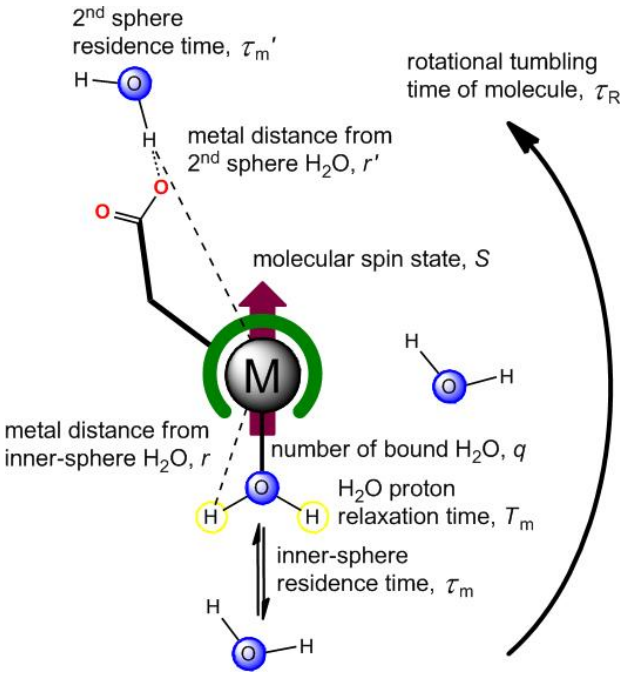

Figure 1.1 A pictorial summary of parameters that can be tuned to optimize the relaxivity of T_1-modulating probes. Figure is from ref. 2b.

Compared to probes with T_1-modulating contrast, another type of probes relies on chemical exchange of protons to generate contrast in H_2O NMR signals.[5] Paramagnetic chemical exchange saturation transfer (PARACEST) probes are paramagnetic molecules with labile protons. Upon presaturation with radiofrequency radiation, these labile protons deliver saturation to H_2O through chemical exchange, resulting in reduced H_2O NMR signal. Hence, H_2O molecules interacting with the probes can be distinguished from those that are isolated from the probes, generating contrast (see Figure 1.2, upper). The hyperfine shifts of these protons are shifted far from the range of diamagnetic compounds, thus avoiding interference from labile protons under physiological conditions and allowing for faster exchange rate, which is limited by the separation in chemical shifts between the H_2O and the labile proton peaks (see Figure 1.2).[6] In a typical chemical exchange saturation transfer (CEST) experiment, the integration of the H_2O signal is plotted

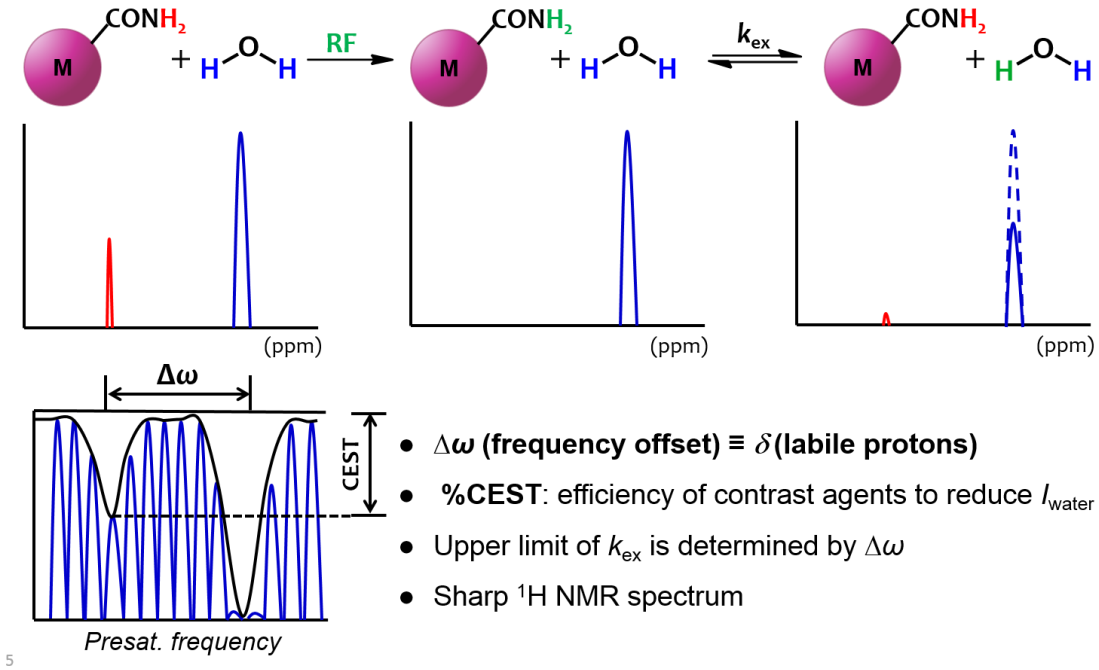

Figure 1.2 Upper: pictorial explanation of how contrast is generated by PARACEST probes. Bottom: illustration of how a CEST spectrum is generated and relevant parameters to characterize the spectrum.

against the presaturation frequency (i.e. frequency offset from the H_2O signal) to give a *Z*-spectrum or CEST spectrum. In general, a CEST spectrum features a near-100% saturation peak, which is attributed to the direct saturation of H_2O, in addition to one or more less intense peaks, which are attributed to labile protons from the PARACEST probe (see Figure 1.2, lower). One major advantage for PARACEST probes is the presaturation frequency-selective contrast, which allows for simultaneous detection of more than one non-overlapping CEST peaks. In addition, because CEST experiments detect H_2O signals, PARACEST probes can be conveniently applied in studies using conventional MRI scanners, which are exclusively tuned to record H_2O NMR signal.

PARACEST probes were first recognized in lanthanide (Ln) chelates, where the H_2O exchange rate was in the slow-to-medium range ($\approx 10^2$–10^4 s^{-1}).[7] Such probes are generally macrocyclic chelates functionalized with negatively charged pendant groups, which primarily serve to reduce both the large positive charge on Ln^{III} and the fast water exchange rate (see Figure 1.3 for examples). Due to the large magnetic moment of most Ln ions, the short Ln···^{1}H distance and optimal exchange rates, CEST peaks from coordinating H_2O molecules on Ln-based PARACEST probes generally have large frequency offsets and significant CEST intensities (as high as 60%).[8] However, because of the predominantly ionic nature of Ln–L bonds, protons that are farther from the Ln center than those on coordinating H_2O molecules, experience minimal hyperfine shift

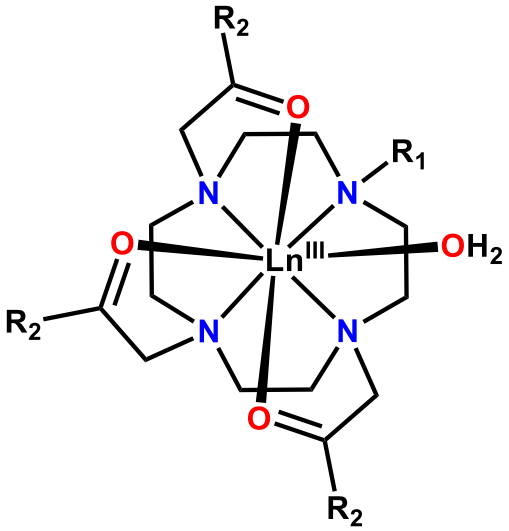

Figure 1.3 A representative molecular structure for Ln-based PARACEST agents with DOTA-based chelates. Ln: Eu, Tb, Dy, Ho, Er, Tm, Yb.

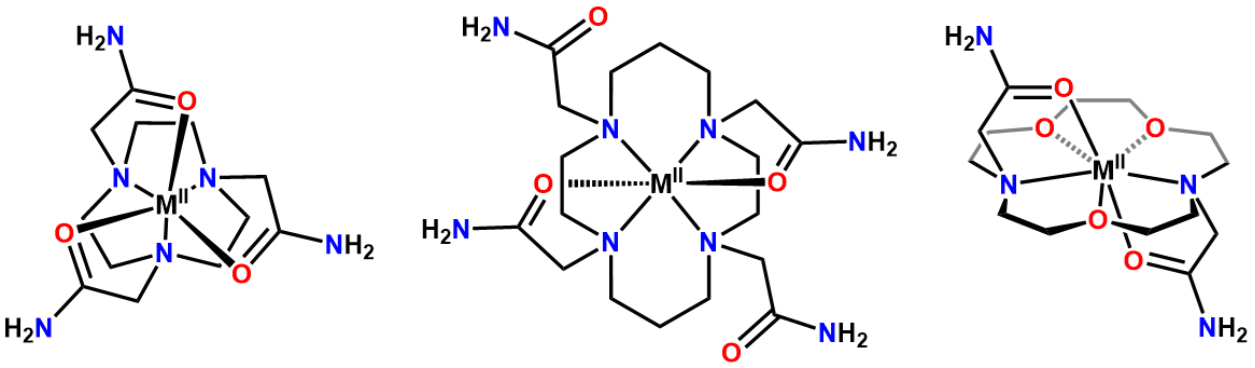

Figure 1. 4 Summary of examples of transition metal-based PARACEST agents. M: Fe, Co and Ni.

induced by the magnetic moment of the Ln center. Such limitation hampers the utilization of any organic functional groups with optimal proton exchange rates for the application of CEST.

To address such challenge, transition metal-based PARACEST probes were developed, with the intent that the more covalent M–L bonds facilitate greater diffused spin densities from the paramagnetic center, expanding the hyperfine shift of labile protons on coordinating ligands. These transition metal-based probes generally feature a macrocyclic chelate functionalized with pendant groups that have labile protons, such as alcohol, carboxyamide, pyrazole and imidazole (see Figure 1.4 for examples).[9] The frequency offsets for some of the CEST peaks are over 100 ppm away from the H_2O signal, highlighting the contribution from the more covalent M–L bonds in expanding hyperfine shift through spin diffusion. More importantly, the shift of the CEST peaks have been shown to be highly dependent on the coordination environment and the magnetic properties of the metal centers in structurally similar probes, highlighting the excellent tunability of transition metal-based PARACEST probes.[10] However, because the presence of sharp ^{1}H NMR peaks is a prerequisite, τ_s of the metal center must be short ($< 10^{-11}$ s).[11] As such, probes containing only high-spin Fe^{II}, Co^{II} and Ni^{II} have been developed (see Figure 1.4 for examples).[9]

While MRI is effective in distinguishing different types of tissues, it is much less effective in

distinguishing abnormalities within the same type of tissue. As such, responsive MRI probes were developed to create contrast based on biological stimuli. Ln-based T_1 modulating or PARACEST probes generally utilize ligand-based sensing, meaning that the conformation or the chemical structure of ligand(s) change upon interacting with the biomarkers, leading to a change in r_1 or CEST intensity, respectively.[10] Eu-based probes are the only exception where a metal-centered $Eu^{II/III}$ couple is utilized to create contrast based on solution redox status.[11] In contrast, the electronic properties of transition metals are highly susceptible toward coordination environment. The resulting magnetic properties of the metal center, e.g. a change in spin state or magnetic anisotropy, can induce more dramatic change in the T_1 or CEST signals, giving rise to highly responsive probes.[12]

Finally, ideal responsive MRI probes should be able to account for the uneven biodistribution of probes or biomarkers to avoid falsified responses. One promising approach is to have more than one signal that have different extent of responses toward a biomarker, so that the ratio between the two signals can provide a concentration-independent measure of the biomarker. PARACEST probes are particularly suited for such ratiometric quantitation strategy, because the frequency-dependent contrast allows simultaneous detection of more than one CEST peak. The challenge becomes how to design probes with non-overlapping CEST peaks that have different dependence on stimulations from biomarkers. Because the choice of transition metal centers is strictly limited, it is equally important to broaden the choice of metals and oxidation states, in order to fully realize the tunability of transition metals in the development of responsive PARACEST probes. The following chapters demonstrate studies to address the above challenges.

Chapter Two: A Cu^{II}_2 PARACEST Contrast Agent Enabled by Magnetic Exchange Coupling

Reprinted with permission from:

Du, K and Harris, T. D. *J. Am. Chem. Soc.* **2016**, *138*, 7804-7807.

This work was performed in collaboration with the co-authors listed above.

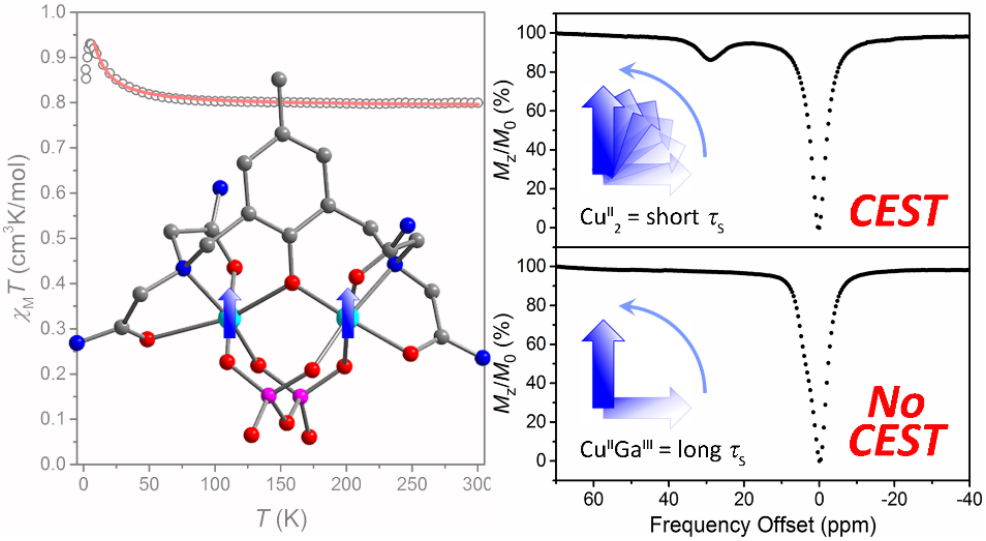

2.1 Introduction

PARACEST magnetic resonance imaging (MRI) contrast agents represent an emerging class of molecules that offer several key advantages over conventional Gd-based proton relaxation agents, including the ability to facilitate on/off contrast switching and an inherent response to environmental parameters such as pH and temperature.[1] The mechanism through which PARACEST agents generate contrast exploits labile ligand protons within close proximity to the paramagnetic center. Here, irradiation at the resonant frequency of the exchangeable protons, along with concomitant chemical exchange of these protons with bulk water protons, induces a suppression of bulk water signal and thus an image darkening.[2] Importantly, the paramagnetic metal imposes a large hyperfine shift on the resonant frequency of the exchangeable protons, so as to minimize interference from resonances associated with surrounding tissue and to permit rapid proton exchange. Despite the potential utility of PARACEST agents, a major fundamental limitation toward their implementation arises due to proton nuclear spin relaxation enhancement induced by paramagnetic metal centers, which leads to spectral broadening and thus low sensitivity and resolution. In order to reduce proton relaxation effects, the electronic relaxation time (τ_s) of the paramagnetic metal must be minimized so that it is not resonant with the proton nuclear spin.[1]

To date, reported PARACEST agents have taken the form of non-Gd lanthanide,[1, 3] and first-row transition metal (Fe^{II}, Co^{II}, Ni^{II}) complexes.[4] These ions display short values of τ_s, typically in the range of 10^{-11} to 10^{-12} s, owing to low-lying excited states that arise from spin-orbit coupling and/or zero-field splitting. Lanthanide PARACEST agents are air-stable and tend to exhibit large hyperfine shifts, as high as 720 ppm vs water,[5] stemming from their large magnetic moments and strong magnetic anisotropy. Nevertheless, these agents rely on through-space pseudocontact shifts

of protons, rather than through-bond contact shifts, due to the contracted 4*f* orbitals,[1] and therefore necessitate placement of exchangeable protons within very close proximity to the metal ion. Moreover, the ionic nature of lanthanides, in conjunction with their redox- and spin-state inertness, limits the design of responsive agents.[1e, 3b, 6] Compared to lanthanide complexes, transition metal PARACEST agents exhibit smaller hyperfine shifts, up to 135 ppm vs water,[4f] but offer much more tunability through coordination and redox chemistry. Indeed, recent work has demonstrated the ability of transition metal ions with short values of τ_s to engender PARACEST agents that are stable under physiological conditions.[4c,d,e] Nevertheless, metal ions with large values of electronic spin and higher oxidative stability, such as $S = {}^5/_2$ Mn^{II} or Fe^{III}, or metal ions that exhibit even more kinetically inert substitution, such as Cr^{III}, are precluded from consideration for PARACEST, as they exhibit long values of $\tau_s = 10^{-8}$ to 10^{-9} s and therefore induce severe NMR line broadening.[7] Taken together, these observations underscore the need for a general strategy to design transition metal-based PARACEST agents with short electronic relaxation times.

A paramagnetic metal ion displays a long τ_s when the electronic ground state is energetically well-isolated from excited states, with no significant zero-field splitting or spin-orbit coupling. A representative example is Cu^{II}, where the d^9, $S = {}^1/_2$ electronic configuration and Jahn-Teller distortion result in a long τ_s of 10^{-8} to 10^{-9} s.[7] Nevertheless, several Cu^{II}_2 complexes with weak magnetic superexchange coupling between metal centers have been shown to exhibit much shorter values, as small as $\tau_s \sim 10^{-11}$ s.[8] As the separation of ground and excited state is correlated to the magnitude of exchange constant *J*, the presence of weak coupling leads to a low-lying excited state that can facilitate fast electronic relaxation and therefore a short τ_s. Moreover, the $S = 1$ ground or excited state, resulting from ferro- or antiferromagnetic coupling, respectively, can possess non-

negligible zero-field splitting that further decreases τ_s and can contribute to increasing the hyperfine shift.[7] Despite the potential of magnetic exchange coupling to serve as a tool to shorten τ_s, no multinuclear transition metal complexes have been reported as PARACEST agents. Herein, we demonstrate the utility of magnetic exchange coupling to enable realization of a Cu^{II}_2 PARACEST agent.

2.2 Experimental Section

General considerations. Unless otherwise specified, chemicals and solvents were purchased from commercial vendors and used without further purification. Deuterated solvents were purchased from Cambridge Isotope Laboratories. When necessary for moisture sensitive experiments, glassware was flame dried or stored in an oven at 150 °C for at least 4 hours, followed by cooling in a desiccator. Air- and water-free manipulations were carried out using standard Schlenk techniques. Acetonitrile was dried using a commercial solvent purification system from Pure Process Technology and stored over 4 Å molecular sieves prior to use. Water was obtained from a purification system from EMD Millipore. Elemental analysis was conducted by Midwest Microlab Inc. Preparative reverse-phase HPLC was performed on a Waters 19 × 250 mm^2 Xbridge C18 Column, using the Varian Prostar 500 system equipped with a Varian 363 fluorescence detector and a Varian 335 UV/Visible Detector. During HPLC, water was used as solvent A and acetonitrile as solvent B. The absorbances at 220 and 285 nm were monitored. Anhydrous hydrogen chloride gas was generated by adding concentrated hydrochloric acid to a stirring solution of concentrated sulfuric acid. The gas was passed through a bubbler filled with sulfuric acid.

Synthesis of 2,6-bis(bromomethyl)-4-methylphenol. This compound was synthesized

following a modified literature procedure.[9] Para-cresol (9.7 g, 0.090 mol) was dissolved in an aqueous solution (18 mL) of sodium hydroxide (4.5 g, 0.11 mol). To this solution was added with stirring a 37% aqueous solution of formaldehyde (18 mL), and the resulting light yellow solution was stirred for 12 hours at ambient temperature to give a white solid precipitate. The solid was collected by filtration and then was dissolved in H_2O (200 mL), and the ensuing solution was adjusted to pH 6 with glacial acetic acid. Upon stirring for 15 minutes, a white solid precipitated and was collected by filtration. This solid was dissolved in a solution of 37% HBr in acetic acid (40 mL). After stirring for 24 h, the resulting mixture was diluted with H_2O (40 mL), stirred for an additional 30 minutes, and then filtered to give the product as an off-white solid (9.0 g, 34%). ^{1}H NMR (MeCN-d_3): 2.24 (s, 3H), 4.61 (s, 4H), 7.15 (s, 2H).

Synthesis of 2, 2′-iminobis(acetamide). This compound was synthesized following a modified literature procedure.[10] Iminodiacetonitrile (5.0 g, 0.053 mol) was suspended in anhydrous isopropanol (100 mL). Anhydrous HCl gas was bubbled into this suspension, and the mixture was stirred at 50 °C for 15 hours. The resulting yellow mixture was then filtered to isolate an off-white solid. The solid was dissolved in H_2O (40 mL), and the solution was adjusted to pH 10 with $(NH_4)OH$. The solution was evaporated to dryness, and the remaining brown solid was dissolved in H_2O (18 mL). The resulting dark brown solution was added to acetone (120 mL) with stirring, giving an off-white precipitate. Upon stirring for 10 minutes, the off-white solid was collected by filtration to give the product as an off-white solid (3.0 g, 45%) ^{1}H NMR (DMSO-d_6): 3.67 (s, 4H), 7.50 (s, 2H), 7.84 (s, 2H).

Synthesis of *N*,*N*′-[(2-hydroxy-5-methyl-1,3-phenylene)bis(methylene)]bis[N-(carboxymethyl)glycinamide] (HL). Under a dinitrogen atmosphere, *N*,*N*-diisopropylethylamine

(1.47 g, 11.4 mmol) and 2,2′-iminobis(acetamide) (1.50 g, 11.4 mmol) were suspended in MeCN (200 mL). The suspension was heated to reflux, and to it was added dropwise with stirring a solution of 2,6-bis(bromomethyl)-4-methylphenol (1.12 g, 3.81 mmol) in MeCN (20 mL) over the course of 24 h to give a dark brown slurry. The reaction mixture was evaporated to dryness, and the remaining brown residue was dissolved in a 10% aqueous MeOH solution (18 mL) and subsequently purified by C18 reverse-phase HPLC using H_2O and MeCN as eluents. Evaporation of the resulting solution gave HL as an off-white solid (0.205 g, 13%). ESI-MS: 395.101 ($M+H^+$). ^{1}H NMR (MeOH-d_4): 2.23 (s, 3H), 3.35 (s, 8H), 3.82 (s, 4H), 6.96 (s, 2H). UV-Vis absorption spectrum: 285 nm (ε = 2660 M^{-1} cm^{-1}). FT-IR (ATR, cm^{-1}): 3172 (m, broad); 1674 (s); 1648 (s); 1598 (m); 1480 (m); 1411 (m); 1340 (m); 1254 (m); 1209 (m); 1111 (m); 1009 (m); 859 (m); 786 (m).

Synthesis of H[LCu$_2$(P$_2$O$_7$)]·0.5KNO$_3$·3H$_2$O (1). $Cu(NO_3)_2 \cdot 3H_2O$ (12 mg, 0.051 mmol) was dissolved in H_2O (0.5 mL), and the resulting solution was added to a stirring solution of HL (10 mg, 0.025 mmol) in H_2O (0.5 mL) to give a brown solution. The solution was stirred for 15 minutes, and then a solution of $K_4(P_2O_7)$ (8.4 mg, 0.025 mmol) in H_2O (0.5 mL) was added. After an additional 15 minutes of stirring, the pH of the brown solution was adjusted to 7 through addition of a ca. 5% aqueous KOH solution. The ensuing brown solution was stirred for 30 minutes and then filtered through a 0.22 μm nylon membrane. Slow evaporation of the resulting brown solution gave brown plate-shaped crystals of **1** (11 mg, 37%) suitable for single-crystal X-ray diffraction analysis. UV-Vis absorption spectrum: 302 nm (ε = 4470 M^{-1} cm^{-1}), 432 nm (ε = 742 M^{-1} cm^{-1}), 771 nm (ε = 107 M^{-1} cm^{-1}). FT-IR (ATR, cm^{-1}): 3154 (m, broad); 1667 (s); 1614 (s); 1476 (m); 1350 (s); 1317 (s); 1278 (w); 1093 (s); 1020 (m); 876 (m); 803 (w). Due to the co-

crystallization of small but inconsistent impurities of KNO_3, satisfactory elemental analysis could not be obtained for **1**. However, addition of EtOH (5 mL) to a stirred concentrated (0.5 mL) brown solution of crystallization from above gave $K[LCu_2(P_2O_7)]\cdot 3KNO_3\cdot 4H_2O\cdot 0.6EtOH$ as a light brown precipitate. Anal. Calcd. for $C_{18.2}H_{36.6}Cu_2N_9O_{25.6}P_2K_4$: C, 19.23; H, 3.25; N, 11.09. Found: C, 19.21; H, 2.63; N, 10.59.

Synthesis of LCuGaL′·4NaNO₃·7.1EtOH (2) $Ga(NO_3)_3\cdot H_2O$ (10 mg, 0.038 mmol) was dissolved in H_2O (0.5 mL), and the resulting solution was added to a stirring solution of HL (15 mg, 0.038 mmol) in H_2O (0.5 mL) to give a pale yellow solution. $Cu(NO_3)_2\cdot 3H_2O$ (9.2 mg, 0.038 mmol) in H_2O (1.0 mL) was added to the above solution dropwise. The light brown solution was stirred for 15 minutes, and then a solution of $Na(H_3L')\cdot 3H_2O$ (12 mg, 0.038 mmol) in H_2O (0.5 mL) was added. After an additional 15 minutes of stirring, the pH of the brown solution was adjusted to 7 through addition of a ca. 5% aqueous NaOH solution. The ensuing brown solution was stirred for 30 min and then filtered through a 0.22 μm nylon membrane. The filtrate was concentrated under reduced pressure to a volume of 0.5 mL, addition of EtOH (5 mL) to this solution with stirring gave **2** (13 mg, 23%) as a yellow precipitate. Anal. Calcd. for $C_{35.2}H_{77.6}CuGaN_{12}O_{34.1}P_2Na_4$: C, 28.15; H, 5.21; N, 11.19. Found: C, 27.80; H, 4.33; N, 10.85. UV-Vis absorption spectrum: 363 nm (ε = 1070 $M^{-1}\,cm^{-1}$), 418 nm (ε = 297 $M^{-1}\,cm^{-1}$), 784 nm (ε = 75 $M^{-1}\,cm^{-1}$). FT-IR (ATR, cm^{-1}): 3154 (m, broad); 1667 (s); 1614 (s); 1483 (s); 1448 (w); 1319 (s); 1279 (w); 1116 (s); 1070 (s); 999 (m); 875 (m); 815 (w).

X-ray structure determination. A single crystal of **1** was directly coated with Paratone-N oil and mounted on a MicroMounts™ rod. The crystallographic data were collected at 100 K on a Bruker APEX II diffractometer equipped with MoKα sealed tube source. Raw data were integrated

and corrected for Lorentz and polarization effects using Bruker APEX2 v. 2009.1.[11] The program SADABS was use to apply absorption correction.[12] Space group assignments were determined by examining systematic absences, E-statistics and successive refinement of the structure. Structures were solved by SHELXT using direct methods and refined by SHELXL within the OLEX interface.[13, 14] H_2O solvent molecules were severely disordered and could not be modeled properly. Therefore, the program SQUEEZE, a component of PLATON,[15] was used to calculate solvent disorder area. A total of 25 H_2O molecules were estimated based on 251 electrons in a void volume of 665.1 $Å^3$. Partially occupied solvent H_2O molecules that were potentially hydrogen bonded were not considered by SQUEEZE and therefore were modeled isotropically. Thermal parameters for all other non-hydrogen were refined anisotropically.

^{1}H NMR experiments. Variable temperature ^{1}H NMR spectra were collected on an Agilent DD2 500 MHz (11.75 T) system. T_1 and T_2 values were obtained from the preset pulse sequence in the program *vnmr* and processed by the program MNOVA.

CEST experiments. Variable temperature CEST experiments were performed on an Agilent DD2 500 MHz (11.75 T) system. Samples containing 10 mM of **1** and 30 mM of **2** in 50 mM of HEPES at pH 7 were used for CEST experiments. Z-spectra (CEST spectra) were obtained according to the following protocol. NMR spectra were acquired using the presaturation pulse applied for 2 s at a power level of 21 μT. The saturation frequency offsets were screened with a step increase of 0.4 ppm. The obtained NMR spectra were plotted as normalized water intensity against frequency offset to produce a Z-spectrum. Direct saturation of the water signal was set to 0 ppm. D_2O was placed in an inner capillary to lock the sample. Exchange rate constants were calculated based off a reported method.[16] The NMR spectra were acquired at various presaturation

powers ranging from 7.4 to 21 μT applied for 5 s.

Magnetic measurements. Magnetic measurements of **1** in a 92.5 mM 1:1 H_2O/glycerol solution were carried out using a Quantum Design MPMS-XL SQUID magnetometer. Absorption spectra of **1** in H_2O and in 1:1 H_2O/glycerol confirmed the preservation of the structure of **1** in both solvents (see Figure 2.11). While the diamagnetic contribution from the solvent matrix is difficult to accurately determine, we can assume that the coupling between the two Cu^{II} centers is insignificant at high temperature. Therefore, the diamagnetic correction was adjusted to set the value of $\chi_M T$ to be constant in the temperature range 150-300 K. In addition, using this assumption, the number of moles of **1** was determined through an independent measure of the *g* tensor using EPR (see Figure 2.12). This method enables us to eliminate mass errors introduced during the preparation of such a small sample.

Electron paramagnetic resonance experiments. Continuous-wave EPR data were collected on a frozen glass of **1** in 6.78 mM 1:1 H_2O/glycerol at 77 K on a Bruker Elexsys 500 X-band spectrometer at the University of Chicago EPR facility. Spectra were acquired with the Bruker Win-EPR software suite. The spectrometer was equipped with a dual mode cavity, operating in parallel mode.

Cyclic voltammetry. Cyclic voltammetry was carried out in a standard one-compartment cell in air at ambient temperature, equipped with a glassy carbon working electrode, a platinum wire as counter electrode, and a Ag/AgCl in saturated KCl solution reference electrode using a CHI 760c potentiostat. The analyte solution was prepared with 0.1 M $NaClO_4$ aqueous solution at pH 7. The voltammogram was converted and shown as values referred to the normal hydrogen electrode (NHE), using a literature conversion factor.[17]

UV-Visible spectral titrations. Spectral titration experiments were carried out on an Agilent Cary 5000 UV/Vis/NIR spectrometer. In general, 2 μL increments of an aqueous stock solution of $Cu(NO_3)_2 \cdot 3H_2O$ and $K_4(P_2O_7)$ were added to a 3 mL solution of HL. Each spectrum was acquired after stirring for 3 min following each addition. The absorbance value was corrected for the change of volume of the sample by the addition of a stock solution. Typical starting samples for dinuclear complexes contained 0.317 mM of HL or 0.317 mM of HL + 0.634 mM of $Cu(NO_3)_2 \cdot 3H_2O$ in 5 mM HEPES at pH 7. Typical stock solutions contained 50.1 mM of Cu^{2+} in deionized water or 48.8 mM of $K_4(P_2O_7)$ in 5 mM HEPES pH 7. The titration data for the dissociation constant of $(P_2O_7)^{4-}$ were fitted by the program Dynafit[18]

2.3 Results and Discussion

Dinuclear Cu^{II}_2 complexes supported by a phenoxo-centered tetrapyridyl ligand have previously been shown to exhibit solubility and stability in aqueous solution and weak magnetic exchange coupling of $|J| \leq 25$ cm^{-1}.[19] Building from these results, we targeted the analogous tetra(carboxamide) ligand HL, with the intent that the carboxamide groups could provide CEST-active protons (see Figure 2.1). This ligand was synthesized through an S_N2 reaction between 2,2′-iminodiacetamide and 2,6-bis(bromomethyl)-4-methylphenol. As for the ancillary ligand,

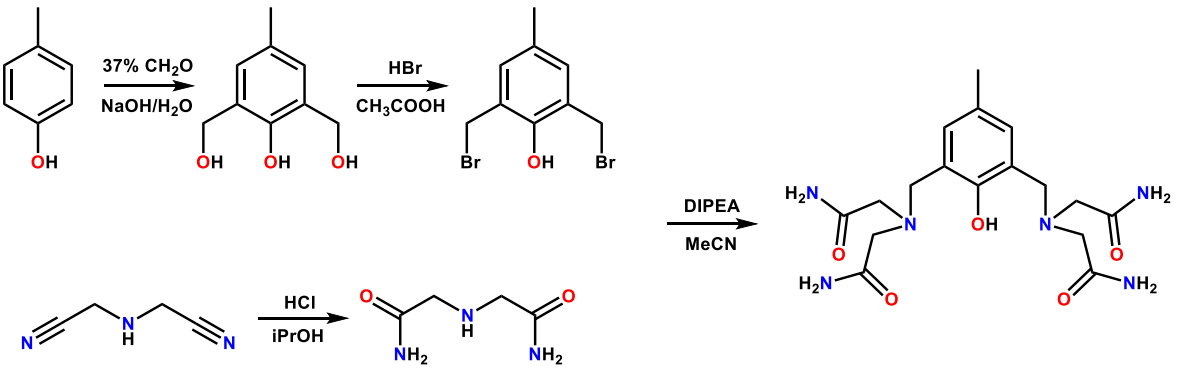

Figure 2.1 Synthesis of precursors and HL.

pyrophosphate, $(P_2O_7)^{4-}$, was selected owing to its tendency to coordinate metal ions with higher thermodynamic stability than do water and coordinating anions in aqueous solution.[20] Reaction of two equiva-lents of $Cu(NO_3)_2 \cdot 3H_2O$ with one equivalent each of HL and $K_4(P_2O_7)$ in water gave rise to a brown solution. Subsequent slow evaporation of this solution afforded brown plate-shaped crystals of $H[LCu_2(P_2O_7)] \cdot 0.5KNO_3 \cdot 3H_2O$ (**1**) that were suitable for single-crystal X-ray diffraction analysis. To provide a related uncoupled Cu-containing complex for comparison to **1**, an analogous GaCu complex was synthesized. Here, HL was selectively metalated with one equivalent of $Ga(NO3)_3 \cdot H_2O$, followed by addition of one equivalent each of $Cu(NO_3)_2 \cdot 3H_2O$ and $Na(H_3L') \cdot 3H_2O$ (H_4L' = alendronic acid), to give $LGaCuL' \cdot 4NaNO_3 \cdot 7.1EtOH$ (**2**; see Figure 2.2, right). In the synthesis of **2**, tetraanionic alendronate was employed as the ancillary ligand in place of $(P_2O_7)^{4-}$ in order to impart water solubility to the neutral complex.

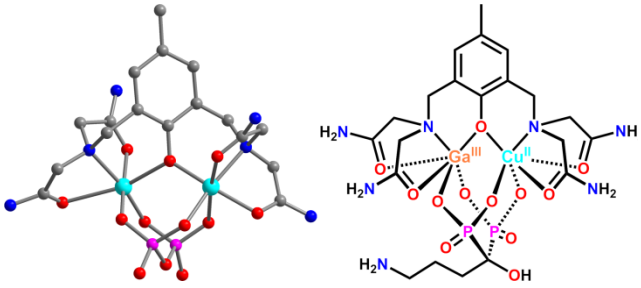

Figure 2.2 Left: Crystal structure of $[LCu_2(P_2O_7)]^-$, as observed in **1**. Cyan, pink, red, blue, and gray spheres represent Cu, P, O, N, and C atoms, respectively; H atoms are omitted for clarity. Right: Molecular structure of LGaCuL′, as observed in **2**.

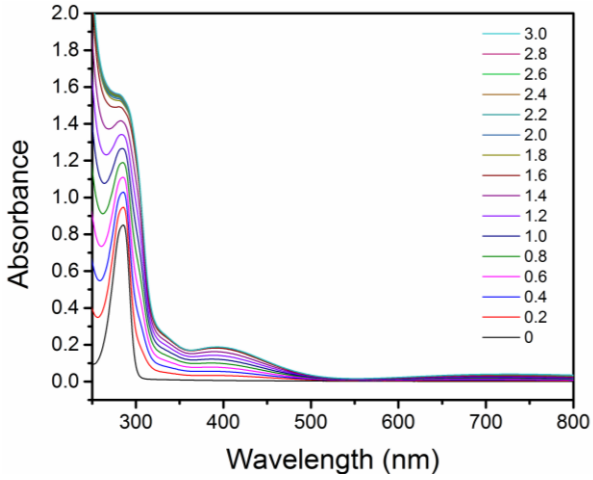

Figure 2.3 UV-Vis spectra of a solution containing 0.317 mM of HL and 5 mM of HEPES at pH 7, with incremental additions of a 50 mM aqueous solution of $Cu(NO_3)_2 \cdot 3H_2O$. Total numbers of stoichiometric equivalents of Cu corresponding to each addition are given in the legend.

Compound **1** crystalizes in the space group $P\bar{1}$, with an asymmetric unit that contains two nearly identical Cu_2 complexes (see Figure 2.2, left). The two Cu^{II} centers of each molecule

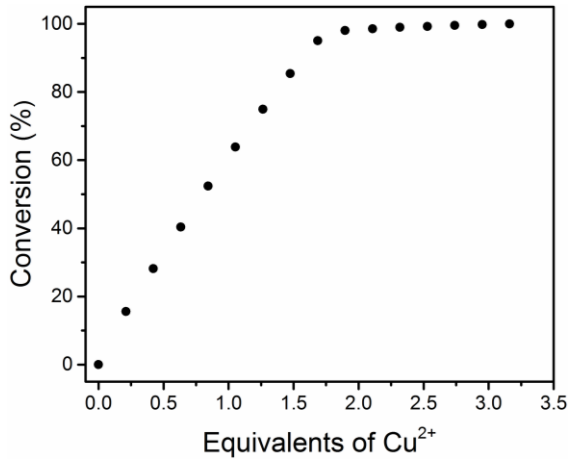

Figure 2.4 Reaction of HL with Cu^{II}, as monitored by the appearance of a peak at 398 nm in the UV-Visible spectra.

reside in distorted octahedral coordination environments, with significantly elongated Jahn-Teller axes along the O_{amide}-Cu-$O_{phenoxy}$ and $O_{phosphate}$-Cu-N_{amine} vectors. As a result, all four pendant amides are structurally inequivalent in the solid state. The tetraanionic pyrophosphate unit acts as a tetradentate, dinucleating bridging ligand that coordinates the two Cu centers in a μ^2-κ^4 configuration. This binding mode presumably engenders a chelate effect of $(P_2O_7)^{4-}$ that results in preferential coordination of the Cu_2 complex over water molecules and other anions in solution. The mean Cu···Cu distance of 3.658(1) Å is comparable to those reported for alkoxo- or phenoxo-bridged Cu^{II}_2 complexes that feature acetate ancillary bridging ligands.[8] Finally, the mean Cu-O-Cu angle of 123.8(2)° is similar to those reported for Cu_2 complexes with weak antiferromagnetic or ferromagnetic exchange coupling.[21]

In anticipation of CEST experiments in aqueous media, we sought to confirm the integrity and structure of $[LCu_2(P_2O_7)]^-$ in buffered aqueous solution. Toward this end, the kinetic and thermodynamic profiles of complexation for Cu^{2+} ions by L^- and $(P_2O_7)^{4-}$ in aqueous solution were monitored by UV/Visible spectroscopy. First, small aliquots of a 50 mM aqueous solution of $Cu(NO_3)_2 \cdot 3H_2O$ were titrated into a pH 7 buffer solution of 5 mM 4-(2-hydroxyethyl)-1-piperazineethanesulfonic acid (HEPES) containing 0.317 mM HL (see Figure 2.3). Prior to Cu addition, the spectrum of HL was characterized by one major peak at 285 nm, which we tentatively assign as a π–π transition. Upon Cu addition, two new features at 398 nm (ε = 580 M^{-1} cm^{-1}) and

726 nm (ε = 129 M^{-1} cm^{-1}) emerged, which we tentatively assign as ligand-metal charge transfer (LMCT) and *d*–*d* transitions, respectively, based on literature precedent.[8bc] Spectral changes ceased within 3 minutes following each addition, suggesting a relatively rapid Cu complexation by L^-. Moreover, the peak intensity at 398 nm is linearly dependent on the concentration of Cu^{2+} and reaches a maximum value upon addition of two equivalents of Cu^{2+} (see Figure 2.4), suggesting the formation of a 1:2 complex of L^- and Cu^{2+} with a dissociation constant well below millimolar. The resulting species is likely either the diaquo adduct $[LCu_2(H_2O)_4]^{3+}$ or the μ-hydroxo adduct $[LCu_2(\mu\text{-}OH)]^{2+}$, as have been observed in related tetrapyridyl-supported Cu^{II}_2 complexes.[22]

Titration of the Cu_2 solution with a buffered pH 7 aqueous solution of $K_4(P_2O_7)$ revealed similarly rapid complexation kinetics. Here, peak maxima corresponding to the LMCT and *d*–*d* transition shift from 398 to 432 nm (ε = 735

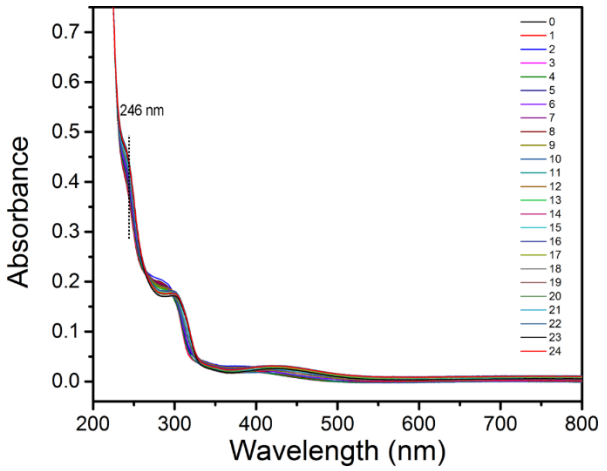

Figure 2.5 UV-Vis spectra of a solution containing 40.2 μM of HL with 2 eq. of Cu^{II} and 300 μM of HEPES at pH 7, with incremental additions of a 5.67 mM (1st to 15th addition) or 17.0 mM (16th to 24th addition) of $K_4P_2O_7$ in the same buffer. Color assignments of each addition are given in the legend. Dotted line indicates the location of 246 nm absorbance which is used in Figure 2.6 for fitting.

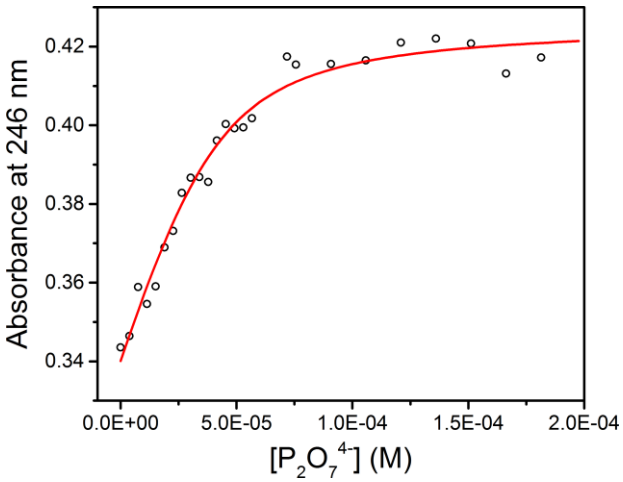

Figure 2.6 The absorbance at 246 nm of each spectrum in Figure 2.5 are plotted against the concentration of $(P_2O_7)^{4-}$ added. The plot was fitted to obtain the dissociation constant of $[LCu_2(P_2O_7)]^-$. Black hollow spheres represent experimental data; red line represent the fit.

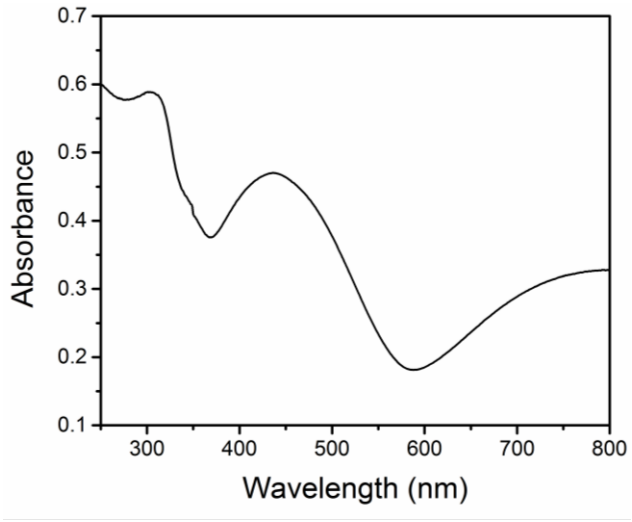

Figure 2.7 Diffuse-reflectance spectrum for a solid sample of **1**.

M^{-1} cm^{-1}) and 726 to 779 nm (ε = 104 M^{-1} cm^{-1}), respectively, with each conversion proceeding through an isosbestic point (see Figure 2.5). These spectral changes suggest that aquo or hydroxo ligands are displaced by $(P_2O_7)^{4-}$ ligands. In addition, the d-d transition at 779 nm lies in between that of $[Cu(H_2O)_6]^{2+}$ (810 nm, ε = 12 M^{-1} cm^{-1}) and that of $[Cu(EDTA)]^{2-}$ (735 nm, ε = 85 M^{-1} cm^{-1}), confirming the preservation of the elongated Cu^{II} octahedral geometry in solution.[23] Fitting the absorbance data at 246 nm from titrations at lower concentration (40.2 μM) gave a dissociation constant of K_d = 9(2) μM (see Figure 2.6), confirming the high affinity of $(P_2O_7)^{4-}$. Finally, the diffuse-reflectance spectrum collected for a solid sample of **1** features peaks with maxima at 436 and 788 nm (see Figure 2.7), and an electrospray mass spectrum exhibits three major patterns corresponding to adducts of the anionic complex of **1** (see Figure 2.8). Taken together, these data lead us to conclude that the structure of $[LCu_2(P_2O_7)]^-$ determined from X-ray diffraction analysis is preserved in aqueous HEPES solution. Finally, the spectrum of **2** exhibits similar features to that of **1** (see Figures 2.9–10), with the LMCT and *d–d* transitions at 418 nm (ε = 297 M^{-1}) and 784 nm (ε = 75 M^{-1} cm^{-1}), respectively, only slightly shifted. These spectral similarities suggest that the Cu centers in **1** and **2** feature very similar coordination environments in aqueous solution.

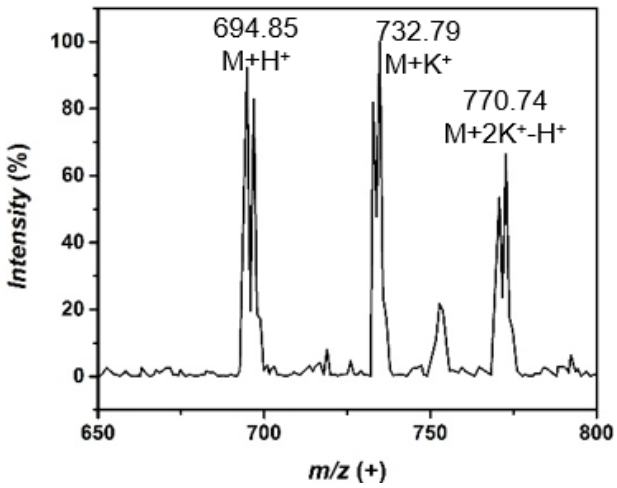

Figure 2.8 Electrospray ionization mass spectrum of **1** in H_2O, where M = $[LCu_2(P_2O_7)]^-$.

Variable-temperature dc magnetic susceptibility data were collected in order to determine the sign and magnitude of magnetic coupling in the Cu_2 complex. To best approximate the magnetic interactions in aqueous solution, magnetic data were collected on a solution of **1** in a 1:1 H_2O/glycerol mixture (see Figure 2.11).[24] Due to the error associated with mass determination of such a small amount of solute, the number of moles of Cu_2 complex was determined by a fixed g = 2.0629 obtained from X-band EPR along with the assumption that the high-temperature values of $\chi_M T$ correspond to two non-interacting $S = {}^1/_2$ centers (see Figure 2.12). The corresponding plot of $\chi_M T$ vs T is shown in Figure 2.13. With decreasing temperature, the $\chi_M T$ data remain relatively constant to ca. 100 K, whereupon they undergo a gradual increase to a maximum value of $\chi_M T$ = 0.929 cm^3K/mol at 6 K. Below 6 K, $\chi_M T$ decreases sharply to reach a minimum value of 0.853 cm^3K/mol at 2 K. The increase in $\chi_M T$ below 100 K stems from ferromagnetic coupling between the Cu^{II} ions, most likely dominated by superexchange coupling through the phenoxo bridge, to give an S = 1 ground state.

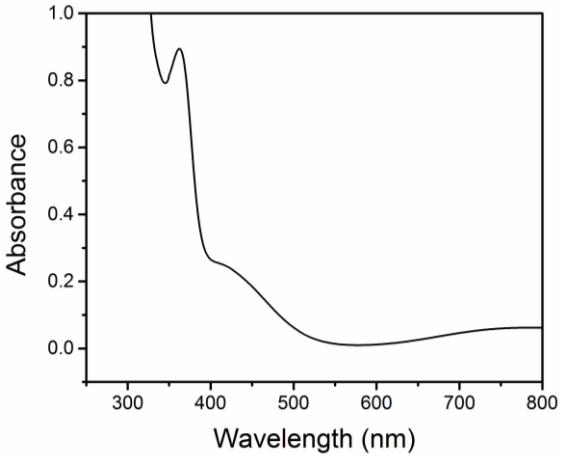

Figure 2.9 UV-Vis spectrum of 0.832 mM of **2** in 3 mM HEPES buffer solution at pH 7.

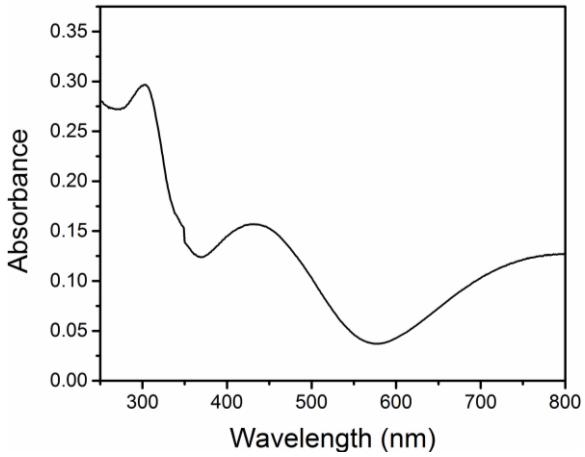

Figure 2.10 Diffuse-reflectance spectrum for a solid sample of **2**.

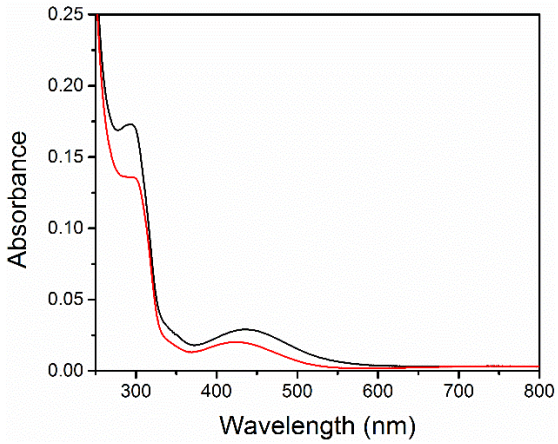

Figure 2.11 UV-Vis spectra of 0.317 mM of **1** in H_2O (black) and in 1:1 H_2O/glycerol (red).

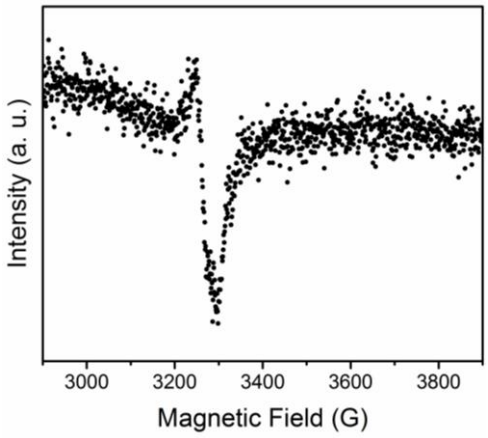

Figure 2.12 X-band EPR spectrum of **1** in a 1:1 H_2O/glycerol solution at 77 K.

Accordingly, the data were fit in the temperature range 10–300 K to the Van Vleck equation considering the spin Hamiltonian $\hat{H} = -2J(\hat{S}_{Cu1} \cdot \hat{S}_{Cu2})$.[25] Here, J represents the magnetic exchange coupling constant, which quantitate the strength of the coupling interaction, while $\hat{S}_{Cu1}$ and $\hat{S}_{Cu2}$ are the spin operators. The corresponding fit to the data gave an exchange constant of $J = +2.69(5)$ cm^{-1}, indicating a weak ferromagnetic Cu···Cu interaction in solution (see Figure 2.13). This weak interaction results in an energetic separation of the $S = 1$ ground state and $S = 0$ excited state of only 5.38 cm^{-1} (see Figure 2.13, inset), and this observation suggests that **1** may feature a

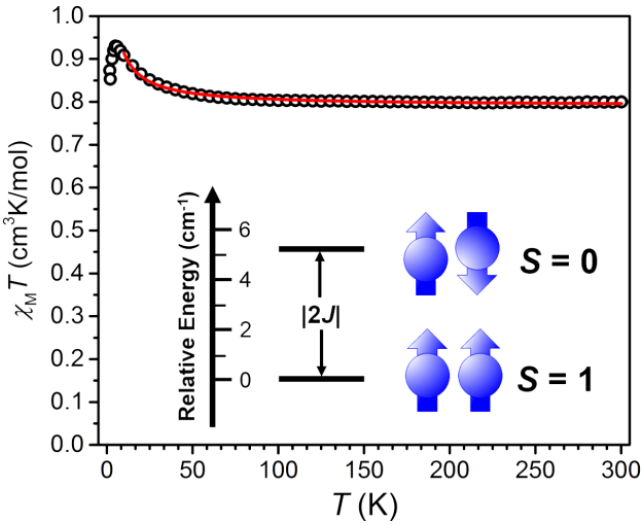

Figure 2.13 Variable-temperature dc magnetic susceptibility data for **1** in 1:1 H_2O/glycerol, collected under an applied field of 1 T. The red line corresponds to a fit of the data. Inset: Spin ladder and graphical representation of the energetic separation between S = 1 ground and S = 0 excited state.

considered shortened τ_s relative to a monocopper complex with a Cu^{II} center of similar coordination.

The relaxation of proton nuclear spins in **1** and **2** were probed by ^{1}H NMR in order to obtain a qualitative comparison of τ_s. More specifically, electronic spins with long values of τ_s induce a shortening of spin-lattice relaxation time (T_1) in proximal nuclear spins, which leads to a broadening of the NMR spectra. Indeed, such an analysis has been previously employed to obtain a qualitative measure for τ_s in related Cu_2 complexes.[7, 8b] Importantly, the presence of similar local coordination environments of the Cu^{II} centers in **1** and **2** suggests that the hyperfine shifts of analogous protons on the two complexes should be similar. In the case of **1**, the ^{1}H NMR spec-trum collected for a 10 mM H_2O solution at 37 °C features three paramagnetically-shifted resonances at 12, 14, and 29 ppm vs H_2O. Inversion recovery experiments of the three peaks give values of T_1 = 8(1), 13(1) and 22(4) ms, respectively (see Figure 2.14), suggesting that the T_1 shortening of the peaks by the Cu^{II} centers is comparable for all three resonances. In addition, the peak at 29 ppm is absent in the spectrum of **1** in D_2O, indicating that this peak corresponds to the exchangeable amide protons. Importantly, the presence of only one amide resonance suggests relatively fast interchange among the four pendant arms in solution that leads to an average of four inequivalent amides. As such, the broadness of the amide

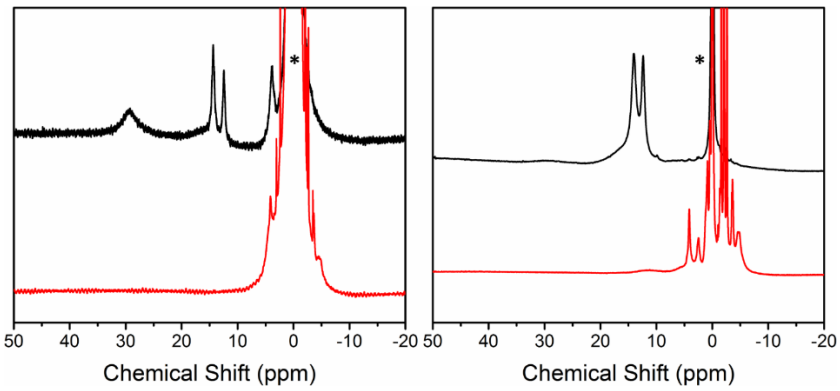

Figure 2.14 ^{1}H NMR spectra of **1** (black) and **2** (red) in D_2O (left) and 30 mM HEPES H_2O buffer (right) at pH 7 at 37 °C. Asterisks denote solvent peaks.

resonance, compared to the other two paramagnetic peaks, is more likely due to the combination of fast molecular dynamics and the proton-exchange nature, rather than electronic relaxation from the Cu^{II} centers. In stark contrast, an aqueous sample containing 30 mM of **2** in either D_2O or H_2O gave a spectrum that is absent of any resolvable resonances in the paramagnetic region (see Figure 2.14), presumably due to severe line broadening induced by electronic relaxation. This comparison provides strong qualitative evidence that the Cu_2 complex in **1** features a shorter τ_s than does the GaCu complex in **2**, likely resulting from the presence of weak magnetic exchange coupling in **1**.[8b]

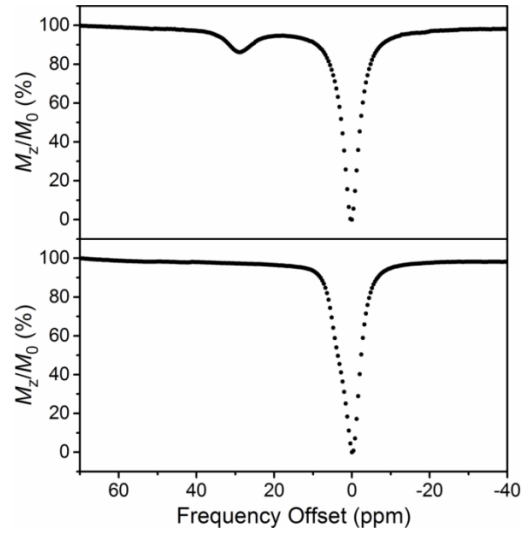

Figure 2.15 CEST spectra of 10 mM of **1** (top) and 30 mM of **2** (bottom) solutions in 50 mM of HEPES buffer at pH 7 and 37°C, with a 2 s presaturation pulse of 21 μT.

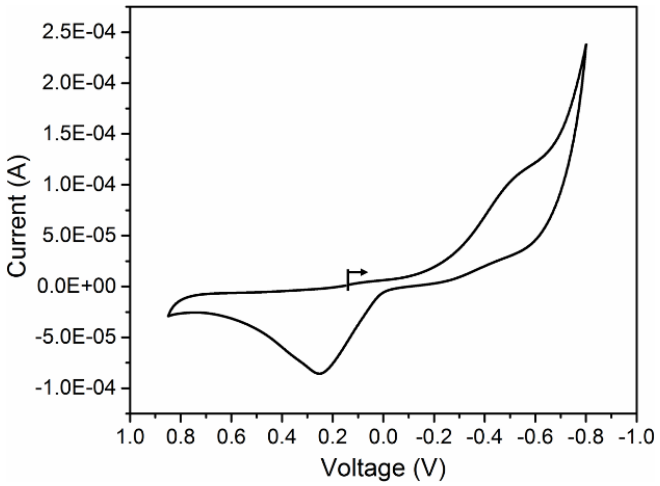

Figure 2.16 Cyclic voltammogram for 20 mM **1** in aqueous solution at pH 7, using a glassy carbon electrode, 10 mV/s scan rate and 0.1 M $NaClO_4$ supporting electrolyte.

The dramatic sharpening of the NMR linewidths for the Cu_2 complex relative to the monocopper analogue indicates the possibility to observe the CEST effect. We therefore collected ^{1}H NMR spectra on solutions of **1** and **2** in 50 mM HEPES buffer at pH 7 and 37 °C following a series of presaturation pulses at selected frequencies, using an 11.75 T NMR spectrometer (see Figure 2.15). The resulting CEST spectra, also known as Z-spectra, were constructed by plotting the intensity of the water ^{1}H NMR signal (M_Z/M_0, where M_0 and M_Z correspond to the bulk water signal before and after presaturation at a given frequency, respectively) against the presaturation frequency (i.e. frequency offset) relative to the bulk water frequency, which is set to 0 ppm. For **1** and **2**, complete disappearance of the water signal was observed at 0 ppm, arising from direct saturation at the water proton resonance. For **1**, in stark contrast to **2**, a peak was observed at 29 ppm corresponding to a 14% decrease in intensity of the water signal due to CEST. Although significant, note that the CEST effect is likely limited due to incomplete presaturation of the broad resonance of the amide protons. Note that the presence of a slight shoulder on the water resonance in **2** likely corresponds to CEST arising from carboxamide protons coordinated to the diamagnetic Ga^{III} center. Since the T_1 of water protons can significantly influence CEST effect,[1b] these values were measured for solutions of **1** and **2**, in addition to pure water. The obtained values of T_1 = 105(4), 110(20), 90(20) ms, respectively, are statistically indistinguishable and therefore suggest that neither **1** nor **2**

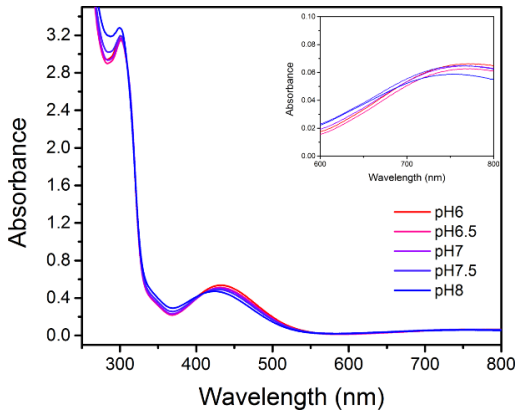

Figure 2.17 UV-Vis spectra for solutions containing 0.8 mM of **1** buffered at different pH values. Buffers contain 3 mM of MES (pH 6) or HEPES (pH 6.5, 7, 7.5 and 8). Inset shows the region for *d*–*d* transitions.

significantly alters the relaxation of water protons. For **1**, the CEST peak intensity at 25 °C decreases to 7.8%, suggesting that the exchange rate of the carboxamide protons is in the slow exchange regime with respect to the saturation offset. The exchange rate at 37 °C was estimated at k_{ex} = 420(20) s^{-1} by employing the Omega plot method,[16] and this value is comparable to those reported for mononuclear Fe-based PARACEST agents with pendant carboxamide groups.[4d, 26] Interestingly, despite containing $S = {}^1/_2$ metal centers with negligible single-ion magnetic anisotropy, **1** gives rise to a CEST peak shift and intensity that is comparable to some reported mononuclear PARACEST agents comprised of the high-spin, high-anisotropy Fe^{II} ion.[4d, 26] In sum, these experiments demonstrate the ability of **1** to provide MR contrast through the CEST effect.

Preliminary experiments were carried out to probe the stability of **1** to reduction, pH variation, and ion substitution. The cyclic voltammogram of **1** shows a reduction wave at ca. −500 mV vs NHE (see Figure 2.16), suggesting that **1** would not undergo reduction under physiological conditions.[17] In addition, the UV-Vis spectra of **1** confirm the integrity of $[LCu_2(P_2O_7)]^-$ in the pH

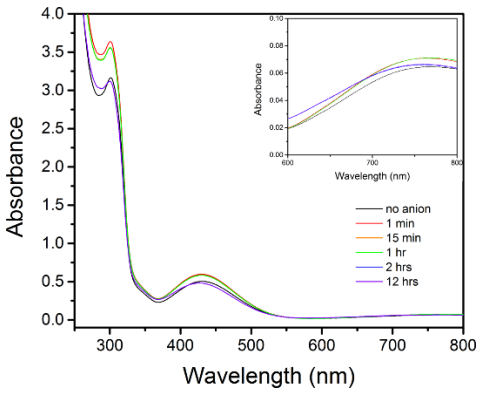

Figure 2.18 UV-Vis spectra for solutions containing 0.8 mM of **1**, 4 mM of Na_2CO_3 and NaH_2PO_4, and 3 mM HEPES buffered at pH 7. The color assignment in the legend correspond to spectra with different incubation times. Inset shows region for the *d*–*d* transitions.

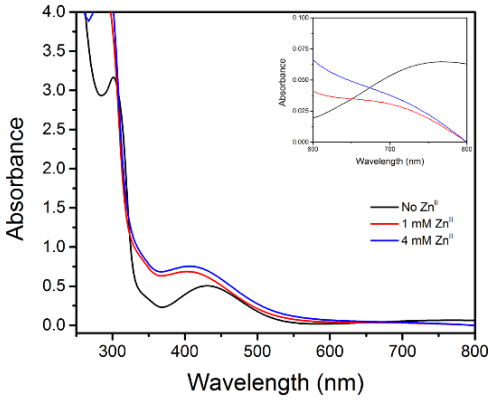

Figure 2.19 UV-Vis spectra for solutions containing 0.8 mM of **1**, selected concentrations of $Zn(NO_3)_2 \cdot 6H_2O$ and 3 mM HEPES buffered at pH 7. The color assignments in the legend correspond to spectra with different Zn^{II} concentrations. Inset shows region for the *d*–*d* transitions.

range 6–8 or in the presence of excess Na_2CO_3 and NaH_2PO_4 (see Figures 2.17–18). However, in the presence of excess Zn^{2+} ions, the LMCT is red shifted by 20 nm and the *d–d* transition disappears (see Figure 2.19), suggesting the presence of Zn^{II} substitution.

2.4 Conclusion

The foregoing results demonstrate that the limited scope of metal ions suitable for PARACEST can be expanded through introduction of magnetic exchange coupling in multinuclear complexes. Here, a Cu^{II}_2 complex is shown to exhibit the CEST effect, in contrast to its monocopper analogue, resulting from the presence of weak ferromagnetic exchange coupling between Cu centers. Efforts are underway to extend this initial proof-of-concept investigation to metal ions with larger values of spin and higher stability and to apply this strategy to the design of responsive PARACEST agents.

Chapter Three: Ratiometric Quantitation of Redox Status with a Molecular Fe_2 Magnetic Resonance Probe

Reprinted with permission from:

Du, K; Waters, E. A.; Harris, T. D. *Chem. Sci.* **2017**, *8*, 4424-4430.

This work was performed in collaboration with the co-authors listed above.

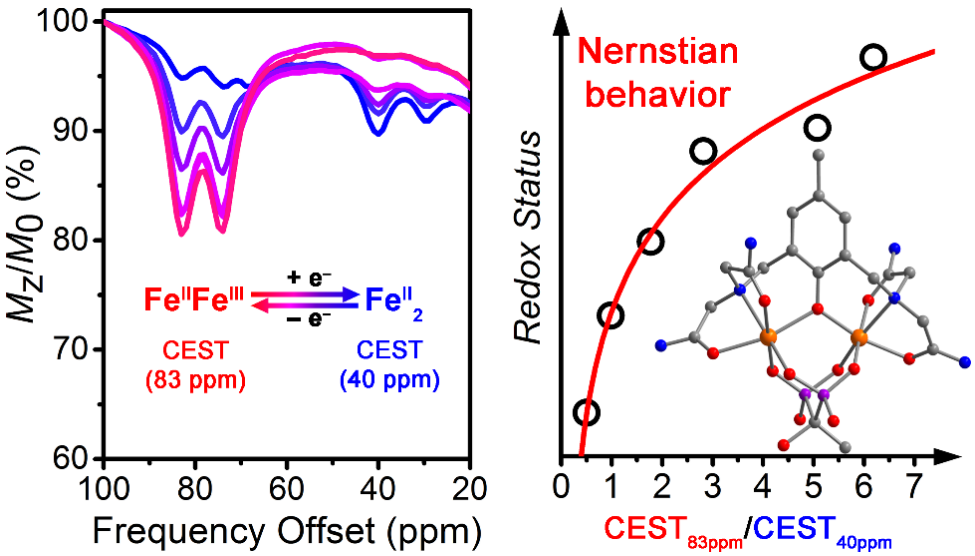

3.1 Introduction

The redox status of intra- and extracellular environments is a vital biomarker for disease, as it provides a collective picture of the concentration of redox-active species, such as thiols, reactive oxygen or nitrogen species, signaling molecules (e.g. NO/H_2O_2), and redox-active proteins (e.g. superoxide dismutases), which are key participants in cell apoptosis and proliferation.[1] For this reason, the ability to quantitatively interrogate redox environment represents an important challenge. One approach toward this end involves the employment of analytical methods, such as HPLC[2] and fluorescence spectrometry,[3] to determine the ratio of oxidized to reduced species in an extracted sample. Whereas these procedures provide important information regarding the redox-dependence of cancer-related cell activities in tissues[4] and cultured cells,[5] they nonetheless suffer from key disadvantages in that they require physical withdrawal of a sample and provide only a single spatiotemporal point, rather than global, measurement. Indeed, a non-invasive imaging method for spatiotemporal redox mapping would represent an invaluable tool for both diagnostic and pathological investigations of redox status.

Magnetic resonance imaging (MRI) is a powerful and non-invasive imaging technique, as it utilizes non-ionizing radio radiation that deeply penetrates tissue to provide high spatiotemporal image resolution.[6] As such, MRI represents an ideal modality for redox mapping of tissue. Toward this end, numerous metallic molecular MRI probes have shown the capability to detect pO2/hypoxia,[7] peroxide,[8] thiols,[9] NADH,[10] and redox active metals.[11] In general, these probes show negligible contrast in one oxidation state but are activated upon oxidation or reduction to generate MRI contrast, with a number of activation mechanisms having been reported. For instance, lanthanide probes can feature redox-active pendent groups on the ligand that cause

structural changes upon redox chemistry to turn contrast on or off.[9a, 10] In addition, transition metal probes can exploit metal-based redox processes, where a change in oxidation state of the metal center turns contrast on or off.[7ce]

A key limitation of turn-on or turn-off probes is their inability to provide quantitative information about redox environment, owing to unpredictable, inhomogeneous probe concentration in tissue that results from variable biodistribution patterns. As an alternative, one can envision use of a single molecule that features two individually addressable "on" oxidation states, with the ratio of the two signals giving a concentration-independent measureable that can be used to quantitate solution redox environment. Toward this end, PARACEST represents a promising method for ratiometric redox quantitation.[12] This technique employs paramagnetic probes with highly-shifted exchangeable protons that, upon selective irradiation, are delivered to bulk H_2O to generate contrast. In principle, for a probe accessible in two CEST-active oxidation states, the ratio between the CEST effects of the redox states would provide a concentration-independent measure of solution redox environment.

In order for a molecule to display the PARACEST effect in two oxidation states, the metal center must first be paramagnetic in both states. One such scenario is high-spin Fe^{II} and high-spin Fe^{III}. However, the electronic relaxation time (τ_s) of high-spin Fe^{III} is usually too long (ca. 10^{-10} s) to give sharp 1H NMR spectra,[13] another requirement for PARACEST. Alternatively, moving to a redox-active molecule with multiple metal centers offers a more straightforward and general strategy toward realizing multiple oxidation states with short τ_s. Recently, we reported a dinucleating, tetra(carboxamide) ligand (HL; see Figure 3.1) that gives rise to a Cu_2 PARACEST agent.[14] Herein, we report the Fe_2 analogue and demonstrate PARACEST activity in both the

$Fe^{II}Fe^{III}$ and $Fe^{II}Fe^{II}$ form that enables ratiometric quantitation of solution open-circuit potential. To our knowledge, this study provides the first example of ratiometric quantitation of solution redox environment using an MR probe.

3.2 Experimental Section

General considerations. Unless otherwise specified, chemicals and solvents were purchased from commercial vendors and used without further purification. Deuterated solvents were purchased from Cambridge Isotope Laboratories. When necessary for moisture sensitive experiments, glassware was flame dried or stored in an oven at 150 °C for at least 4 hours, followed by cooling in a desiccator. Air- and water-free manipulations were carried out using standard Schlenk techniques. Acetonitrile was dried using a commercial solvent purification system from Pure Process Technology and stored over 4 Å molecular sieves prior to use. Water was obtained from a purification system from EMD Millipore. Elemental analysis was conducted by Midwest Microlab Inc. Preparative reverse-phase HPLC was performed on a Waters 19 × 250 mm^2 Xbridge C18 Column, using the Varian Prostar 500 system equipped with a Varian 363 fluorescence detector and a Varian 335 UV/Visible Detector. During HPLC, water was used as solvent A and acetonitrile as solvent B. The absorbances at 220 and 285 nm were monitored. Anhydrous hydrogen chloride gas was generated by adding concentrated hydrochloric acid to a stirring solution of concentrated sulfuric acid. The gas was passed through a bubbler filled with sulfuric acid. Synthesis of *N*,*N*′-[(2-hydroxy-5-methyl-1,3-phenylene)bis(methylene)]bis[N-(carboxymethyl)glycinamide] (HL) was based off a procedure reported previously.[14]

Synthesis of $(NMe_4)[LFe_2L']\cdot 2.7H_2O\cdot THF$ (1). To a stirred suspension of HL (20 mg, 0.051 mmol) in MeOH (2 mL) was added dropwise a solution of anhydrous $FeCl_2$ (13 mg, 0.10 mmol)

in MeOH (2 mL) to give a light purple solution. A solution of etidronic acid monohydrate (11.4 mg, 0.051 mmol) in MeOH (2 mL) was then added dropwise to give a light orange solution, followed by addition of $NMe_4OH{\cdot}5H_2O$ (46 mg, 0.26 mmol) in MeOH (2 mL) to give a light yellow slurry. After stirring for 12 hours, the yellow solid was collected by filtration and washed with MeOH (10 mL). The solid was then stirred in THF (15 mL) for 20 min, collected by filtration, and dried under reduced pressure for 12 hours to give **1** (20 mg, 50%). Solution magnetic moment $\chi_M T$ = 7.3(3) cm^3K/mol (310 K). Anal. Calcd. for $C_{27}H_{54.4}Fe_2N_7O_{15.7}P_2$: C, 35.99; H, 6.08; N, 10.87. Found: C, 36.00; H, 6.15; N, 10.91. ICP-OES: Fe:P = 0.96:1. UV-Vis absorption spectrum: 453 nm (ε = 48 $M^{-1}\,cm^{-1}$). FT-IR (ATR, cm^{-1}): 3289 (m, broad); 3158 (m, broad); 1668 (s); 1615 (s); 1475 (s); 1447 (w); 1311 (s); 1262 (w); 1097 (s); 1055 (s); 991 (m); 877 (m); 802 (w); 660 (m); 560 (s).

Synthesis of $LFe_2L'{\cdot}0.7H_2O{\cdot}0.2THF$ (2). To a stirred suspension of HL (20 mg, 0.051 mmol) in MeOH (2 mL) was added dropwise a solution of anhydrous $FeCl_3$ (8.2 mg, 0.051 mmol) in MeOH (2 mL) to give a dark purple solution. Anhydrous $FeCl_2$ (6.4 mg, 0.051 mmol) in MeOH (2 mL) was then added dropwise to this solution, with no significant color change observed. A solution of etidronic acid monohydrate (11 mg, 0.051 mmol) in MeOH (2 mL) was then added dropwise, resulting in a dark red solution. A solution of $NMe_4OH{\cdot}5H_2O$ (46 mg, 0.26 mmol) in MeOH (2 mL) was then added dropwise to give a red slurry. After stirring for 12 hours, the a red-brown solid was collected by filtration and was washed with MeOH (10 mL). The solid was then stirred in THF (15 mL) for 20 min, collected by filtration, and dried under reduced pressure for 12 h to give **2** (34 mg, 95%). Solution magnetic moment $\chi_M T$ = 7.0(6) cm^3K/mol (310 K). Anal. Calcd. for $C_{19.8}H_{32}Fe_2N_6O_{12.9}P_2$: C, 32.40; H, 4.39; N, 11.45. Found: C, 32.40; H, 4.27; N, 11.38.

ICP-OES: Fe:P = 0.97:1. UV-Vis absorption spectrum: 470 nm (ε = 861 M^{-1} cm^{-1}), 801 nm (ε = 168 M^{-1} cm^{-1}), 1383 nm (ε = 83 M^{-1} cm^{-1}). FT-IR (ATR, cm^{-1}): 3278 (m, broad); 2969 (m, broad); 1655 (s); 1613 (s); 1479 (m); 1453 (w); 1311 (m); 1263 (m); 1120 (s); 1049 (s); 988 (s); 877 (m); 805 (w); 662 (m); 562 (s). Slow diffusion of THF vapor into a concentrated solution of **2** in H_2O over the course of 3 days gave dark red plate-shaped crystals of LFe_2(etidronate)·$7H_2O$ suitable for single-crystal X-ray diffraction analysis.

Synthesis of [LFe_2L'](NO_3)·$0.9H_2O$·1.5THF (3). To a stirred suspension of HL (20 mg, 0.051 mmol) in MeOH (2 mL) was added dropwise a solution of $Fe(NO_3)_3$·$9H_2O$ (41 mg, 0.10 mmol) in MeOH (2 mL) to give a dark purple solution. A solution of etidronic acid monohydrate (11 mg, 0.051 mmol) in MeOH (2 mL) was then added dropwise to give a red solution. A solution of NMe_4OH·$5H_2O$ (46 mg, 0.26 mmol) in MeOH (2 mL) was then added dropwise give a red slurry. After stirring for 12 hours, the ensuing red solution was dried under reduced pressure to give a red solid. The solid was stirred in DMF (10 mL) for 30 min, and was then collected by filtration and washed with THF (10 mL) and Et_2O (10 mL). The residue was dried under reduced pressure for 2 h to give **3** (20 mg, 51%) Solution magnetic moment $\chi_M T$ = 8.9(3) cm^3K/mol (310 K). Anal. Calcd. for $C_{20.5}H_{36.7}Fe_2N_7O_{17.4}P_2$: C, 29.52; H, 4.44; N, 11.78. Found: C, 29.52; H, 4.53; N, 11.84. ICP-OES: Fe:P = 1.1:1. FT-IR (ATR, cm^{-1}): 3110 (m, broad); 1652 (s); 1591 (s); 1477 (m); 1417 (w); 1386 (m); 1315 (m); 1095 (m); 1001 (s); 880 (m); 800 (m); 664 (w); 573 (m); 468 (s); 448 (m); 414 (m).

X-ray structure determination. A single crystal of LFe_2(etidronate)·$7H_2O$ was directly coated with Paratone-N oil and mounted on a MicroMounts™ rod. The crystallographic data were collected at 100 K on a Bruker APEX II diffractometer equipped with MoKα sealed tube source.

Raw data were integrated and corrected for Lorentz and polarization effects using Bruker APEX2 v. 2009.1.[15] The program SADABS was use to apply absorption correction.[16] Space group assignments were determined by examining systematic absences, E-statistics and successive refinement of the structure. Structures were solved by SHELXT[17] using direct methods and refined by SHELXL within the OLEX interface.[18] Partially occupied solvent H_2O molecules that were potentially hydrogen bonded were modeled isotropically. Thermal parameters for all other non-hydrogen were refined anisotropically.

^{1}H NMR experiments. Variable temperature ^{1}H NMR spectra were collected on an Agilent DD MR-400 system (9.4 T) system. The T_1 of H_2O was obtained by fitting H_2O intensities from experiments with an array of relaxation times implemented in the program *vnmr*. Linewidth analyses were obtained the program MNOVA.

CEST experiments. Variable temperature CEST experiments were performed on an Agilent DD MR-400 system (9.4 T) system. In a typical experiment, samples containing 100% **1**, 100% **2** or mixture of the two at a desired ratio in buffer containing 100 mM NaCl and 100 mM of HEPES at pH desired were used for CEST experiments. Z-spectra (CEST spectra) were obtained according to the following protocol. NMR spectra were acquired using the presaturation pulse applied for 7 s at a power level of 24 μT. The saturation frequency offsets were screened with a step increase of 1 ppm. The obtained NMR spectra were plotted as normalized water intensity against frequency offset to produce a Z-spectrum. Direct saturation of the water signal was set to 0 ppm. D_2O was placed in an inner capillary to lock the sample. Exchange rate constants were calculated based off a reported method.[19] The B_1 values are calculated based on the calibrated 90- degree pulse on a linear amplifier. The NMR spectra were acquired at various presaturation powers ranging from 14

to 24 μT applied for 7 s. To correct for baseline, reported values of %CEST are the difference in percent H_2O signal reduction between applied on-resonance and off-resonance presaturations.

Solid state magnetic measurements. Magnetic measurements were carried out using a Quantum Design MPMS-XL SQUID magnetometer. Powder samples were sealed in 2 mL polyethylene bags. Dc susceptibility data were collected from 1.8 to 300 K at applied dc fields of 1, 1.5 and 2 T. Dc susceptibility data were corrected for diamagnetic contribution from the sample holders and from the sample (estimated using Pascal's constants[20]). The temperature dependent magnetic susceptibility data for **1** (1.8-300 K) and **2** (10-300 K) and were model using spin Hamiltonian $\hat{H} = -2J(\hat{S}_{Fe1} \cdot \hat{S}_{Fe2})$,[21] where J is the magnetic superexchange coupling constant; and $\hat{S}_{Fe1}$ and $\hat{S}_{Fe2}$ are the spin operators for the Fe ions. The best fits of the data give g = 2.20(3) and 2.00(4) for **1** and **2**, respectively.

Solution magnetic measurements. Magnetic moments of metal complexes were carried out using Evan's method[22] at 310 K. In a typical experiment, compounds (about 4 mM) were dissolved in mixture of 0.5 w/w % of DMSO in D_2O. A capillary containing same solvent mixture (without the to-be-characterized compound) was inserted into each NMR sample as reference. Diamagnetic correction was carried out based on the empirical formula of each compound (as determined by elemental analysis) using Pascal's constants.[20]

Electrochemical measurements. Cyclic voltammetry was carried out in a standard one-compartment cell inside a nitrogen glove box at room temperature, equipped with a platinum working electrode, a platinum wire as counter electrode and a SCE reference electrode using a CHI 760c potentiostat. The analyte solution was with 100 mM NaCl and 100 mM HEPES buffered at pH 7.4. The voltammogram was converted and shown as values referred to normal hydrogen

electrode (NHE), using literature conversion factor.[23] Open circuit potentials were measured by the built-in technique "open circuit potential – time" within the CHI660E electrochemical workstation software. The open circuit potential readings were recorded 10 minutes after the experiment started, at which time the reading was stabilized.

Mössbauer spectroscopy. Zero-field ^{57}Fe Mössbauer spectra were obtained at various temperatures with a constant acceleration spectrometer and a ^{57}Co/rhodium source. Prior to measurements, the spectrometer was calibrated at 295 K with α-iron foil. Samples were prepared in an MBraun nitrogen glove box. A typical sample contained approximately 60 mg of compounds (~10 mg of Fe) suspended in a plastic cap in heated eicosane, which solidified upon cooling to ambient temperature, in order to immobilize the sample. Another cap with a slightly smaller diameter was squeezed into the previous sample cap to completely encapsulate the solid sample mixture. All spectra were analyzed using the WMOSS Mössbauer Spectral Analysis Software (www.wmoss.org).

Other physical measurements. Infrared spectra were recorded on a Bruker Alpha FTIR spectrometer equipped with an attenuated total reflectance accessory. Solution and solid-state UV-Vis-NIR spectra were obtained using an Agilent Cary 5000 spectrophotometer.

Estimation of electron transfer rate by IVCT analysis.[24] The calculation of ambient temperature electron-transfer rate in **2** is based on a method described in a similar mixed-valence Fe_2 analog. Location of the IVCT ν_{max}, extinction coefficient (ε) and Fe···Fe distance (d) were obtained experimentally as described in the main text. The full width at half maximum ($\Delta\nu_{1/2}$) was determined by fitting IVCT to a Gaussian model in the software OriginPro. The electron-transfer rate (k_{et}) in **2** can be calculated using the following equation:

$$k_{et} = \nu_{et} \exp(-\Delta G^*/RT)$$

where R is the ideal gas constant and T is temperature. The frequency factor for electron transfer, ν_{et}, and the thermal free energy, ΔG^*, are given by:

$$\nu_{et} = 2\pi^{3/2} \nu_{ab} h^{-1} (kT\nu_{max})^{-1/2} \text{ and } \Delta G^* = \nu_{max}(4 - \nu_{ab})^{-1}$$

where h is Planck constant, k is Boltzmann constant and ν_{max} is the wavenumber of IVCT peak maximum. The resonance matrix element, ν_{ab}, is given by:

$$\nu_{ab} = \alpha\nu_{max},$$

where the extent of electron delocalization $\alpha^2 = 4.2 \times 10^{-4} \varepsilon \Delta\nu_{1/2} (\nu_{max} d^2)^{-1}$. Here, ε is the extinction coefficient of IVCT, and d is the Fe···Fe distance determined by X-ray structural analysis.

Viability experiment. Melanoma B16F10 cells (ATCC) were cultured in Dulbecco's Modified Eagle's Media (Life Technologies) supplemented with 10% fetal bovine serum (Fisher), 1 mM each of sodium pyruvate, non-essential amino acids and L-glycine at 37 °C and 5% CO_2. Cells for the experiment were subcultivated for 3 to 4 times after thawing the cell stocks. Cells were incubated with media containing the desired concentration of **3** for 24 h before viability measurements. Cell viability was measured by a Guava EasyCyte Mini Personal Cell Analyzer (EMD Millipore). Each sample subjected for analysis contained 50 μL of well-mixed cell suspension and 150 μL of Guava ViaCount reagent. Stained samples were vortexed for 20 s and immediately subjected to counting using the ViaCount software module. Viability was measured using the EasyFit software module. Cells not treated by **3** were used as a control to account for normal cell death. Reported %viability was normalized with respect to the control samples.

MRI phantom experiment. Samples contained 100 mM of NaCl, 100 mM of HEPES buffered at pH 7.4 and overall 10 mM Fe_2 concentration with **1**:**2** ratio ranging from 9:1 to 1:9. ~0.5 mL of each sample was stored in a 0.5 mL Eppendorf tube, which was placed within another scintillation vial filled with H_2O solution containing 1 mg/mL $CuSO_4$ and 100 mM NaCl for T_1 matching. CEST experiments were carried out on a Bruker Biospec 9.4 T MRI scanner running ParaVision 6.0.1 (Bruker Biospin, Billerica, MA, USA). Temperature was maintained at 37 °C using a warm water circulating system with feedback control from a temperature probe (SA Instruments, Stonybrook, NY, USA). CEST images were acquired using an accelerated spin echo based sequence with a pre-saturation pulse (14 μT, 2 s duration) applied at offsets of 83 and 40 ppm (M_z). Other imaging parameters: TR/TE = 2034/14.9 ms, RARE factor 16, matrix = 64 × 64, FOV = 3.2 × 3.2 cm, 2 mm slice thickness, and 2 averages). Matched unsaturated images were acquired using identical parameters except that the pulse amplitude was set to 0 μT (M_0). %CEST = $(1 - M_z/M_0) \times 100\%$. Averaged intensities of the same regions were used to calculate $CEST_{83\ ppm}/CEST_{40\ ppm}$ for fitting. For the fitting, sample A was a significant outlier likely due to weak CEST signal, and therefore was not taken into account for fitting. Trace amounts of precipitation occurred for sample D, E, F during the phantom

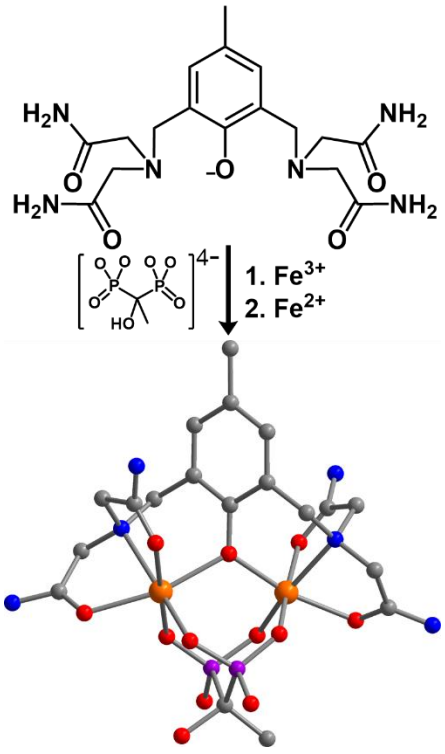

Figure 3.1 Synthetic scheme and structure of LFe_2(etidronate), as observed in LFe_2(etidronate)·$7H_2O$. Orange, purple, blue, red, and gray spheres represent Fe, P, N, O, and C atoms, respectively; H atoms are omitted for clarity.

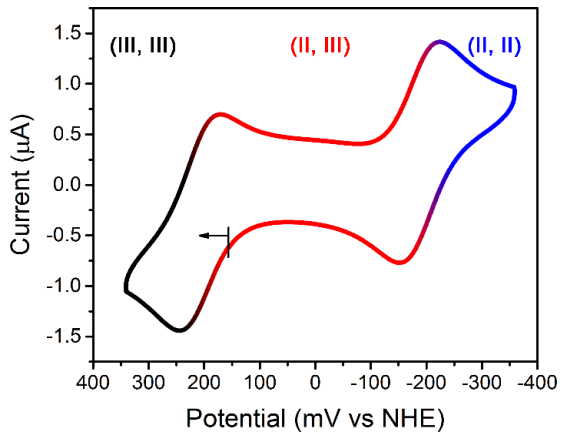

Figure 3.2 Cyclic voltammogram of **2** in solution containing 100 mM NaCl, 100 mM HEPES buffered at pH 7.4; scan rate = 50 mV/s. Roman numerals represent Fe oxidation states.

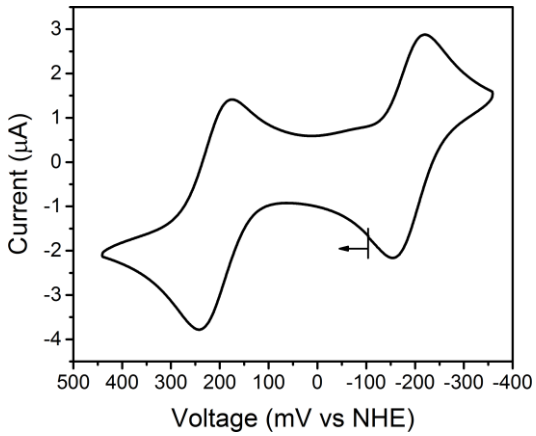

Figure 3.3 CV of **1** in solution containing 100 mM NaCl, 100 mM HEPES, buffered at pH 7.4. 50 mV/s scan rate.

experiment, likely due to the affected solubility of **1** and/or **2** in the presence of high buffer concentration. Such precipitate did not alter either the phantom experiment or OCP measurement.

3.3 Results and Discussion

The synthesis of the anionic complex $[LFe_2(etidronate)]^-$ was carried out through successive additions of two equivalents of $[Fe(H_2O)_6]^{2+}$ and one equivalent of etidronic acid, in the presence of NMe_4OH, to a solution of HL in methanol, to give the compound $(NMe_4)[LFe^{II}_2(etidronate)]\cdot 2.7H_2O\cdot THF$ (**1**) as a light yellow solid. The analogous mixed-valence $Fe^{II}Fe^{III}$ and univalence Fe^{III}_2 complexes were prepared similarly, but with 1:1 $[Fe(H_2O)_6]^{2+}$:$[Fe(H_2O)_6]^{3+}$ and exclusively $[Fe(H_2O)_6]^{3+}$, respectively, to afford the red compounds $LFe_2(etidronate)\cdot 0.7H_2O\cdot 0.2THF$ (**2**) and $[LFe_2(etidronate)](NO_3)\cdot 0.9H_2O\cdot 1.5THF$ (**3**). The presence of etidronate, in contrast to pyrophosphate in the Cu_2 analogue,[14] improves solubility of the neutral molecule, $LFe_2(etidronate)$, in H_2O.

Slow diffusion of THF vapor into a concentrated solution of **2** in H_2O afforded plate-shaped single crystals of $LFe_2(etidronate)\cdot 7H_2O$ that were suitable for X-ray structural analysis. The structure features two distinct Fe centers, each in a distorted octahedral coordination environment

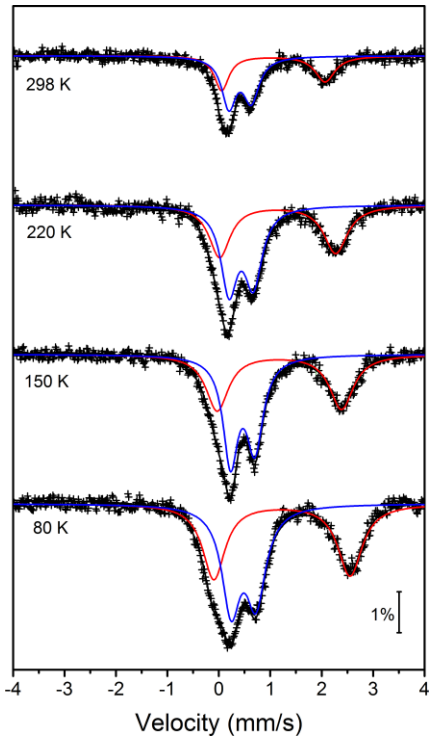

Figure 3.4 Variable temperature Mössbauer spectra of **2**. Crosses, black line, red line and blue line represent the experimental data, global fit, fit of high spin Fe^{II} and fit of high spin Fe^{III}, respectively.

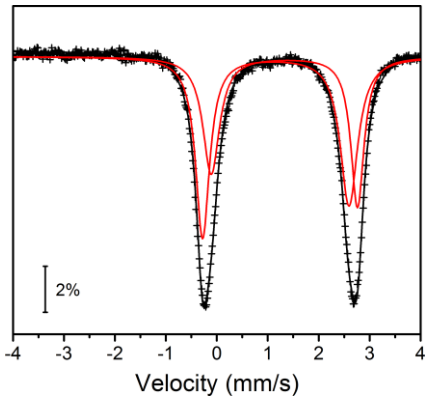

Figure 3.5 Mössbauer spectrum of **1** at 80 K. Crosses and red line represent the experimental data and fit, respectively.

comprising two carboxamide O atoms, one μ-phenoxo O atom, and one N atom from L^-, along with two O atoms from a μ^2-κ^4 etidronate bridging ligand (see Figure 3.1). The mean Fe–O bond distances for the two Fe centers are distinct at 1.992(5) and 2.125(6) Å, indicative of valence-localized high-spin Fe^{III} and Fe^{II}, respectively. The Fe-O_L-Fe angle of 118.6(3)° and Fe···Fe distance of 3.547(2) Å are consistent with related mixed-valence Fe_2 complexes.[25]

To probe the redox chemistry of the Fe_2 complex, a cyclic voltammogram was collected for an aqueous solution of **2** in HEPES buffer at pH 7.4. The voltammogram features two reversible processes at potentials of $E_{1/2}$ = –187 and 209 mV vs the Normal Hydrogen Electrode (NHE) (see Figure 3.2). These processes are assigned to the $Fe^{II}Fe^{II}/Fe^{II}Fe^{III}$ and $Fe^{II}Fe^{III}/Fe^{III}Fe^{III}$ couples, respectively. The potential separation of $\Delta E_{1/2}$ = 396 mV corresponds to a comproportionation constant of $K_c = 5.00 \times 10^6$ for the reaction $[LFe_2(etidronate)]^+ + [LFe_2(etidronate)]^- \rightarrow 2LFe_2(etidronate)$, indicating that the mixed-valence complex is stable towards disproportionation. Similarly, a solution of **1** gave an identical voltammogram, albeit with

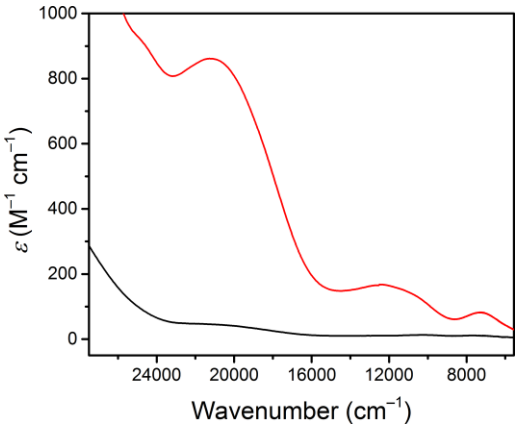

Figure 3.6 UV-Vis-NIR spectra of **1** (black) and **2** (red) in D_2O.

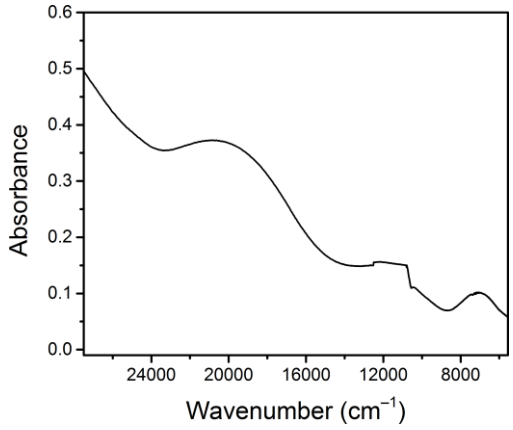

Figure 3.7 Diffuse reflectance spectrum of **2**. The flat feature at ca. 12000 cm^{-1} is an instrument artifact.

a different open-circuit potential (see Figure 3.3). Importantly, the redox window observed here is wide and biologically relevant, consistent with electrochemical potentials of intra- and extracellular environments, approximately –300 to 0 mV vs NHE.[12g] Further, note that the broad library of bisphosphonate ligands offers the possibility to tune the potential window to target specific redox environments.

Mössbauer spectra were collected to investigate the nature of mixed-valency in **2**. At 80 K, the compound displays two quadrupole doublets with isomer shifts of δ = 1.23(1) and 0.480(5) mm/s and quadrupole splittings of ΔE_Q = 2.65(2) and 0.485(8) mm/s, that we respectively assign to high-spin Fe^{II} and high-spin Fe^{III} (see Figure 3.4).[26] The areal ratio between the two spectral components of 1:1.1(1) indicates a valence-trapped $Fe^{II}Fe^{III}$ electronic structure, in agreement with crystallographic analysis.[27] In contrast, the spectrum for **1** at 80 K is best modeled with two doublets (δ = 1.325(8) and 1.158(7) mm/s, ΔE_Q = 2.871(7) and 2.874(6) mm/s) that correspond to two similar but inequivalent high-spin Fe^{II} centers (see Figure 3.5).

A solution of **2** in neutral D_2O exhibits features at 21,277 cm^{-1} (ε = 861 M^{-1} cm^{-1}) and 7318 cm^{-1} (ε = 83 M^{-1} cm^{-1}) (see Figure 3.6), which we assign to ligand-to-metal charge-transfer

(LMCT) and intervalence charge transfer (IVCT) bands, respectively, in accord with similar mixed-valence Fe_2 complexes.[28] Polar solvents often forestall electron transfer, and as such, the observation of IVCT in D_2O is notable and highlights the stability and rigidity of the Fe_2 complex. The IVCT full-width at half-maximum of $\Delta\upsilon_{1/2}$ = 3043 cm^{-1} is lower than the theoretical linewidth of $\Delta\upsilon^{\circ}_{1/2}$ = $(2310(\upsilon_{max}))^{1/2}$ = 4112 cm^{-1}, suggesting some degree of electron detrapping in **2**.[29, 30] Moreover, a linewidth analysis using the crystallographic Fe···Fe distance provides an estimate of the 298 K electron transfer rate as 6.7(1) × 10^{10} s^{-1}.[26a, 29] The solution spectrum closely resembles that of the solid-state diffuse reflectance (see Figure 3.7), suggesting that the crystallographic structure is retained in solution. In contrast to **2**, only a shoulder at 22000 cm^{-1} (ε = 48 M^{-1} cm^{-1}) is present in the spectrum for **1** (see Figure 3.6). This observation is consistent with a univalence Fe^{II}_2 configuration and agrees with literature examples.[31]

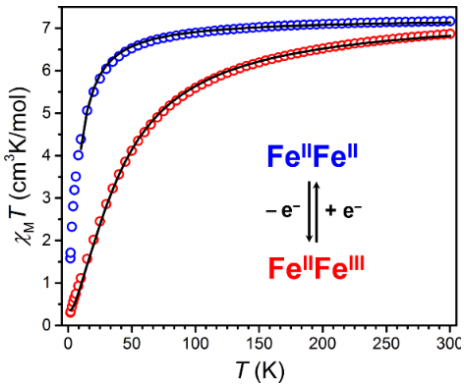

Figure 3.8 Variable temperature dc magnetic susceptibility data for **1** (blue circles) and **2** (red circles) collected under an applied field of 1 T. The black lines correspond to fits of the data.

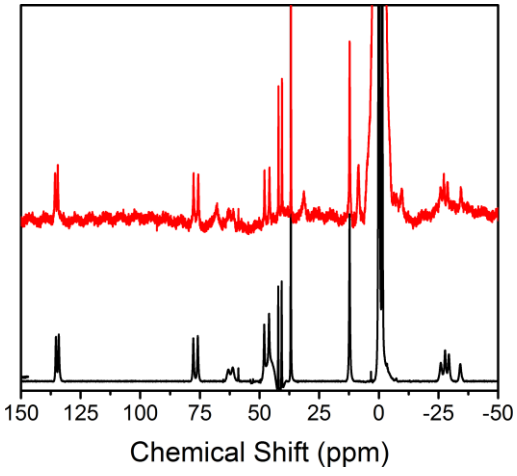

Figure 3.9 Stacked NMR spectra of **1** in neutral H_2O (red) and D_2O (black) at 37 °C.

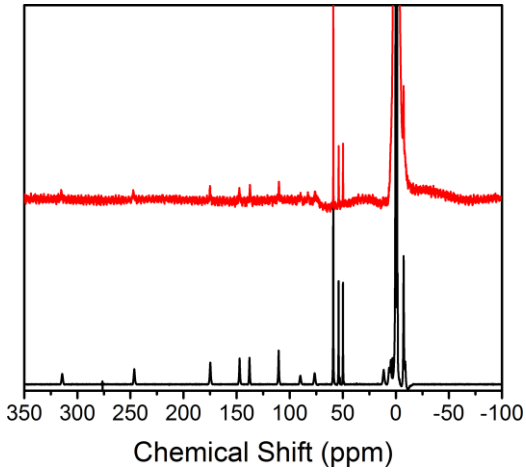

Figure 3.10 Stacked NMR spectra of **2** in neutral H_2O (red) and D_2O (black) at 37 °C.

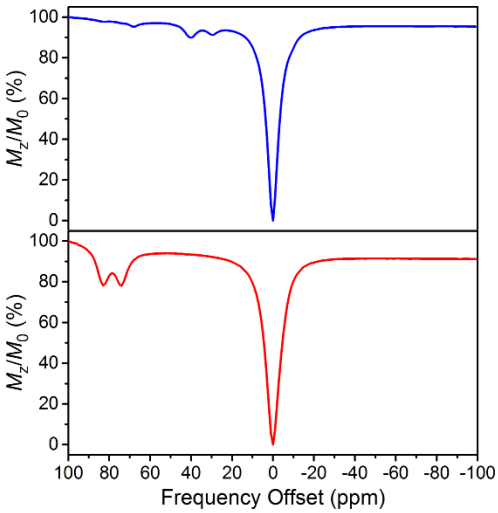

Figure 3.11 CEST spectra collected at 37 °C for solutions containing 4.9 mM of **1** (top) and **2** (bottom) with 100 mM HEPES and 100 mM NaCl buffered at pH 7.4.

To assess magnetic interactions in the Fe_2 complexes, variable-temperature magnetic susceptibility measurements were carried out for solid-state samples of **1** and **2** (see Figure 3.8). At 300 K, $\chi_M T$ = 7.17 cm^3K/mol for **1**, consistent with two non-interacting high-spin Fe^{II} centers with weak antiferromagnetic superexchange. For **2**, $\chi_M T$ = 6.87 cm^3K/mol at 300 K, consistent with high-spin Fe^{III} and Fe^{II}. For both compounds, $\chi_M T$ decreases with decreasing temperature, albeit more rapidly for **2**, indicative of antiferromagnetic superexchange. These interactions were modeled with the spin Hamiltonian $\hat{H} = -2J(\hat{S}_{Fe1} \cdot \hat{S}_{Fe2})$,[32] to give exchange coupling constants J = –0.8(3) cm^{-1} for **1** and J = –3.6(5) cm^{-1} for **2**. The stronger coupling in **2** is likely due to shorter Fe^{III}–O bond than the Fe^{II}–O bond in **1**. These values are comparable to those previously reported for structurally similar Fe_2 complexes.[26] Solution magnetic moments ($\chi_M T$) for **1**, **2** and **3** are 7.3(3), 7.0(6) and 8.9(3) cm^3K/mol at 310 K, respectively, consistent with the solid-state magnetic data as well as the presence all high-spin Fe^{II} and Fe^{III}. The larger-than-expected $\chi_M T$ for **1** is likely due to the anisotropic Fe^{II} as evidenced by the g value determined by EPR.

Neutral aqueous solutions of **1** and **2** gave sharp, well-resolved ^{1}H NMR spectra. The spectrum for **1** features 20 paramagnetically shifted resonances that range from –50 to 150 ppm (see Figure 3.9), with exchangeable protons appearing at –9.5, 8.5, 29, 40 and 68 ppm established by comparing the spectra obtained in D_2O and H_2O. These five resonances are assigned to four structurally inequivalent carboxamide groups and the etidronate hydroxyl group. In comparison, 14 paramagnetically shifted resonances are present in the spectrum for **2**, ranging from –10 to 320 ppm (see Figure 3.10). The resonances at 74 and 83 ppm are assigned to exchangeable protons on the carboxamide groups, as evidenced by their disappearance in the presence of D_2O. The full width at half maximum for the resonances of **1** and **2** are 65–820 Hz and 44–620 Hz, respectively. The similarity in linewidth suggests that the smaller number of observed paramagnetic shifts in **2** than **1** is likely due to peak-averaging caused by fast electron transfer rate ($6.7(1) \times 10^{10}$ s^{-1}), instead of peak-broadening caused by nuclear relaxation. Furthermore, Spin-lattice relaxation times (T_1) for H_2O, in samples containing 4.9 mM of **1** or **2** buffered at pH 7.4, are 1.30(1) and 1.14(1) s, respectively. The similar resonance linewidth and T_1 profiles suggest a shortening of τ_s in Fe^{III}, which otherwise would have imposed significant nuclear relaxation and thus severe line broadening. Such shortening of τ_s is likely due to the magnetic coupling to a fast-relaxing Fe^{II},[13] as well as fast electron-transfer between the two Fe centers. In sum, the significantly different but sharp carboxamide resonances in **1**

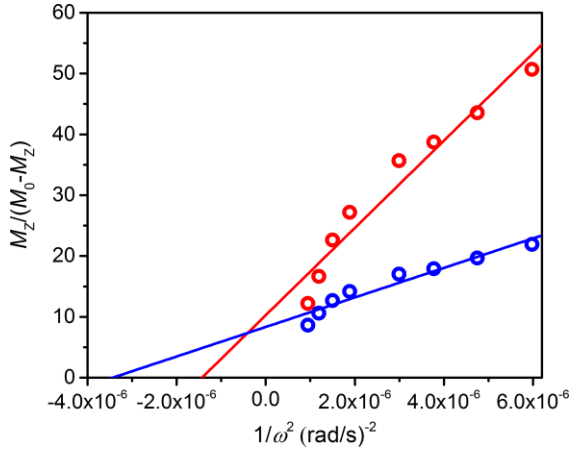

Figure 3.12 Omega plot of the CEST effect at 29 ppm (red) and 40 ppm (blue) of 4.0 mM **1** in pH 7.4 H_2O with 100 mM HEPES and 100 mM NaCl. Circles represent experimental data and the lines represent the linear fit.

and **2** suggests the possibility to observe the CEST effect for the Fe_2 probe in both oxidation states.

To investigate the possibility of CEST, ^{1}H NMR spectra were collected for aqueous 3.4 mM solutions of **1** or **2** with 100 mM HEPES and 100 mM NaCl buffered at pH 7.4, using presaturation at frequencies ranging from –100 to 100 ppm referenced to H_2O. The CEST spectrum, or Z-spectrum, shows the extent of H_2O signal intensity reduction with respect to the saturation frequency, or frequency offset. In the spectrum for **1**, three CEST peaks appear at 29, 40 and 68 ppm with 8.8, 10 and < 5% H_2O signal reduction, respectively (see Figure 3.11, upper). Note that any CEST effect stemming from the two upfield labile protons at −9.5 and 8.5 ppm are likely masked by direct saturation of H_2O. In comparison, two CEST peaks are present in the CEST spectrum for **2**, centered at 74 and 83 ppm with 21 and 22% H_2O signal reduction, respectively (see Figure 3.11, lower). Using the Omega plot method,[19] the proton exchange rates were estimated as 6.5(8) × 10^2 (29 ppm) and 5.0(8) × 10^2 (40 ppm) s^{-1} for **1**, and 6.8(9) × 10^2 (74 ppm) and 7.0(8) × 10^2 (83 ppm) s^{-1} for **2**, respectively (see Figures 3.12–13), in agreement with rates reported in mononuclear Fe^{II} carboxamide PARACEST agents.[33] Most importantly, the orthogonality of CEST peaks for **1** and **2** suggests the possibility for ratiometric measurements.

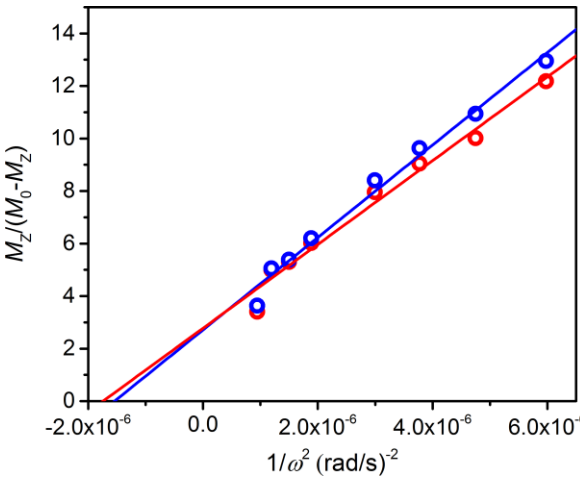

Figure 3.13 Omega plot of the CEST effect at 74 ppm (red) and 83 ppm (blue) of 4.0 mM **2** in pH 7.4 H_2O with 100 mM HEPES and 100 mM NaCl. Circles represent experimental data and lines represent linear fits.

The open-circuit potential (OCP) of an electrochemical cell provides an experimental measure of the reducing or oxidizing nature of the solution environment. For a system at equilibrium, the OCP represents a collective measure of the ratio between the oxidized and reduced forms of each redox-active species and follows the Nernst equation. Therefore, we constructed a ratiometric calibration curve over a range of OCPs centered around the $Fe^{II}Fe^{II}/Fe^{II}Fe^{III}$ redox couple. Specifically, we collected CEST spectra for a series of solutions containing 100 mM HEPES, 100 mM NaCl, and selected ratios of 1:2 (total [Fe_2] = 4.9 mM) in the range 9:1–1:9, and then correlated these spectral ratios to OCPs obtained independently using

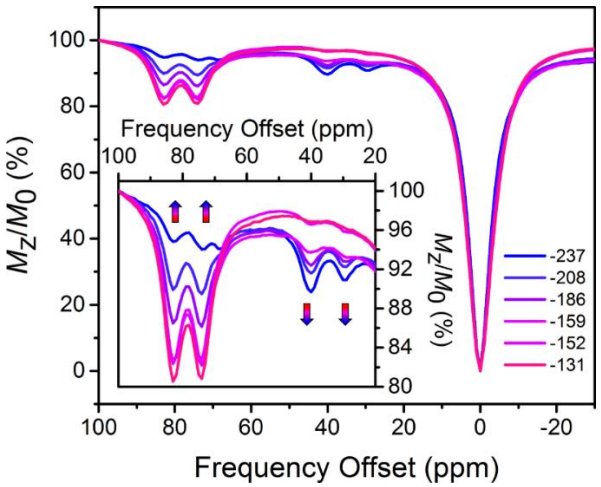

Figure 3.14 CEST spectra collected at 37 °C for 4.9 mM aqueous solutions of **1** and **2** at pH 7.4, with ratios of **1**:**2** from 9:1 (blue) to 1:9 (red). The legend gives the independently obtained OCP of each sample (mV vs NHE). Inset: Expanded view of the relevant CEST peaks.

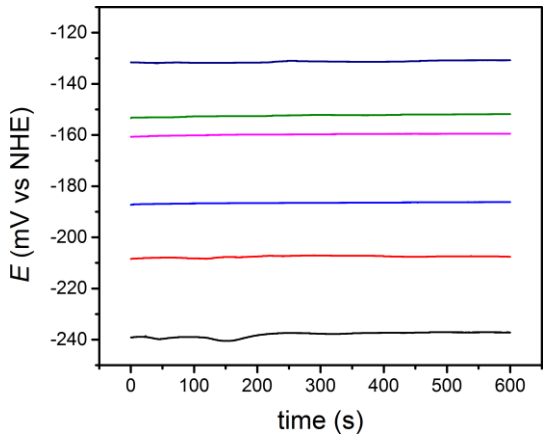

Figure 3.15 OCPs of solutions containing overall 4.9 mM Fe_2, with the ratio of **1**:**2** ranging from 9:1 (bottom most) to 1:9 (top most), are monitored over time upon mixing (at 0 s). Each solution contains 100 mM NaCl and 100 mM HEPES buffered at pH 7.4.

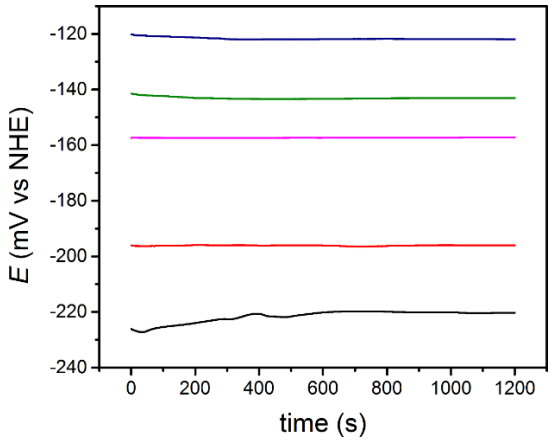

Figure 3.16 OCPs of solutions containing overall 3.8 mM Fe_2, with the ratio of **1**:**2** ranging from 9:1 (bottom most) to 1:9 (top most), are monitored over time upon mixing (at 0 s). Each solution contains 100 mM NaCl and 100 mM HEPES buffered at pH 7.5.

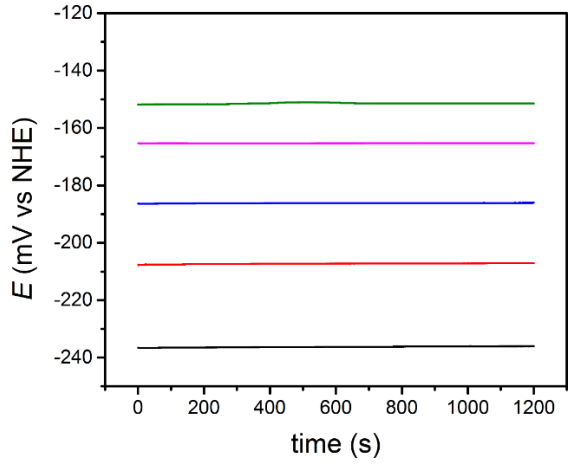

Figure 3.17 OCPs of solutions containing overall 2.6 mM Fe_2, with the ratio of **1**:**2** ranging from 9:1 (bottom most) to 1:9 (top most), are monitored over time upon mixing (at 0 s). Each solution contains 100 mM NaCl and 100 mM HEPES buffered at pH 7.3.

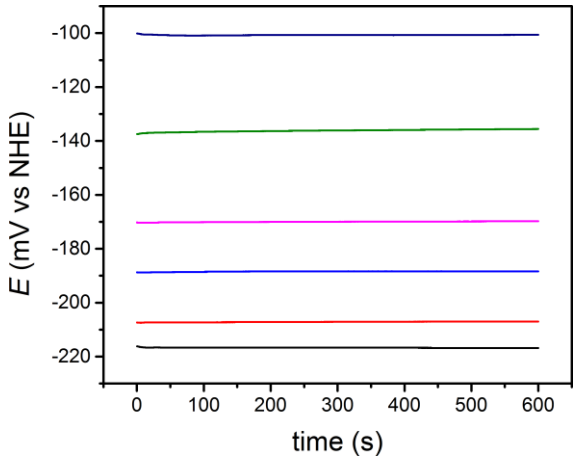

Figure 3.18 OCPs of solutions containing overall 10 mM Fe_2, with the ratio of **1**:**2** ranging from 9:1 (bottom most) to 1:9 (top most), are monitored over time upon mixing (at 0 s). Each solution contains 100 mM NaCl and 100 mM HEPES buffered at pH 7.4

a potentiostat (see Figure 3.14). Importantly, note that the OCP values stabilized within a variation of <1 mV after seconds, suggesting relatively fast kinetics toward reaching equilibrium (see Figures 3.15–18). As the OCP becomes more reducing (i.e. a higher fraction of **1**), the CEST intensity at 74 and 83 ppm monotonically decreases with a concomitant increase in intensity at 29 and 40 ppm. To construct a calibration curve, the ratio of %CEST effect at 83 and 40 ppm ($CEST_{83\ ppm}/CEST_{40\ ppm}$) were plotted as a function of OCP (see Figure 3.19). The corresponding data follow Nernstian behavior, and can therefore be fit to the following equation where OCP varies linearly with the semilog of $CEST_{83\ ppm}/CEST_{40\ ppm}$:

$$OCP\ (mV) = 40.1\ln(CEST_{83\ ppm}/CEST_{40\ ppm}) - 208 \quad (1)$$

The effectiveness of Eq. 1 in quantitation of OCP in the presence of potassium superoxide and cysteine were examined. First, a solution containing 4 mM of **1** was incubated with 1 mM of KO_2 in pH 7.4 buffer. The resulting CEST spectrum exhibits CEST peaks at 74 and 83 ppm, in addition to those from **1**, arise from the oxidation product LFe_2(etidronate) (see Figure 3.20). The %CEST

at 83 and 40 ppm are 7.1 and 5.3, respectively, resulting in a calculated OCP of –219 mV based on Eq. 1, which is in excellent agreement with the experimentally determined OCP, –225 mV. In another sample, 4 mM of **2** was incubated with 200 mM of cysteine in pH 7.4 buffer. The calculated OCP based on %CEST at 83 and 40 ppm and Eq. 1 was –187 mV, which is in good agreement with the experimental OCP, –204 mV (see Figure 3.21). Both reactions exhibit reasonable equilibration rate, with the KO_2 oxidation reaching equilibrium in 10 minutes and the cysteine reduction in 50 minutes, as evidenced by the stabilization of OCP (see Figure 3.22). Above evidences confirm the responsiveness of the Fe_2 probe towards thiol and superoxide, as well as the capability of Eq. 1 to quantitate solution OCP dictated by thiol-based reductants and reactive oxygen species-based oxidants.

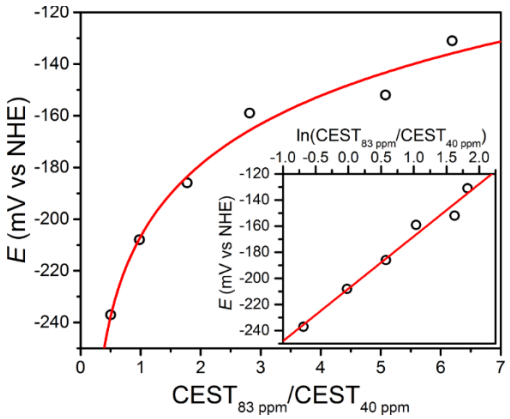

Figure 19. Open-circuit potential (OCP) of aqueous Fe_2 samples vs ratios of CEST peak intensities from presaturation at 83 and 40 ppm. Inset: Semilog form of the plot. Black circles represent experimental data; red lines represent fits.

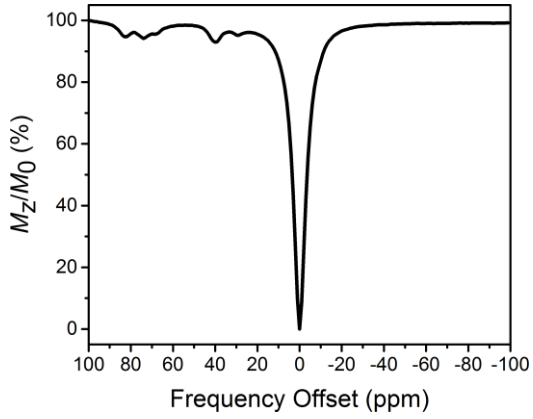

Figure 3.20 CEST spectra collected at 37 °C for a sample containing 4 mM of **1** mixed with 1 mM of KO_2 in a solution containing 100 mM HEPES and 100 mM NaCl buffered at pH 7.4. Refer to the CEST experimental section for details on baseline correction.

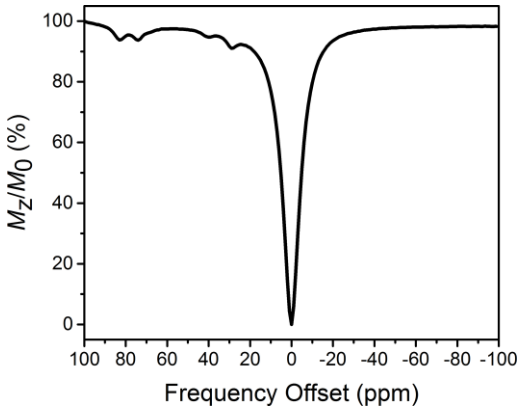

Figure 3.21 CEST spectra collected at 37 °C for a sample containing 4 mM of **2** mixed with 200 mM of cysteine in a solution containing 100 mM HEPES and 100 mM NaCl buffered at pH 7.4. Refer to the CEST experimental section for details on baseline correction.

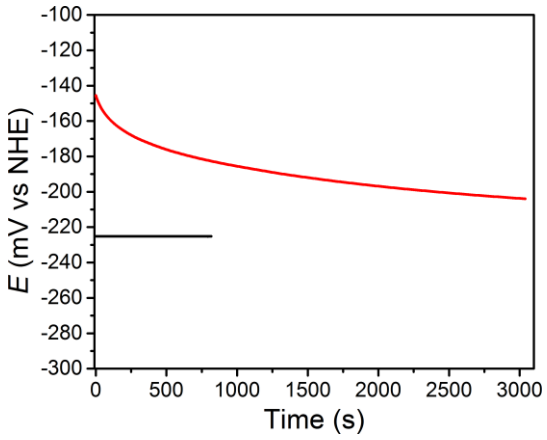

Figure 3.22 OCPs of two solutions containing 4 mM **1** with 1 mM KO_2 (black) and 4mM **2** with 200 mM cysteine (red) are monitored over time upon mixing (at 0 s). Measurements were stopped when OCP varied less than 1 mV within 5 minutes. Each solution contains 100 mM NaCl and 100 mM HEPES buffered at pH 7.4.

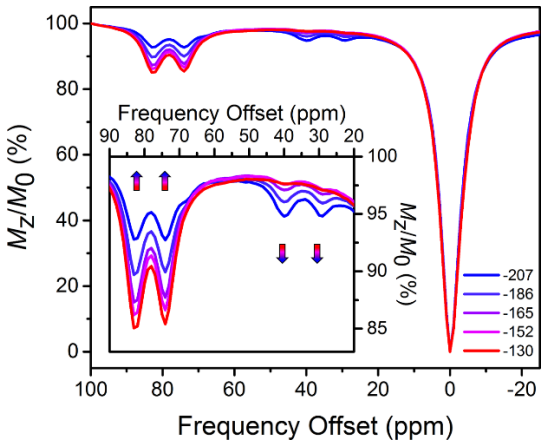

Figure 3.23 CEST spectra for 2.6 mM aqueous solutions of **1** and **2**, with ratios of **1**:**2** from 9:1 (blue) to 1:9 (red) at 37 °C. Each solution contains 100 mM NaCl and 100 mM HEPES buffered at pH 7.3. The legend gives the independently obtained OCP of each sample (mV vs NHE). Inset: Expanded view of the relevant CEST peaks.

We next sought to determine how factors such as pH and temperature affect this calibration curve, as these factors exhibit slight heterogeneity in physiological conditions. Most notably, pH affects the exchange rate of CEST-active protons, which leads to changes in CEST peak intensities. However, such changes can be partially compensated by taking the ratio of two CEST peaks in the event that both are altered to similar degree. To investigate pH effects, two series of solutions, buffered at pH 7.3 and 7.5, respectively, were prepared analogously to those at pH 7.4. Fits of the obtained OCPs as a function of $CEST_{83\ ppm}/CEST_{40\ ppm}$ for the two series gave the

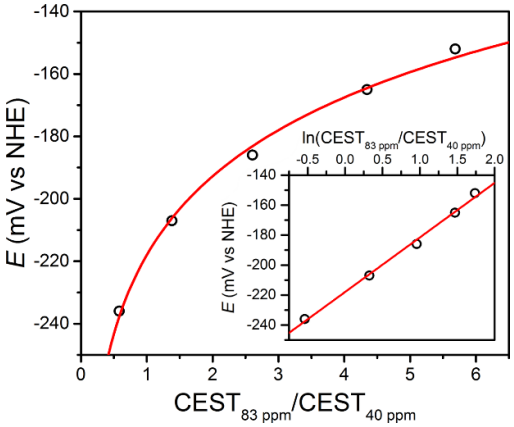

Figure 3.24 Open circuit potentials for solutions, containing 100 mM HEPES, 100 mM NaCl and 2.6 mM Fe_2 buffered at pH 7.3 at 37 °C, is plotted against both the ratio of CEST effects from application of presaturation at 83 and 40 ppm and the natural log of the ratio (inset). Black circles and the red line represent the experimental data and the fit, respectively.

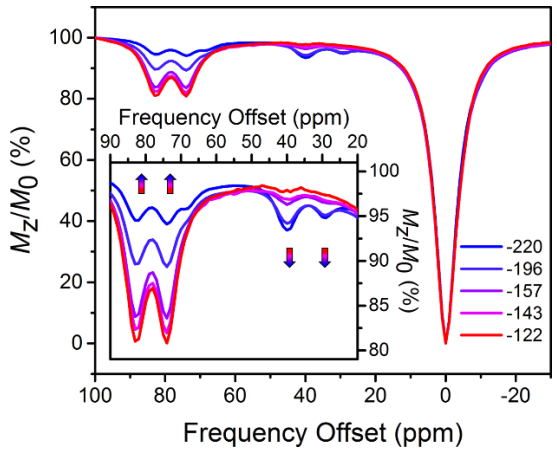

Figure 3.25 CEST spectra for 3.8 mM aqueous solutions of **1** and **2**, with ratios of **1**:**2** from 9:1 (blue) to 1:9 (red) at 37 °C. Each solution contains 100 mM NaCl and 100 mM HEPES buffered at pH 7.5. The legend gives the independently obtained OCP of each sample (mV vs NHE). Inset: Expanded view of the relevant CEST peaks.

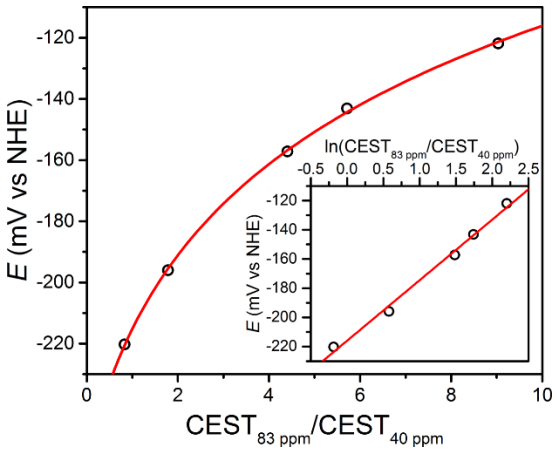

Figure 3.26 Open circuit potentials for solutions, containing 100 mM HEPES, 100 mM NaCl and 3.8 mM Fe_2 buffered at pH 7.5 at 37 °C, is plotted against both the ratio of CEST effects from application of presaturation at 83 and 40 ppm and the natural log of the ratio (inset). Black circles and the red line represent the experimental data and the fit, respectively.

following two Nernstian equations (see Figures 3.23–26):

$$\text{pH 7.3: OCP (mV)} = 36.4\ln(\text{CEST}_{83\ \text{ppm}}/\text{CEST}_{40\ \text{ppm}}) - 218 \quad (2)$$

$$\text{pH 7.5: OCP (mV)} = 41.5\ln(\text{CEST}_{83\ \text{ppm}}/\text{CEST}_{40\ \text{ppm}}) - 216 \quad (3)$$

Eq. 1, 2 and 3 are summarized in Figure 3.27. For a given $\ln(\text{CEST}_{83\ \text{ppm}}/\text{CEST}_{40\ \text{ppm}})$ value, the maximum deviation in OCP over the entire range of potentials was found to be ca. 20 mV. This value represents the maximum expected error introduced into the calibration curve by pH inhomogeneity of 7.3–7.5.

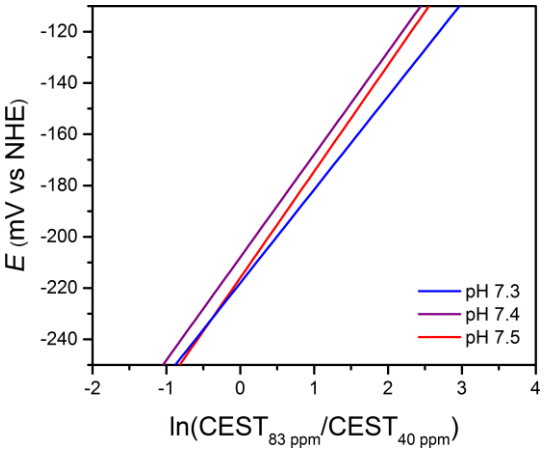

Figure 3.27 Comparison of Nernstian fits (from Figures 3.19, 3.24, and 3.26) obtained from data at various pH values.

In addition to pH, temperature can also alter the intensity and frequency offset of the CEST peak, owing to increased proton exchange rate and the

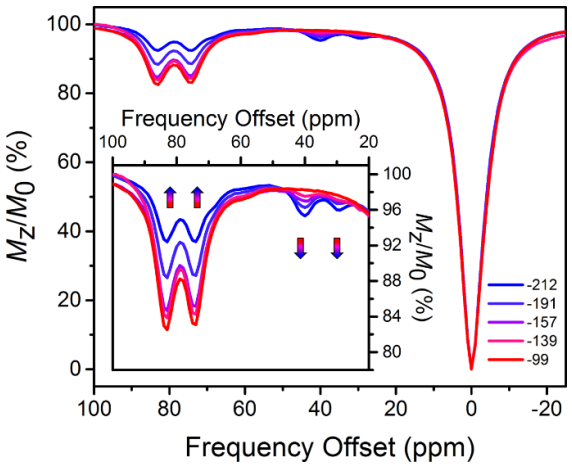

Figure 3.28 CEST spectra for 3.8 mM aqueous solutions of **1** and **2**, with ratios of **1**:**2** from 9:1 (blue) to 1:9 (red) at 35 °C. Each solution contains 100 mM NaCl and 100 mM HEPES buffered at pH 7.5. The legend gives the independently obtained OCP of each sample (mV vs NHE). Inset: Expanded view of the relevant CEST peaks.

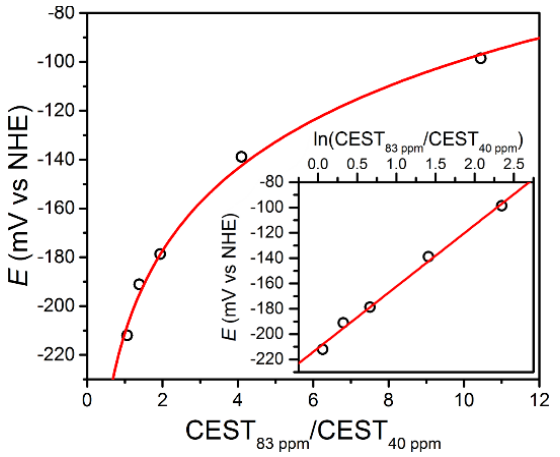

Figure 3.29 Open circuit potentials for solutions, containing 100 mM HEPES, 100 mM NaCl and 3.8 mM Fe_2 buffered at pH 7.5 at 39 °C, is plotted against both the ratio of CEST effects from application of presaturation at 83 and 40 ppm and the natural log of the ratio (inset). Black circles and the red line represent the experimental data and the fit, respectively.

temperature dependence of hyperfine shift.[12] To investigate effects from temperature variation, the data collected at pH 7.5, which feature slightly more significant CEST effects due to base-catalyzed proton exchange mechanism, were examined at 35 and 39 °C, respectively. Note that the CEST peak at 83 ppm at 37 °C shifted to 84 and 82 ppm at 35 and 39 °C, respectively, while the variable-temperature shift in the CEST peak at 40 ppm was insignificant (see Figures 3.28–31). Fits of the OCP vs $CEST_{83\ ppm}/CEST_{40\ ppm}$ plots for data obtained at 35 and 39 °C gave the following two Nernstian equations (see Figures 3.28–31):

$$35\ °C:\ OCP\ (mV) = 59.9\ln(CEST_{83\ ppm}/CEST_{40\ ppm}) - 246 \quad (4)$$

$$39\ °C:\ OCP\ (mV) = 48.6\ln(CEST_{83\ ppm}/CEST_{40\ ppm}) - 211 \quad (5)$$

Using the same analysis used in the pH series, for a given $\ln(CEST_{83\ ppm}/CEST_{40\ ppm})$ value, the largest deviation in the OCP readout was found to be ca. 40 mV (see Figure 3.32).

The kinetic and thermodynamic properties of **1** and **2** towards ions, air and reductants were

examined by comparison of electronic absorption and NMR spectra. In the presence of 4 mM of the ions $H_2PO_4^-/HPO_4^{2-}$, CO_3^{2-}, SO_4^{2-}, CH_3COO^-, or Ca^{2+} incubated at 37 °C for 12 hours, 4 mM of **1** or **2** in solutions buffered at pH 7.4 or D_2O show identical NMR spectra to solutions containing the respective Fe_2 complex with no added ions (see Figures 3.33–36). The experiments demonstrate the high stability of the Fe_2 complexes towards physiological ions of millimolar concentrations.[34] Finally, the observation of CEST effect from **1** and **2** were confirmed in bovine blood plasma (see Figure 3.37). While the baseline is broader than CEST spectra obtained from buffers, presumably due to the presence of additional exchangeable protons from proteins in the plasma, the CEST effect from **1** and **2** can be unambiguously observed and are comparable to those obtained in buffers.

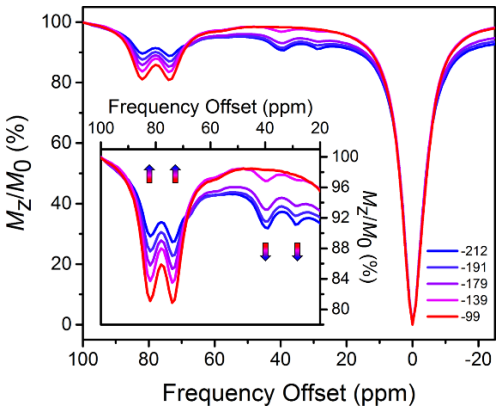

Figure 3.30 CEST spectra for 3.8 mM aqueous solutions of **1** and **2**, with ratios of **1**:**2** from 9:1 (blue) to 1:9 (red) at 39 °C. Each solution contains 100 mM NaCl and 100 mM HEPES buffered at pH 7.5. The legend gives the independently obtained OCP of each sample (mV vs NHE). Inset: Expanded view of the relevant CEST peaks.

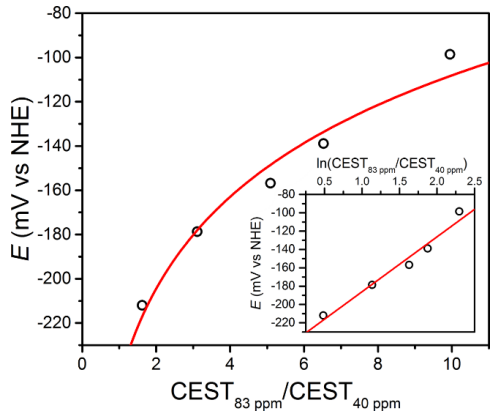

Figure 3.31 Open circuit potentials for solutions, containing 100 mM HEPES, 100 mM NaCl and 3.8 mM Fe_2 buffered at pH 7.5 at 35 °C, is plotted against both the ratio of CEST effects from application of presaturation at 83 and 40 ppm and the natural log of the ratio (inset). Black circles and the red line represent the experimental data and the fit, respectively.

While ions do not introduce interference to the stability of **1** and **2**, the $Fe^{II}Fe^{III}/Fe^{III}Fe^{III}$ redox couple (209 mV vs NHE) makes oxidation of **2** in air a concern, which was studied by electronic absorption spectroscopy. A solution buffered at pH 7.4 containing 0.4 mM of **2** was prepared in a nitrogen glove box and exposed to air while a UV-Vis-NIR spectrum was recorded at 2 h intervals (see Figure 3.38, lower). Over the course of 40 h, the absorption at 801 nm gradually disappeared, while the absorption at 470 nm shifted to ca. 460 nm and decreased in intensity. These spectral changes proceed through an isosbestic point at 445 nm, suggesting a clean conversion to a single, new species. Indeed, a similarly buffered solution containing 0.4 mM of **3** showed an identical UV-Vis-NIR spectrum to that of the 40 h oxidation product of **2** (see Figure 3.38), demonstrating that

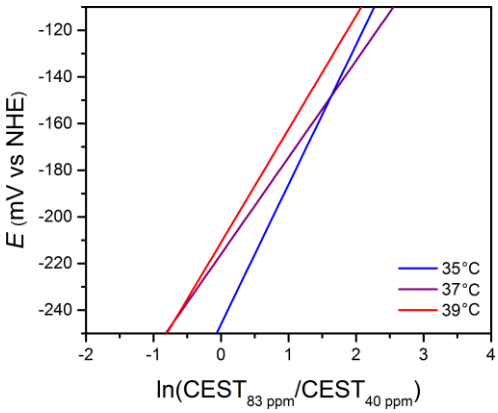

Figure 3.32 Comparison of Nernstian fits (from Figures 3.19, 3.29 and 3.31) obtained from data at various temperatures.

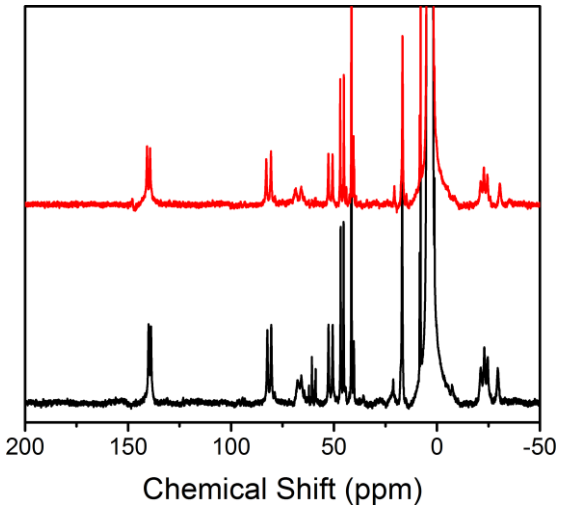

Figure 3.33 ^{1}H NMR spectra of 4 mM of **1** in D_2O with (top) and without (bottom) presences of 4 mM of each NaOAc, Na_2CO_3, NaH_2PO_4 and Na_2SO_4.

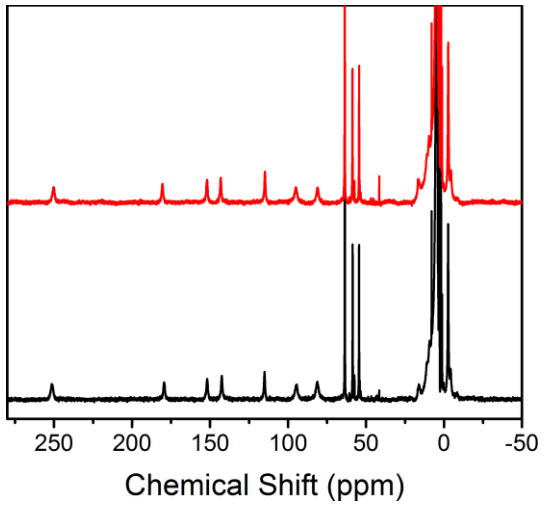

Figure 3.34 ^{1}H NMR spectra of 4 mM of **2** in D_2O with (top) and without (bottom) presences of 4 mM of each NaOAc, Na_2CO_3, NaH_2PO_4 and Na_2SO_4.

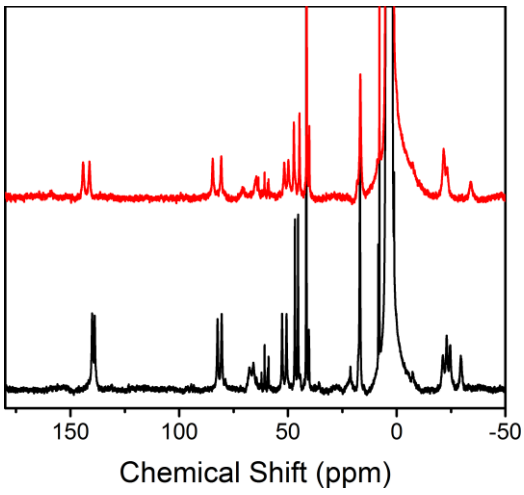

Figure 3.35 NMR spectra of 4 mM of **1** in D_2O with (top) and without (bottom) presences of 4 mM of $Ca(NO_3)_2$.

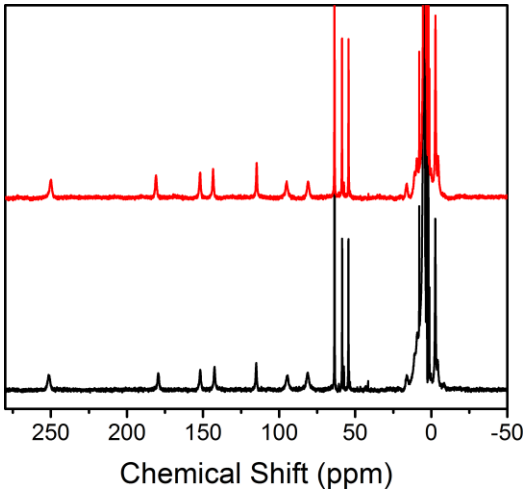

Figure 3.36 NMR spectra of 4 mM of **2** in D_2O with (top) and without (bottom) presences of 4 mM of $Ca(NO_3)_2$.

2 is cleanly oxidized to the stable **3** in air. Moreover, the reversibility of this oxidation was demonstrated by in situ reduction of **3** by glutathione, as monitored by NMR spectroscopy (see Figure 3.39). This redox reversibility suggests the potential utilization of **3** as a probe precursor, which is stable in air and could undergo reduction to the CEST-active $Fe^{II}Fe^{III}$ upon introduction into the reducing extracellular environment of tissue.

To further examine the possibility of using **3** as a probe precursor, we carried out preliminary cell viability experiments using melanoma B16F10 cells as a model. After incubating the cells with media containing various concentrations of **3**, the percentages of viable cells were recorded (see Figure 3.40). In the presence of 8.2 mM of **3**, ca. 80% of cells are viable, and this percentage increased up to ca. 90% for samples containing lower concentrations of **3**. Overall > 80% viability within millimolar probe

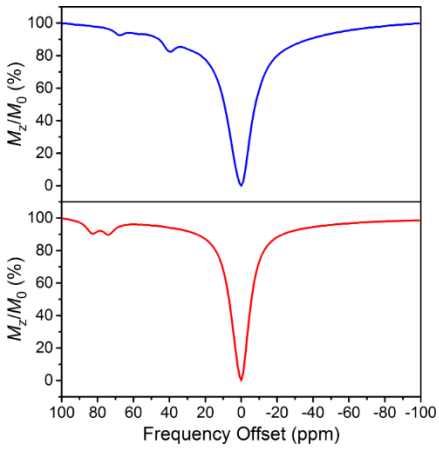

Figure 3.37 CEST spectra collected at 37 °C for solutions containing 4.0 mM of **1** (top) and **2** (bottom) in bovine blood plasma at pH 7.4.

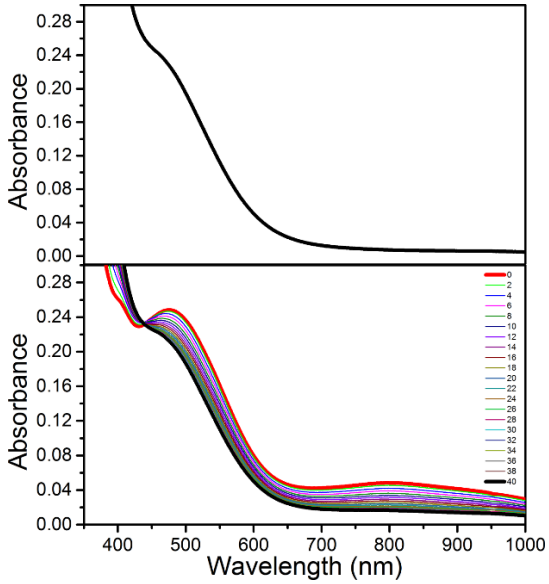

Figure 3.38 UV-Vis-NIR spectra of 0.4 mM of **3** (top) and 0.4 mM of **2**, buffered at pH 7.4 with different hours of air exposure (bottom, legend indicates hours of exposure).

concentration range is quite promising, as this is the concentration in which PARACEST probes show optimal contrast.

Finally, we sought to investigate whether the favorable CEST properties of the Fe_2 probe observed on a 9.4 T NMR spectrometer could also be realized on phantom images from a 9.4 T preclinical MRI scanner. A series of solutions containing overall 10 mM Fe_2 with 1:2 ratio ranging from 9:1 to 1:9 were prepared similarly to those in the NMR study. For each sample, two images were acquired with a 14 μT presaturation pulse applied at frequencies of 40 and 83

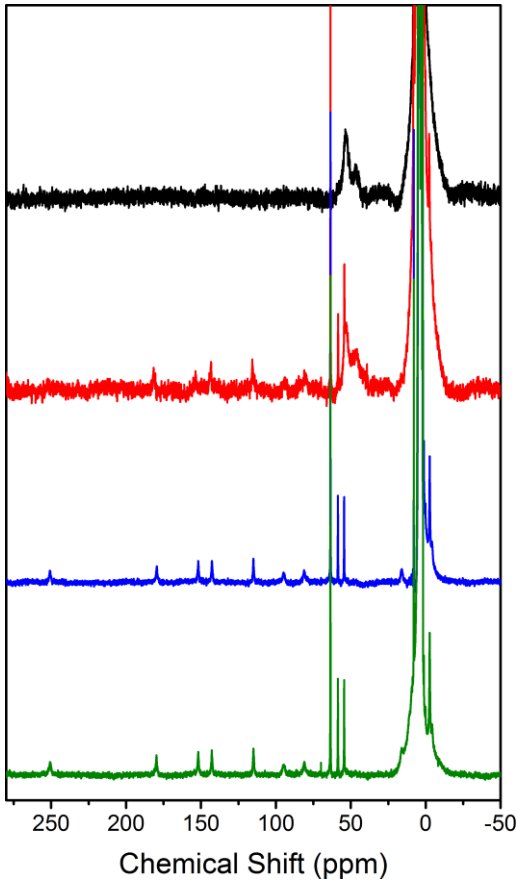

Figure 3.39 Stacked NMR spectra for 4 mM of **3** in D_2O in the presence of 0 (black), 4 (red), 8 (blue) and 16 (green) mM of glutathione monosodium salt, which is used to avoid acidity build-up caused by glutathione in an unbuffered solution.

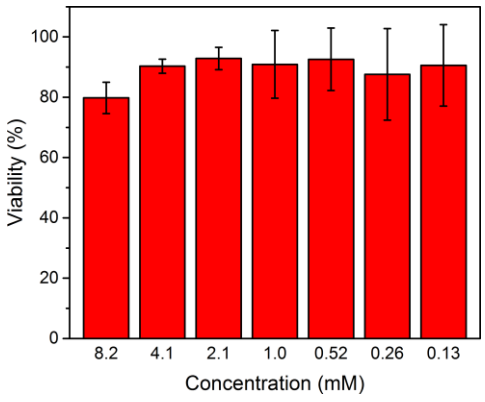

Figure 3.40 Cells survival (in %) after incubation with different concentrations of **3**.

ppm from the H_2O signal (see Figure 3.41). Control images were acquired at the respective presaturation frequencies with 0 μT power. Presaturation at 40 and 83 ppm reduced the H_2O intensity up to ca. 4 and 8%, respectively, demonstrating that CEST effects from both Fe^{II}_2 and $Fe^{II}Fe^{III}$ redox states can be observed on a MRI scanner. However, the inhomogeneity of phantom intensities, likely stemming from weak CEST effects and therefore a noisy background, makes the contrast across phantoms virtually indistinguishable. Despite the ambiguous visualization of trend in redox status, the OCPs independently measured by a potentiosat can be plotted against the ratios between averaged phantom intensities from 83 and 40 ppm ($CEST_{83\ ppm}/CEST_{40\ ppm}$) to give a Nernstian fit resembling eqs. 1–5 (see Figure 3.42). Furthermore, the OCPs calculated from the calibration, using intensities from phantom, fall in relatively good agreement with the OCPs measured by a potentiostat (see Table 3.1). Future efforts will aim to improve homogeneity of phantom images by increasing CEST through combination of chemical and pulse sequence optimizations.

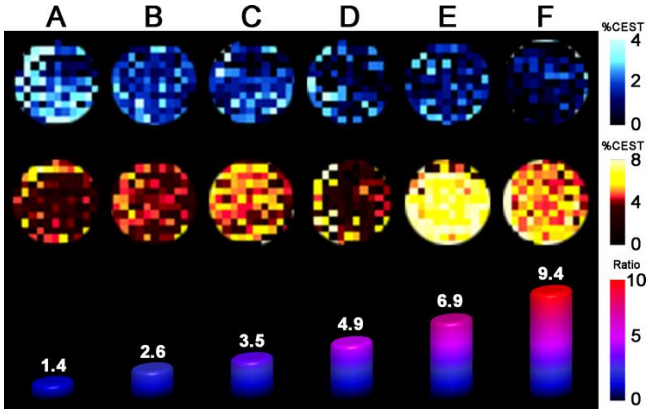

Figure 3.41 Phantom images of solutions containing 10 mM of Fe_2 with **1**:**2** ratios ranging from 9:1 to 1:9 (A–F). Top and middle rows of images represent CEST effects with 14 μT presaturation at 40 and 83 ppm, respectively. The bars along the bottom row represent the ratio of average %CEST for presaturation at 40 and 83 ppm.

Table 3.1 Comparison of OCP values obtained by Nernstian equation from CEST imaging vs those obtained by potentiostat

OCP (vs NHE)	**A**	**B**	**C**	**D**	**E**	**F**
CEST imaging	−263	−213	−188	−161	−133	−107
potentiostat	−222	−201	−188	−170	−135	−101

3.4 Conclusion

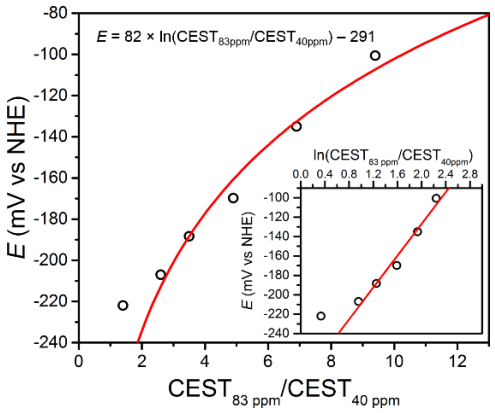

Figure 3.42 Open circuit potentials for solutions for phantom experiments, containing 100 mM of HEPES, 100 mM of NaCl and 10 mM of Fe_2 buffered at pH 7.4, is plotted against both the ratio of CEST effects at 37 °C from the averaged phantom image intensity with presaturation at 83 and 40 ppm and the natural log of the ratio (inset). Black circles and the red line represent the experimental data and the fit (equation displayed), respectively. Refer to Experimental Section for fitting details.

The foregoing results demonstrate the feasibility of using the Nernst equation to correlating OCP with the ratio of CEST effects from a Fe_2 PARACEST probe, in a range spanning ca. –120 to –230 mV vs NHE. To our knowledge, this study provides the first demonstration of ratiometric quantitation of solution redox status through NMR/MRI measurables. The CEST-active mixed-valence compound **2** is enabled by the presence of fast electron transfer and magnetic coupling to the neighboring fast-relaxing Fe^{II} center, as evidenced by NMR and electronic absorption studies. The potential applicability of the Fe_2 probe is further highlighted by the potential utilization of the air-stable $[Fe^{III}_2]^+$ complex as a one-electron oxidized probe precursor, which shows low cell-toxicity and excellent redox reversibility. Finally, a Nernstian calibration curve was constructed using averaged CEST effects from phantom images, and OCPs obtained from this curve are in good agreement with those obtained from a potentiostat.

Whereas the current Fe_2 probe provides a promising proof-of-concept for quantitation of redox status, perhaps most exciting is that the dinucleating ligand scaffold provides an excellent platform for chemically tuning the $Fe^{II}Fe^{II}/Fe^{II}Fe^{III}$ redox couple. Toward this end, preliminary experiments show that the $Fe^{II}Fe^{II}/Fe^{II}Fe^{III}$ redox couple can be varied over a 120 mV range through either introduction of other bisphosphonate derivatives or chemical modification of the dinucleating

ligand. Current work is geared toward tailoring members of this family of molecules to target optimal redox properties and proton exchange properties for *in vivo* applications.

Chapter Four: Effect of Magnetic Coupling on Water Proton Relaxivity in a Series of Transition Metal Gd^{III} Complexes

Reprinted with permission from:

Lilley, L. M.; Du, K.; Krzyaniak, M. D.; Parigi, G.; Luchinat, C.; Harris, T. D.; Meade, T. J.

Inorg. Chem. **2018**, *57*, 5810-5819.

This work was performed in collaboration with the co-authors lised above.

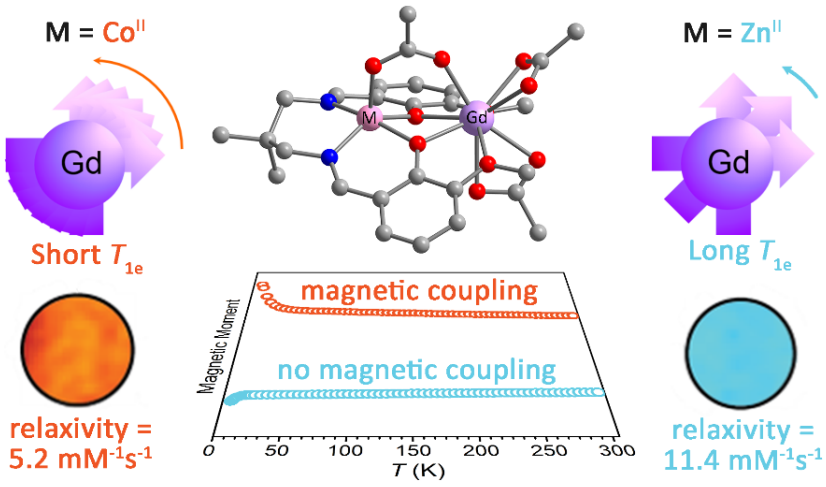

4.1 Introduction

Magnetic resonance imaging (MRI) is a staple of preclinical and clinical diagnostic radiology due to its tunable soft tissue contrast and high spatial resolution. The need to differentiate regions of tissues or organs that are magnetically similar but histologically distinct, has been a major impetus for the development of contrast enhancement agents. Paramagnetic agents such as gadolinium [Gd^{III}] complexes are often used (> 40% of the 50 million clinical procedures performed annually) to decrease the T_1 of adjacent protons, resulting in increased signal intensity (brightness) in the vicinity of the agent.[1]

The vast majority of Gd^{III} agents are anatomical reporters and are designed to highlight regions of interest such as vasculature and tumors. Our laboratory has developed conditionally activated (or bioresponsive) probes that report on the *in vivo* physiological and biochemical status of whole animals in the form of an acquired MR image.[2] The use of these probes in intact organisms (combined with a modality that provides high spatiotemporal resolution) has resulted in a deeper understanding of the specific roles of *in vivo* gene expression and fluctuations in ion concentration in normal and pathological physiology.[3–5]

Current efforts toward developing responsive or bio-activated Gd^{III} agents focuses on optimizing several molecular parameters associated with paramagnetic Gd^{III} chelates. These parameters include the number of inner-sphere water molecules (q), the rotational correlation time of the complex (τ_r), and the mean residence lifetime of the aqua ligand (τ_m).[6–8] To date, numerous examples of MR molecular probes that modulate q in response to enzymatic activities,[4, 9–11] ion binding,[12–16] and pH[17–19] have been reported. Further, τ_r enhancement has been explored through

molecular interactions with endogenous proteins,[20, 21] and nanoparticle platforms[22, 23] to create high signal probes.

In order to maximize the signal enhancement in the acquired MR image using bioresponsive agents, the second- and outer-coordination sphere contributions of Gd^{III} (which represent background signal in the image) must be minimized. For example, small-molecule agents at clinical field strengths (1–3 T), the outer-sphere contribution to the observed relaxation enhancement of water protons is ca. 45%.[6, 24] Therefore, when employing bioresponsive agents *in vivo* the background signal from outer-sphere water can be misinterpreted for the agent having been activated by an enzyme, or other physiologically relevant ions. In other words, we designed this new class of probes with exceptionally low-background signal to minimize the ambiguity in MR images where an observed signal enhancement (brighter) can be the result of either high Gd^{III} complex concentrations, or the activation of the bioresponsive agent being turned "on."

The electronic relaxation time (τ_s) of a contrast agent represents a key physical property that governs both the inner-sphere, (described by Solomon-Bloembergen-Morgan (SBM) theory), and outer-sphere, (as described by the Freed and Bryant equations) relaxation enhancement of bulk water. Modulation of q, τ_r or τ_m has created numerous bioresponsive probes by tuning the inner-sphere contribution to relaxivity. However, manipulating the value of τ_s of a contrast agent can provide a unique opportunity to exploit both the inner- and outer-sphere contributions. Therefore, a mechanism that can modulate τ_s in response to a biochemical event is desirable as it would enable researchers to suppress undesired signal for developing highly responsive MR probes.

According to SBM theory, τ_s of a paramagnetic center contributes to the overall correlation time (τ_c) of the molecule according to Eq. 1:

$$(\tau_c)^{-1} = (\tau_m)^{-1} + (\tau_r)^{-1} + (\tau_s)^{-1} \quad (1)$$

At clinical magnetic field strengths of 1.5 and 3 T, the optimal relationship for maximum contrast is $(\tau_m)^{-1} < (\tau_r)^{-1} \leq (\tau_s)^{-1}$, such that $\tau_c \approx 10^{-9}$ s.[25–28] For small molecular Gd^{III} complexes, such as the clinically-employed contrast agent $[(DOTA)Gd^{III}]^-$ (H_4DOTA = 1,4,7,10-tetraazacyclododecane-1,4,7,10-tetraacetic acid), values for τ_m, τ_r, and τ_s are typically measured to be on the order of ca. 10^{-7}, 10^{-10} and 10^{-9} s, respectively.[29] Accordingly, reduction in τ_s in a contrast agent will result in deviation of the optimal correlation times, and will thus lead to ineffective ^1H relaxation of the molecule and low signal.

One method to decrease τ_s in a molecular complex is through the introduction of magnetic exchange coupling between multiple paramagnetic metal centers. Here, the presence of magnetic exchange coupling gives rise to low-lying excited states through which spins can relax.[30] Indeed, a number of multinuclear complexes that feature magnetic coupling between paramagnetic metal centers have been shown to exhibit smaller values of τ_s relative to the constituent metal ions,[31–33] and we recently employed this strategy to develop a Cu^{II}_2-based chemical exchange saturation transfer (CEST) MR agent.[34]

Similarly, the introduction of magnetic coupling into Gd-containing multinuclear complexes should give rise to a shortening a τ_s and a subsequent decrease in relaxivity. Merbach and coworkers explored this concept in trinuclear Gd^{III} complexes where they found the weak magnetic coupling (0.033 cm^{-1}) between unpaired electrons in the 4f orbitals to be insufficient to engender measurable effects on proton relaxivity.[35] Other reported examples of multinuclear contrast agents with no magnetic coupling likewise exhibited very small reductions in measured τ_s values.[36, 37]

In contrast to the magnetic superexchange between lan-thanides, a transition metal-lanthanide superexchange coupling can be much stronger (up to $|J| = 7.0\ cm^{-1}$) owing to the radially diffuse 3d orbitals in first-row transition metals.[38–41] In principle, for a complex that features magnetic exchange between Gd^{III} and a paramagnetic transition metal ion the decrease in τ_s of the Gd^{III} ion induced by exchange coupling varies with the spin quantum number of the transition metal (STM), the exchange constant (J) of the coupling, and the electronic relaxation time of the transition metal (τ_s').[28, 30, 42] Accordingly, the coupling constant (J) and the electronic structure of the transition metal (STM and τ_s') can be synthetically tuned to modulate τ_s of Gd^{III}. To achieve this we proposed to employ dinuclear complexes where the Gd^{III} center is magnetically coupled to a divalent first row transition metal, M^{II}, as a strategy to reduced τ_s of Gd^{III} for the potential application of low-background Gd^{III} contrast agents.

Bimetallic complexes of dinucleating salen derivatives (2,2′-ethylenebis(nitrilomethylidene)diphenol N,N′ethylenebis(salicylimine)) have been shown to display significant magnetic coupling. Therefore, we selected a series of salen-based dinuclear complexes of the general formula $LMGd(\mu\text{-}O_2CCH_3)(O_2CCH_3)_2$[41, 43] (Figure 4.1) to investigate the correlation between M and the resulting τ_s of Gd^{III}. Here, we should note that these complexes are intended to demonstrate a proof-of-concept and are not suitable for direct use in a biological system. Three first-row transition metals were chosen for this study: Co^{II} ($\tau_s \sim 10^{-12}$ s), Cu^{II} ($\tau_s \sim 10^{-9}$ s), and Zn^{II} as a diamagnetic control.[30] We hypothesized that Co^{II}, with a τ_s value typically over three orders of magnitude faster than Gd^{III} would reduce the τ_s of Gd^{III} to the greatest extent. In addition, while Gd^{III} complexes are our primary focus, the analogous complexes $LMDy(\mu$-

$O_2CCH_3)(O_2CCH_3)_2$ (M = Co, Cu, Zn) were prepared for solution-state determination of *q* and the complex LZnEu(μ-$O_2CCH_3)(O_2CCH_3)_2$ was prepared to elucidate the solution-state structure.

4.2 Experimental Section

General Considerations. Unless otherwise noted, syntheses and manipulations were carried out in an MBraun LABstar glovebox operated under a humid dinitrogen atmosphere. The ligand LH_2 was synthesized following a modified literature procedure.[44] Dioxygen was removed from H_2O through at least three successive freeze-pump-thaw cycles. Anhydrous organic solvents were dried using a solvent purification system from Pure Process Technology. The solvents H_2O (10% ^{17}O) and CD_3OD were purchased from Cambridge Isotope Laboratories, Inc. The compound $Gd(O_2CCH_3)_3{\cdot}4H_2O$ was purchased from Strem Chemical Inc. All other reagents and solvents were purchased from Sigma Aldrich and used without further purification.

Synthetic procedures. **6,6'-((1E,1'E)-((2,2-dimethylpropane 1,3-diyl)bis(azanylylidene))bis(methanylylidene))bis(2-methoxyphenol)** (LH_2). To a stirring solution of o-vanillin (15 g, 98 mmol) in 200 mL anhydrous MeOH under an inert atmosphere, 2,2-dimethyl-1,3-propanediamine (5.0 g, 49 mmol) in 30 mL of dry MeOH was added dropwise via a syringe. The reaction was stirred at room temperature for 24 hours producing a yellow/orange solution. The MeOH was removed in vacuo and the resulting yellow residue was recrystallized from hot toluene to yield the product as yellow block-like crystals in 87% yield (Figure 4.1). ^1H NMR (500 MHz, Chloroform-*d*) δ 14.12 (s, 2H), 8.29 (d, J = 1.4 Hz, 2H), 6.89 (dd, J = 7.8, 1.6 Hz, 2H), 6.85 (dd, J = 7.9, 1.5 Hz, 2H), 6.77 (t, J = 7.8 Hz, 2H), 3.88 (s, 6H), 3.46 (d, J = 1.2 Hz, 4H), 1.04 (s, 6H). ^{13}C NMR (126 MHz, $CDCl_3$) δ 165.80, 152.05, 148.47, 122.92, 118.40, 117.90,

113.81, 67.31, 56.03, 36.17, 24.25. ^{1}H NMR and ^{13}C NMR spectra were obtained at 25 °C on a Bruker Avance III 500 MHz NMR spectrometer.

LCoGd(μ-O_2CCH_3)(O_2CCH_3)$_2$·0.7MeCN (**1**). LH_2 (100 mg, 0.27 mmol) and Co(O_2CCH_3)$_2$·4H_2O (67 mg, 0.27 mmol) were dissolved in MeOH (6 mL) in a 20 mL scintillation vial fit with a stir bar. The reaction was sealed with a Teflon cap and heated to 30 °C with stirring for 10 minutes. The reaction was then stirred at ambient temperature for 1 hour to produce an amber solution. Gd(O_2CCH_3)$_3$·4H_2O (90 mg, 0.27 mmol) was then added to the solution, and after stirring for 16 h, the solvent was removed under reduced pressure to give a red-orange residue. The residue was dissolved in MeCN (1 mL), and the resulting solution was filtered through a column of diato-maceous earth. Vapor diffusion of Et_2O into the filtrate afforded an amber crystalline solid, which was collected by vacuum filtration and dried under reduced pressure to give **1** (190 mg, 87%). FT-IR (ATR, cm^{-1}): 3016 (w), 2898 (w), 1652 (m), 1586 (m), 1475 (s), 1444 (s), 1343 (m), 1255 (s), 1102 (m), 765 (s). Anal. Calcd. $C_{28.4}H_{35.1}GdN_{2.7}O_{10}Co$; C, 43.14; H, 4.47; N, 4.77 %. Found: C, 43.03; H, 4.40; N, 4.77%. ESI-MS (positive mode): m/z = 703.058 g/mol (M-O_2CCH_3). Vapor diffusion of Et_2O into a dilute MeCN (4 mL) solution of the red-orange residue from above gave amber rod-shaped crystals of LCoGd(μ-O_2CCH_3)(O_2CCH_3)$_2$·0.6MeCN that were suitable for single-crystal X-ray diffraction analysis.

LCuGd(μ-O_2CCH_3)(O_2CCH_3)$_2$·0.8MeCN (**2**). LH_2 (100 mg, 0.27 mmol) and Cu(O_2CCH_3)$_2$·H_2O (54 mg, 0.27 mmol) were dissolved in MeOH (6 mL) in a 20 mL scintillation vial fit with a stir bar. The reaction was sealed with a Teflon cap and heated to 30 °C with stirring for 10 minutes. The reaction was then stirred at ambient temperature for 1 hour to produce a blue-green precipitate. Gd(O_2CCH_3)$_3$·4H_2O (90 mg, 0.27 mmol) was then added to the reaction mixture,

which was stirred for 16 hour to yield a blue-green solution. The solvent was removed under reduced pressure to give a blue-green residue. The residue was dissolved in MeCN (1 mL), and the resulting solution was filtered through a column of diatomaceous earth. Vapor diffusion of Et_2O into the filtrate afforded a blue-green crystalline solid, which was collected by vacuum filtration and dried under reduced pressure to give **2** (180 mg, 83%). FT-IR (ATR, cm^{-1}): 2983 (w), 2886 (w), 1661 (m), 1588 (m), 1479 (s), 1444 (m), 1345 (m), 1259 (s), 1102 (s), 1004 (m), 767(s). Anal. Calcd. $C_{28.9}H_{36.2}GdN_{2.8}O_{10}Cu$; C, 43.05; H, 4.52; N, 4.93 %. Found: C, 43.03; H, 4.53; N, 4.94 %. Vapor diffusion of Et_2O into a dilute MeCN (4 mL) solution of the blue-green residue from above gave blue-green rod-shaped crystals of $LCuGd(\mu\text{-}O_2CCH_3)(O_2CCH_3)_2$ that were suitable for single-crystal X-ray diffraction analysis.

$LZnGd(\mu\text{-}O_2CCH_3)(O_2CCH_3)_2\cdot 0.1MeCN$ (**3**). This complex was prepared in air. LH_2 (100 mg, 0.27 mmol) and $Zn(O_2CCH_3)_2\cdot H_2O$ (54 mg, 0.27 mmol) were dissolved in MeOH (6 mL) in a 25 mL round bottom flask fit with a stir bar. The reaction was heated to 30 °C for 10 minutes, and stirred at ambient temperature for 1 hour to produce a yellow solution. $Gd(O_2CCH_3)_3\cdot 4H_2O$ (90 mg, 0.27 mmol) was added to the solution, and after stirring for 12 hours, the solvent was removed under reduced pressure to give a yellow residue. The residue was dissolved in MeCN (1 mL), and the resulting solution was filtered through a column of diatomaceous earth. Vapor diffusion of Et_2O into the filtrate afforded a colorless crystalline solid, which was collected by vacuum filtration and dried under reduced pressure to give **3** (190 mg, 88%). FT-IR (ATR, cm^{-1}): 3028 (w), 3001 (w), 1659 (m), 1591 (m), 1473 (s), 1448 (s), 1343 (m), 1257 (s), 1100 (m), 773 (s). Anal. Calcd. $C_{27.5}H_{34}GdN_{2.1}O_{10}Zn$; C, 42.42; H, 4.40; N, 3.93 %. Found: C, 42.43; H, 4.41; N, 3.83 %. ESI-MS (positive mode): m/z = 708.051 g/mol ($M\text{-}O_2CCH_3$). Vapor diffusion of Et_2O into a dilute

MeCN (4 mL) solution of the colorless residue from above gave colorless rod-shaped crystals of LZnGd(μ -O_2CCH_3)(O_2CCH_3)$_2$·0.9MeCN that were suitable for single-crystal X-ray diffraction analysis.

LCoDy(μ-O_2CCH_3)(O_2CCH_3)$_2$·0.7MeCN (**4**). LH_2 (100 mg, 0.27 mmol) and Co(O_2CCH_3)$_2$·H_2O (67 mg, 0.27 mmol) were dissolved in MeOH (6 mL) in a 20 mL scintillation vial fit with a stir bar. The reaction was sealed with a Teflon cap and heated to 30 °C with stirring for 10 minutes. The reaction was then stirred at ambient temperature for 1 hour to produce an amber solution. Dy(O_2CCH_3)$_3$·xH_2O (46 mg, 0.27 mmol) was added to the solution, and after stirring for 16 hours, the solvent was re-moved under reduced pressure to give an amber residue. The residue was dissolved in MeCN (1 mL), and the resulting solution was filtered through a column of diatoma-ceous earth. Vapor diffusion of Et_2O into the filtrate afforded an orange crystalline solid, which was collected by vacuum filtration and dried under reduced pressure to give **4** (190 mg, 86%). FT-IR (ATR, cm^{-1}): 2983 (w), 2886 (w), 1661 (s), 1558 (m), 1479 (s), 1345 (m), 1259 (s), 1102 (m), 767 (s). Anal. Calcd. $C_{28.9}H_{36.9}DyN_{2.8}O_{10}Co$; C, 43.05; H, 4.53; N, 4.94 %. Found: C, 43.05; H, 4.53; N, 4.94 %. ESI-MS (positive mode): m/z = 709.064 g/mol (M–O_2CCH_3).

LCuDy(μ-O_2CCH_3)(O_2CCH_3)$_2$·2.6H_2O (**5**). LH_2 (100 mg, 0.27 mmol) and Cu(O_2CCH_3)$_2$·4H_2O (67 mg, 0.27 mmol) were dissolved in MeOH (6 mL) in a 20 mL scintillation vial fit with a stir bar. The reaction was sealed with a Teflon cap and heated to 30 °C with stirring for 10 minutes. The reaction was then stirred at ambient temperature for 1 hour to produce a blue-green precipitate. Dy(O_2CCH_3)$_3$·xH_2O (46 mg, 0.27 mmol) was then added to the reaction mix-ture, which was stirred for 16 hours to yield a blue-green solution. The solvent was removed under

reduced pressure to give a blue-green residue. The residue was dissolved in MeCN (1 mL), and the resulting solution was filtered through a column of diatomaceous earth. Vapor diffusion of Et_2O into the filtrate afforded a blue-green crystalline solid, which was collected by vacuum filtration and dried under reduced pressure to afford **5** (180 mg, 80%). FT-IR (ATR, cm^{-1}): 2979 (w), 2942 (w), 1619 (m), 1556 (m), 1437 (s), 1415 (s), 1309 (m), 1223 (s), 1066 (m), and 744 (s). Anal. Calcd. $C_{27}H_{38.1}DyN_2O_{10}Cu$; C, 39.64; H, 4.70; N, 3.43 %. Found: C, 39.53; H, 4.03; N, 3.49 %.

$LZnDy(\mu\text{-}O_2CCH_3)(O_2CCH_3)_2\cdot 0.21MeCN\cdot 0.38H_2O\cdot 0.22MeOH$ (**6**). This compound was prepared in air. LH_2 (100 mg, 0.27 mmol) and $Zn(O_2CCH_3)_2\cdot H_2O$ (54 mg, 0.27 mmol) were dissolved in MeOH (6 mL) in a 25 mL round bottom flask fit with a stir bar. The reaction was heated to 30 °C for 10 minutes, and stirred at ambient temperature for 1 hour to produce a yellow solution. $Dy(O_2CCH_3)_3\cdot xH_2O$ (46 mg, 0.27 mmol) was added to the solution, and after stirring for 12 hours, the solvent was removed under reduced pressure to give a yellow residue. The residue was dissolved in MeCN (1 mL), and the resulting solution was filtered through a column of diatoma-ceous earth. Vapor diffusion of Et_2O into the filtrate afforded a colorless crystalline solid, which was collected by vacuum filtration and dried under reduced pressure to give **6** (180 mg, 82%). FT-IR (ATR, cm^{-1}): 2979 (w), 2942 (w), 1619 (m), 1556 (m), 1437 (s), 1415 (m), 1309 (m), 1223 (s), 1066 (m), 744 (s). Anal. Calcd. $C2_{7.78}H_{35.6}DyN_{2.21}O_{10}Zn$; C, 41.78; H, 4.49; N, 3.88 %. Found: C, 41.78; H, 4.49; N, 3.89%. ESI-MS (positive mode): m/z = 714.058 g/mol ($M\text{-}O_2CCH_3$).

$LZnEu(\mu\text{-}O_2CCH_3)(O_2CCH_3)_2\cdot 0.1MeCN\cdot 0.17H_2O$ (**7**). This compound was prepared in air. LH_2 (100 mg, 0.27 mmol) and $Zn(O_2CCH_3)_2\cdot H_2O$ (54 mg, 0.27 mmol) were dissolved in MeOH (6 mL) in a 25 mL round bottom flask fit with a stir bar. The reaction was heated to 30 °C for 10

minutes, and then stirred at ambient temperature for 1 hour to produce a yellow solution. $Eu(O_2CCH_3)_3 \cdot xH_2O$ (90 mg, 0.27 mmol) was added to the solution, and after stirring for 16 hours, the solvent was removed under reduced pressure to give a yellow residue. The residue was dissolved in MeCN (1 mL), and the resulting solution was filtered through a column of diatomaceous earth. Vapor diffusion of Et_2O into the filtrate afforded a colorless crystalline solid, which was collected by vacuum filtration and dried under reduced pressure to give **7** (180 mg, 86%). FT-IR (ATR, cm^{-1}): 3032 (w), 2960 (w), 1677 (m), 1659 (m), 1471 (s), 1448 (m), 1343 (m), 1259 (s), 1100 (m), 773 (s). Anal. Calcd. $C_{27.21}H_{33.67}DyN_{2.12}O_{10}Zn$; C, 41.78; H, 4.49; N, 3.88 %. Found: C, 44.23; H, 4.41; N, 3.83 %. ESI-MS (positive mode): m/z = 703.048 g/mol ($M\text{-}O_2CCH_3$). Vapor diffusion of Et_2O into a dilute MeCN (4 mL) solution of the colorless residue from above gave colorless rod-shaped crystals of $LZnEu(\mu\text{-}O_2CCH_3)(O_2CCH_3)_2 \cdot 1.5MeCN$ that were suitable for single-crystal X-ray diffraction analysis.

NMR Spectroscopy. Total NMR structural elucidation of **7** was completed to verify that no lanthanide dissociated from the O_4 (2-phenoxo and 2-methoxo) binding pocket. **7** was the only complex with linewidths acceptable for 2D NMR analysis. 2D experiments were performed in methanol-d_4 on a 400 MHz Agilent DD MR-400 system equipped with autoX probe (COSY, TOCSY, NOESY) and an Agilent DD2 500 MHz for HSQC and HMBC data. The chemical shifts of 7 dissolved in D_2O were inferred based on the assignment made in methanol-d_4. 2D NMR experiments were not successful in D_2O due to rapid relaxation times.

The number of bound H_2O molecules (q) was measured by VT ^{17}O NMR of aqueous solutions of **4**, **5**, and **6**. Dy^{III} analogues were utilized to measure q due to suitable line shape (in the range of 30–40 Hz) of the ^{17}O peak. In the N_2 glovebox, saturated solutions of the complexes were pre-

pared with freeze-pump-thawed D_2O, doped with 1 % ^{17}O H_2O. The solutions were filtered using a 5 μm syringe filter and transferred to J. Young NMR tubes. VT-NMR experiments were performed using Agilent DD MR-400 system equipped with an autoX probe. Each sample was heated to 80 °C and allowed to equilibrate for 10 minutes to ensure that H_2O molecules were in the fast-exchanging regime. ^{17}O NMR spectra were collected for each sample. The ^{17}O chemical shifts (in ppm) for diamagnetic control were, –2.74 (4), –4.701 (5) and –3.53 (6). The molar ratio of compound (P_m) was determined using ICP-MS and $\langle S_Z \rangle$ used for Dy^{III} was 28.565. Calculated values for q were reported in Table 4.1.

Relaxivity Measurements at 1.4 T. Saturated aqueous solutions of **1**, **2**, and **3** were prepared in an MBraun LAB-star glovebox and filtered through 5 μm syringe filters. Serial dilutions were prepared four times to produce 500 μL of five sample concentrations. The sample tubes were sealed under inert atmosphere and removed from the glovebox. Analogous solutions of 1:1 $M(O_2CCH_3)_2/Gd(O_2CCH_3)_3$ were prepared; M = Co, Cu, and Zn. The samples were then incubated at 37 °C for 30 minutes and the T_1 and T_2 relaxation times were measured on a Bruker mq60 NMR analyzer equipped with Minispec V2.51 Rev.00/NT software (Billerica, MA, U.S.A.) operating at 1.41 T (60 MHz) and at 37 °C. T_1 was measured by an inversion recovery pulse sequence (t1_ir_mb) with a final pulse separation $\geq 5T_1$. T_2 relaxation was measured by the Carr-Purcell-Meiboom-Gill (CPMG) pulse sequence (t2_cpmb). The T_1 and T_2 relaxation rates were plotted as a function of the Gd^{III} concentration determined by ICP-MS. r_1 and r_2 were determined from the slopes of the linear fits of three independent replicates.

Relaxivity measurements at 7 T. Samples were prepared the same as the 1.4 T measurements but were performed on an 89-mm-bore-size PharmaScan 7.05 T MRI spectrometer fitted with

shielded gradient coils (Bruker Bio-Spin, Billerica, MA) using a RF RES 300 1H 089/023 quadrature transmit/receive mouse brain volume coil (Bruker BioSpin, Billerica, MA). Image acquisition was performed using Paravision 5.0.1 software (Bruker Bio-Spin, Billerica, MA). T_1 and T_2 weighted images were acquired using a rapid-acquisition rapid-echo variable repetition time (RAREVTR) and multi slice multi echo pulse sequences respectively. RARE scan = 13 factor = 1, echo time = 11 ms, averages = 3, matrix size (MTX) = 128 × 128, field of view = 25 mm × 25 mm, six slices, slice thickness = 1.5 mm, interslice distance = 2.0 mm, repetition times = 15000, 10000, 8000, 6000, 3000, 1500, 1000, 750, 500, 300, 200, and 150 ms, and a total scan time of ∼1 hour and 32 minutes. T_1 values of selected regions of interest of five out of six slices were calculated using the T_1 saturation recovery monoexponential curve fitting formula provided by the image sequence analysis tool in Paravision 5.0.1 software. The 7 T T_1 and T_2 relaxation rates were plotted as a function of the Gd^{III} concentration determined by ICP-MS.

MR solution phantom imaging at 1.5 T. Samples of **1**, **2** and **3** were prepared (1 mM) in 15 mL conical tubes for imaging in a 70-cm-bore-size Aera 1.5 T MR spectrometer fitted with shielded gradient coils (Siemens Medical Solu-tions, Erlangen, DE) using a 4-channel receive only head matrix coil (Siemens). Image acquisition was performed using advanced mapping sequences using Siemens Syngo software. T_1 images were acquired using a saturation recovery sequence with variable TR's ranging from 25 ms to 1500 ms. Selection of this range of TR's was chosen to accurately sample the spin-lattice relaxation recovery curve with short T_1 values. The echo time was set to ~2 ms for all scans. All images were acquired in 2D with in-plane resolution of 900 μm, slice thickness = 4 mm (n = 3 slices). Maps were generated using Xinapse JIM software and least square fitting using standard MR signal equations.

Nuclear Magnetic Relaxation Dispersion (NMRD). NMRD profiles were obtained using a Stelar Spinmaster fast field cycling FFC 200-1T relaxometer by measuring the water ^{1}H longitudinal relaxation rates of aqueous solutions containing **1** (2.31 mM), **2** (0.64 mM) or **3** (0.58 mM) as a function of the applied magnetic field, in a range corresponding to proton Larmor frequencies from 0.01 to 40 MHz (ca. 2×10^{-4}–1 T). The relaxivity profiles were obtained by normalization of the relaxation rate data, subtracted by the diamagnetic contribution, to the Gd^{III} concentration determined by ICP-MS. The measurements were performed at 25 and 37 °C. The measurement error was below 1%.

UV-Vis Spectroscopy. UV-Vis spectra were obtained for aqueous solutions of LH_2, **1**, **2** and **3** on an Agilent 8453 UV-Vis in an air-free cuvette dissolved in freeze pump thawed milliQ water. Air stability of **2** and **3** was evaluated over two weeks after exposing the solutions to air.

Inductively Coupled Plasma – Mass Spectrometry (ICP-MS). ICP-MS samples were prepared by dissolving 10 μL aliquots of sample in concentrated HNO_3 (300 μL) in a 15 mL conical tube and digested at 60 °C for 1 hour. Samples were diluted to a total volume of 10 mL with MilliQ water and analyzed using a computer-controlled Thermo iCAP Q ICP-MS. Data was acquired using one survey run (10 sweeps) and three main (peak jumping) runs (100 sweeps). Isotopes selected for analysis were $^{157,158}Gd$, ^{163}Dy, ^{153}Eu, ^{59}Co, ^{68}Zn, ^{65}Cu, ^{89}Y, ^{115}In and ^{159}Tb - the latter three elements were used for internal calibration.

W-band Electron Paramagnetic Resonance Spectroscopy (EPR). 1 mM aqueous stock solutions of each complex (**1**, **2** and **3**) were prepared using MilliQ water in an inert atmosphere; the solutions were diluted to a final concentration of 400 μM and freeze-pump-thawed three times. The solutions were transferred to quartz EPR tubes and sealed with Teflon. Continuous wave EPR

(cw-EPR) spectra were collected at room temperature with a Bruker E-680X/W outfitted with a cylindrical resonator (EN-680-1021H), the experimental parameters used were: 0.05 mW of power; 4 G magnetic field modulation amplitude at 100kHz; and a time constant of 40.96 ms and time constant of 163.84 ms. The cw-EPR lineshapes were modeled in Easyspin using a single isotropic $S = {}^1/_2$ electron spin convoluted with a Lorentzian lineshape, where the linewidth parameter is defined as the full width at half-max.[45]

Magnetic Measurements. Magnetic measurements were performed using a Quantum Design MPMS-XL SQUID magnetometer. Polycrystalline samples were sealed in a polyethylene bag under a dinitrogen atmosphere. Approximately 10 mg of each compound was pulverized and weighed into a small polyethylene bag; exact weights were obtained to the nearest milligram. Variable temperature dc susceptibility data were measured from 1.8 to 300 K. Magnetic data was simulated using MagPro software[46, 47] to obtain coupling constant *J*. The Hamiltonians used were $\hat{H} = -2J\hat{S}_{Gd}\hat{S}_{M}$, where M is Co^{II} or Cu^{II}. Experimental errors were determined by averaging simulations of two independently prepared samples.

X-Ray Structure Determination. Single crystals of reported compounds were directly coated with Paratone-N oil and mounted on a MicroMountsTM rod. The crystallographic data were collected at 100 K on a Bruker APEX II diffractometer equipped with MoKα or CuKα sealed tube source. Raw data was integrated and corrected for Lorentz and polarization effects using Bruker APEX2 v. 2009.1.[48] SADABS[49] was use to apply multi-scan absorption correction. Space group assignments were achieved by examining systematic absences, E-statistics and successive refinement of the structure. Structures were solved by SHELXT[50] direct method and refined by SHELXL[51] within the OLEX interface. In cases where solvent molecules were severely

disordered, the solvent mask function was applied in the OLEX interface to calculate the void space for sol-vent molecules as well as averaged electron density found in such void. For the complexes LCoGd(μ-O_2CCH_3)(O_2CCH_3)$_2$, LZnGd(μ-O_2CCH_3)(O_2CCH_3)$_2$, and LZnEu(μ-O_2CCH_3)(O_2CCH_3)$_2$, there were determined to be 112.8, 156.6 and 129.1 electrons/unit cell (Z = 8 for all three complexes), corresponding to approximately 0.6, 0.9 and 1.5 molecule of CH_3CN/complex, respectively.

4.3 Results and Discussion

The ligand LH_2 was synthesized according to a modified literature procedure.[44] All dinuclear complexes were synthesized through a one-pot stepwise metalation by addition of transition metal(II) then lanthanide(III) acetate salts to H_2L. Here, the acetate anion acts as an internal base to deprotonate the two phenol protons on H_2L. Following metalation, slow diffusion of Et_2O vapor in concentrated MeCN solutions gave crystalline solids that were dried under reduced pressure to give the compounds **1**–**7**.

In the cases of **1**, **2**, **3**, and **7**, Et_2O diffusion into a dilute MeCN solution of the compound gave rod-shaped crystals, suitable for single-crystal X-ray diffraction analysis, of LCoGd(μ-O_2CCH_3)(O_2CCH_3)$_2$·0.6MeCN, LCuGd(μ-O_2CCH_3)(O_2CCH_3)$_2$, LZnGd(μ-O_2CCH_3)(O_2CCH_3)$_2$·0.9MeCN, and LZnEu(μ-O_2CCH_3)(O_2CCH_3)$_2$·1.5MeCN, respectively. The CoGd, ZnGd, and ZnEu compound crystallized in the space group $P2_1/n$, while the CuGd compound crystallized in the space group $P\bar{1}$.

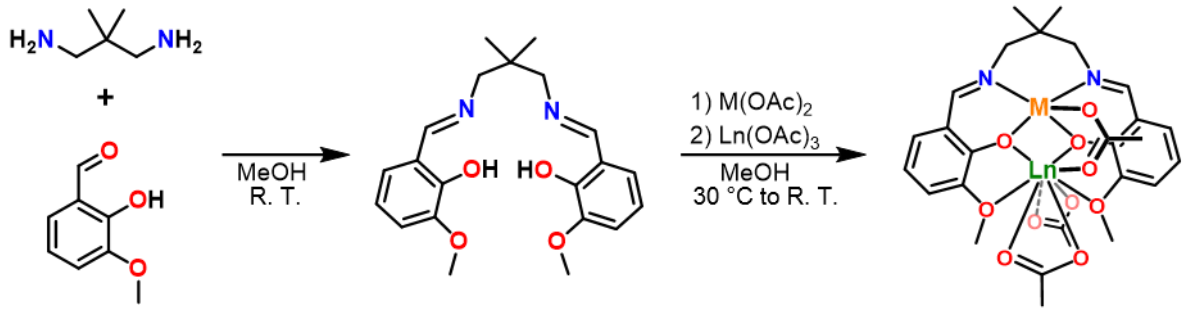

Figure 4.1 Synthetic scheme for the preparation and metalation of LH_2 to give the complexes $LMLn(\mu\text{-}O_2CCH_3)(O_2CCH_3)_2$, where M = Co^{II}, Cu^{II}, or Zn^{II} and Ln = Eu^{III}, Gd^{III}, or Dy^{III}.

The neutral complex in all complexes features a Gd^{III} ion that coordinated to nine O atoms (see Figure 4.2). Four coordination sites of Gd^{III} are occupied by O atoms from two phenoxo bridges and two phenyl methyl ether groups of L^-, while the remaining five sites are occupied by one O atom from a bridging μ-$O_2CCH_3^-$ ion and two κ^2-$O_2CCH_3^-$ ions.

Each divalent transition metal center resides in a pseudosquare pyramidal coordination geometry with the equatorial sites occupied by two imide N atoms and two bridging phenoxo O atoms afforded by L^-, and apical site occupied by an O atom from a μ-O_2CCH_3 ion. In the case of CoGd, ZnGd, and ZnEu complexes, the transition metal ion is significantly displaced out of the N_2O_2 plane, with M–Oacetate distances of 1.996(2), 1.978(4), and 1.980(2) Å, respectively. This distortion leads to the two N-bound C atoms of the propylene group to bend away from the square pyramid. By contrast, the Cu^{II} center in the CuGd complex is not nearly as displaced from the N_2O_2 pocket with a significant Jahn-Teller distortion giving a $Cu–O_{acetate}$ distance of 2.224(2) Å. Consequently, one N-bound C atom of the propylene group is bent away from the square pyramid, while the other is bent toward the pyramid. This conformational difference likely results in the lower-symmetry space group for the CuGd complex relative to the others.

The MLn complexes feature M-O-Ln angles of 103.27(7)° (CoGd), 103.44(9)° (CuGd), 103.3(2)° (ZnGd), and 103.34(9)° (ZnEu), and corresponding M···Gd distances of 3.4528(7),

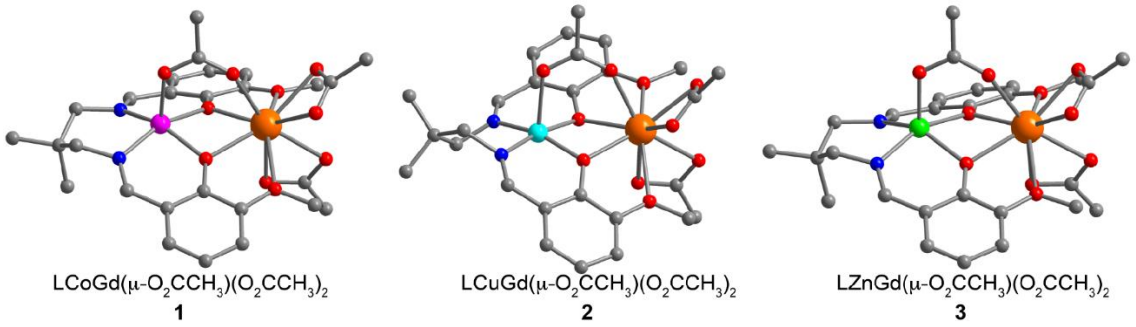

Figure 4.2 Crystal structures of LMGd(μ-O_2CCH_3)(O_2CCH_3)$_2$ complexes, where M = Co (left), Cu (middle) and Zn (right), as observed in single crystals grown from concentrated solutions of **1**, **2** and **3**, respectively. Orange, green, cyan, magenta, red, blue, and gray spheres represent Gd, Zn, Cu, Co, O, N, and C atoms, respectively; H atoms are omitted for clarity.

3.3911(4), 3.463(2), and 3.4787(5) Å. These structural parameters are consistent with related transition metal-lanthanide complexes.[41, 43] Moreover, the similar structural features across the family of complexes supports the validity of comparing values of relaxivity and q between different metal compositions.

In order to probe the magnetic interactions in **1** and **2**, dc magnetic susceptibility data were collected for solid-state samples (see Figure 4.3). The high temperature value of $\chi_M T$ for **1** and **2** are 10.27 and 8.06 cm^{3}K/mol, respectively, consistent with non-interacting spins of $S = {}^3/_2$ (Co^{II}) and $S = {}^7/_2$ (Gd^{III}) for **1** and $S = {}^1/_2$ (Cu^{II}) and $S = {}^7/_2$ (Gd^{III}) for **2**. For both compounds, $\chi_M T$ increases with decreasing temperature, albeit more rapidly for **2**, eventually reaching maxima of 11.27 cm^{3}K/mol (**1**) and 9.57 cm^{3}K/mol (**2**) at 10 K. Upon decreasing the temperature further, $\chi_M T$ undergoes a sharp downturn, reaching minima of 7.30 cm^{3}K/mol (**1**) and 9.87 cm^{3}K/mol (**2**) at 1.8 K.

The gradual increase of $\chi_M T$ value with decreasing temperature indicates the presence of ferromagnetic coupling between Gd^{III} and M^{II} centers. These interactions were modeled with the spin Hamiltonian $\hat{H} = -2J(\hat{S}_{Gd} \cdot \hat{S}_M)$[46, 47] to give exchange coupling constants of $J = +0.22$ cm^{-1} for

1 and J = +2.6 cm^{-1} for **2**. The much stronger coupling observed in **2** can likely be attributed to the large degree of orbital overlap between the p orbital on the phenoxo O atom and the singly occupied $d(x^2–y^2)$ on the Cu center.

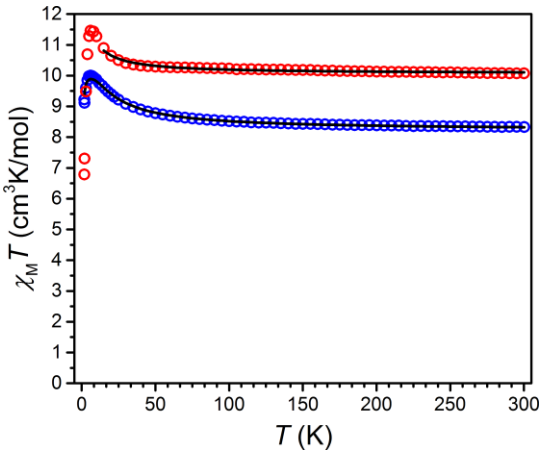

Figure 4.3 Variable temperature dc susceptibility data of **1** (red) and **2** (blue) measured at an applied field of 10,000 Oe. The black lines represent fits to the data.

While not explicitly modeled, the sharp downturn in $\chi_M T$ observed for both compounds likely stems from weak intermolecular antiferromagnetic coupling and zero-field splitting. The values of J obtained for **1** and **2** are comparable to those previously obtained for related dinuclear complexes.[38] Most importantly, the presence of significant exchange coupling for these complexes, particularly when paired with the inherently short τ_s of Co^{II} in **1**, may lead to a shortening of τ_s and thus decrease in relaxivity for Gd^{III} in solution.

Before determining τ_s and the resulting H_2O relaxation rate in **1**, **2** and **3**, the complex compositions in aqueous solution were examined by solution spectroscopic techniques. Compounds **1**, **2**, and **3** exhibited modest solubility in aqueous solution, leading us to suspect the coordinated acetates exchange with water to yield a tricationic complex of form $[LMGd(H_2O)_{5–6}]^{3+}$.

To examine this hypothesis, the solution structure of each complex was investigated by 2D NMR techniques to ensure the lanthanide was stable in the O_4 binding pocket afforded by $L^–$. Total NMR structural assignment was made in methanol-d_4 due to inadequate line shape in D_2O. ^1H assignments were made based on the correlations in the NOESY and TOCSY spectra coupled with

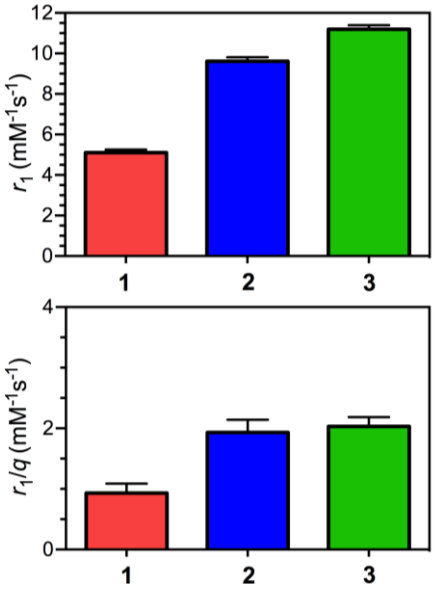

Figure 4.4 Relaxivity values of 1 mM aqueous solutions **1**, **2**, and **3** at 1.4 T and 37 °C. Measured r_1 values (top) and normalized r_1 to the number of inner-sphere waters, q (bottom). Error bars represent the standard deviation of three independent measurements (top) or propagated error (bottom).

the heteronuclear HSQC and HMBC. The rigidity of the structure results in integration doubling of chemically equivalent resonances. Three ^{1}H resonances at 6.2, 9.4 and 18.3 ppm in the methanol-d_4 spectrum were assigned to the bridging and capping acetates in **7**, consistent with 3 coordinating inequivalent acetates. In contrast, only one acetate resonance near 1 ppm was found in the D_2O spectrum of **7**, resembling a dissociated diamagnetic acetate resonance. Additionally, none of the integration doubling observed in the methanol-d_4 spectra was observed in D_2O. Thus, the rigidity of the complex is reduced and we attribute this result to the dissociation of $O_2CCH_3^-$ ions.

The precise number of bound water molecules in aqueous solution was determined by measuring the ^{17}O NMR chemical shifts of **4**, **5**, and **6**, which are the Dy^{III} analogues of **1**, **2** and **3**, respectively. The choice of Dy^{III} in place of Gd^{III} is to take advantage of the short τ_s of Dy^{III}, such that the ^{17}O resonances of bound water molecules can be observed. Saturated solutions of **4**, **5**, and **6** were found to exhibit values of q = 6, 5, and 5.6, respectively with an inherent error of 20% per the limitations of the technique. Additional support for the aqueous stability of $[LCoGd(H_2O)_6]^{3+}$ and $[LCuGd(H_2O)_5]^{3+}$ was evidenced by no significant changes in the UV-Vis spectra in aqueous solution over time.

After confirming the number of bound H_2O molecules in **1**, **2**, and **3** in aqueous solution, the ability of these complexes to increase the relaxation of bulk H_2O protons was evaluated. The

relaxivities (r_1) for samples containing **1**, **2** and **3** were found to be 5.2, 9.8 and 11.4 mM^{-1} s^{-1}, respectively (see Figure 4.4, upper). These values are high compared to conventional Gd^{III} contrast agents where $q \approx 1–2$, due to the high q values (~5–6) present in here. Nevertheless, the value of r_1 for **1** is remarkably less than half that for **3**, despite the structural similarities between the two compounds. By comparison, the r_1 for **2** is lower than that for **3**, but still considerably higher than r_1 for **1**. The reduction in r_1 for **1** is even more apparent when the values are normalized for q, with values of 0.9, 1.9, and 2.0 mM^{-1} s^{-1} for **1**, **2**, and **3**, respectively. Moreover, such a small value of r_1/q is remarkable when compared to the clinically employed agent $[Gd(DOTA)]^-$, which features r_1/q = 3.2 mM^{-1} s^{-1}.[52]

Relaxivities for aqueous solutions containing 1:1 $M(O_2CCH_3)_2$:$Gd(O_2CCH_3)_3$, where M = Co, Cu and Zn, were measured to verify that the observed modulation of r_1 for **1**, **2**, and **3** is not an intrinsic property of the free ions interacting in solution (see Figure 4.5). Importantly, the r_1 values for these mixtures show no correlation to the identities of M, in contrast to the r_1 comparison among **1**, **2** and **3**.[53]

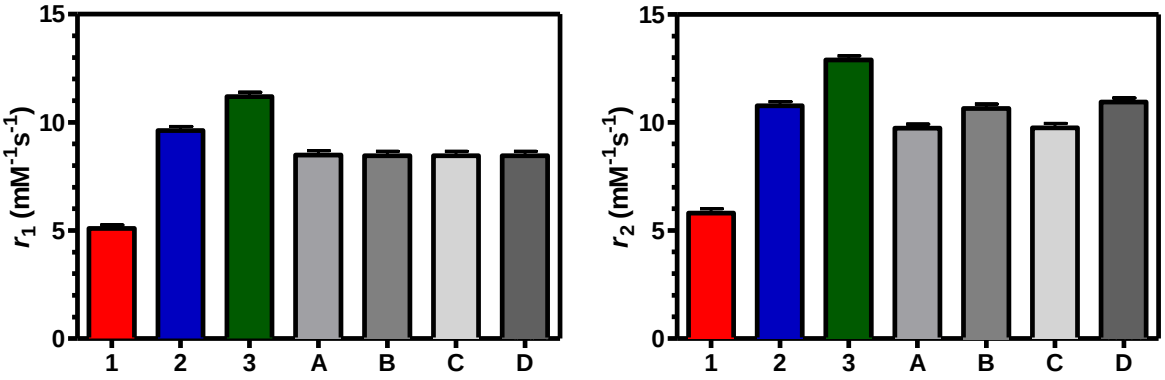

Figure 4.5 Relaxivity (r_1 left and r_2 right) measurements at 1.4 T of **1**, **2**, and **3** at 37 ºC. **A** (Co^{II}), **B** (Cu^{II}), and **C** (Zn^{II}), are aqueous solutions of 1:1 mixtures of transition metal and Gd^{III} acetate salts. **D** represents the relaxivity of aqueous Gd^{III} acetate at 1.4 T. These data reflect the decrease in relaxation enhancement as a function of magnetic exchange coupling between the metals. The relaxivity of the Co^{II} analogue **1** has a significantly lower r_1 ~5 $mM^{-1}s^{-1}$ versus the Cu^{II} and Zn^{II} analogue. The r_1 and r_2 values are approximately equal and follow the same trends as theory predicts. Error bars represent the standard deviation of three independent measurements.

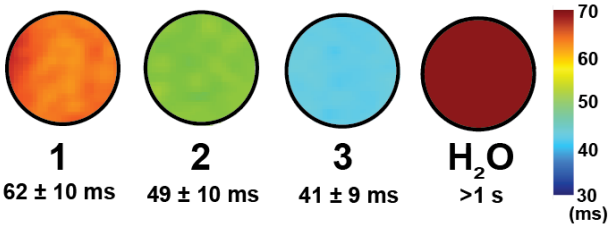

Figure 4.6 T_1 MR solution phantom images of **1**, **2**, and **3** at 1.5 T and ambient temperature. T_1 times represent averages over three slices with the associated standard deviation.

In addition, MR solution phantom images at 1.5 T offer visual evidence that **1** features the smallest relaxation enhancement of the three compounds (see Figure 4.6). The T_1 values were measured at ambient temperature, and as such cannot be directly compared to the relaxivity meas-urements at 37 °C.

At high magnetic field, the proton Larmor frequency increases while τ_s slows dramatically. If the difference in r_1 between complexes **1**, **2**, and **3** arises from the difference in τ_s of Gd^{III}, then this difference should be less prominent at higher field. To examine this, r_1 values were measured on a 7 T MR scanner. Figures 4.7–8 show the relaxivity data from the 7 T relaxivity measurements and image intensities, respectively, where each complex exhibits a value of $r_1 \approx 10\ mM^{-1}s^{-1}$. These data further support the contention that the mechanism of relaxivity decrease in **1** arises from the presence of magnetic coupling to Co^{II} and not through other parameters such as τ_r or τ_m, which are all field-independent.

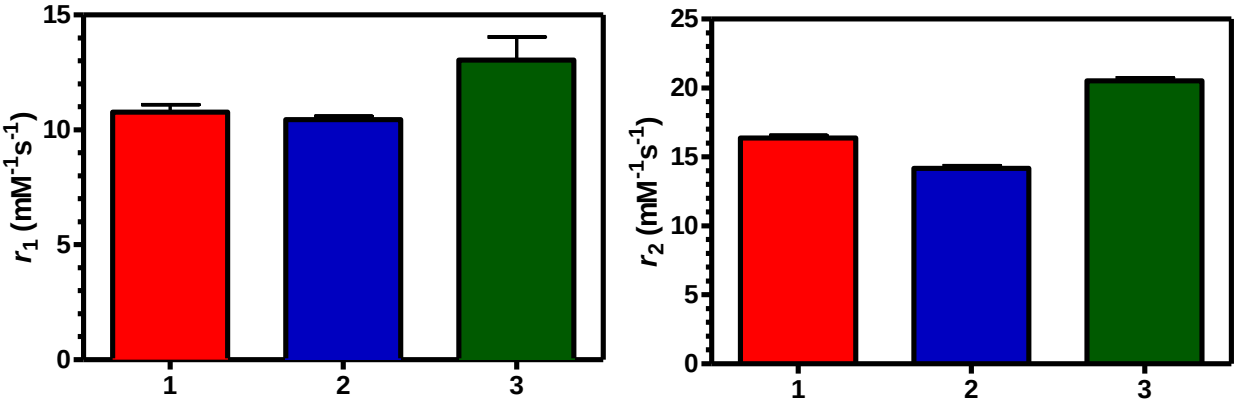

Figure 4.7 Relaxivity (r_1 left and r_2 right) measurements at 7 T of **1** (red), **2** (blue), and **3** (green). These data reflect little difference in relaxivity between each complex, unsurprising as the ^1H Larmor frequency increases as a function of field where the τ_s of Gd^{III} slows dramatically.

In order to determine whether mag-netic coupling between M^{II} and Gd^{III} leads to a decrease in τ_s of Gd^{III}, electron paramagnetic resonance (EPR) spectroscopy of each complex was measured to probe the electronic relaxation. Precise quantitation of τ_s is not possible for these complexes as the τ_s was found to be too short for the instrument acquisition timescale (ns). Nevertheless, the transverse electron relaxation time T_{2e} is expected to follow a similar trend as τ_s in the presence of magnetic coupling,[42] and therefore W-band (95 GHz) continuous-wave EPR spectra were collected for aqueous solutions of **1**–**3** at 25 °C (see Figure 4.9).

Each spectrum shows only a single feature corresponding to $S = {}^7/_2$ Gd^{III}, with g values of 1.9928, 1.9934, and 1.9922 for **1**–**3**, respectively. Importantly, **1** and **2** exhibit an increased Lorentzian linewidth of 14.3 mT and 13.5 mT, respectively, relative to that of 5.8 mT observed for **3**. For a homogenously broadened line, the full width at half-maximum (Γ) is inversely related to T_{2e} ($T_{2e} \propto \Gamma\gamma_e^{-1}$).[54] As such, the significantly larger linewidths for **1** and **2** indicate smaller T_{2e} values of Gd compared to that of **3**. In sum, while EPR measurements here cannot provide direct

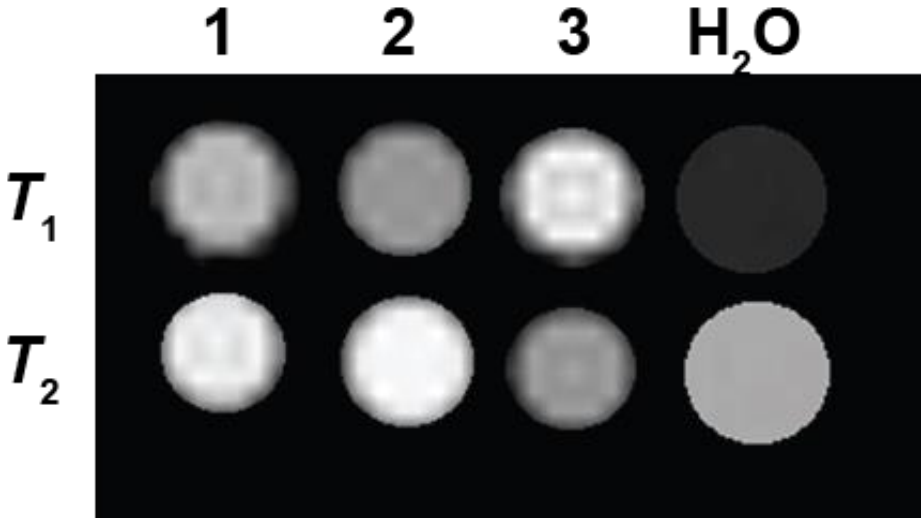

Figure 4.8 T_1 and T_2 solution phantom images of **1, 2,** and **3** at approximately 1 mM in a 7 T Bruker MR scanner. Measurements were taken at ambient temperature. No significant decrease in contrast is observed at this field as expected based on the field dependence of τ_s and the Larmor frequency of water.

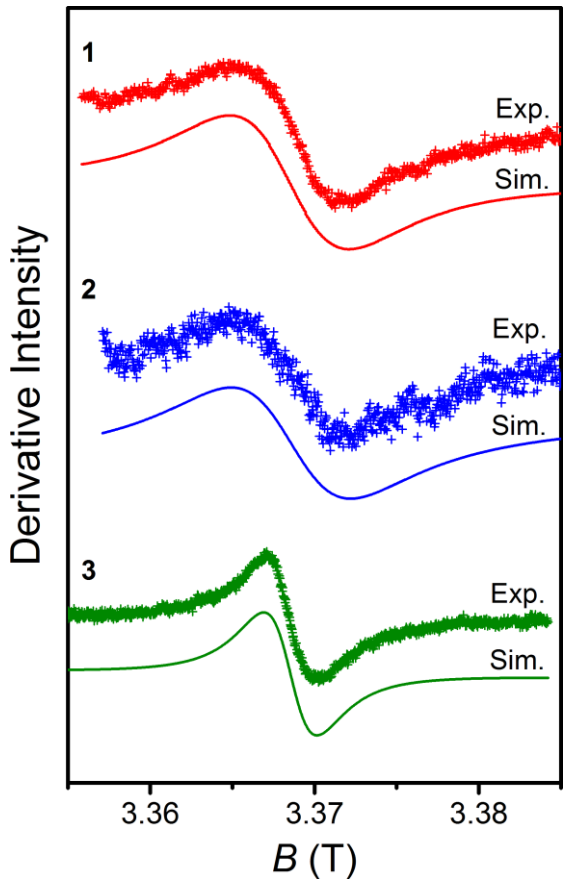

Figure 4.9 W-band EPR spectra of **1** (top, red), **2** (middle, blue) and **3** (bottom, green) in aqueous solution at room temperature. Crosses and solid lines represent experimental data and simulation, respectively.

determination of τ_s, acceleration of the electronic relaxation of Gd^{III} in **1** and **2** is evidenced by the observed reduction in T_{2e}.

To verify that the observed differences in relaxivity arise due to changes in the τ_s of Gd^{III}, nuclear magnetic relaxation dispersion (NMRD) data were obtained at 25 and 37 °C (see Figure 4.10) for **1**–**3**. This analysis enables the estimation of τ_s from fitting the parameters of the SBM model for paramagnetic relaxation enhancement, namely τ_s, τ_r, and τ_m (eq 1). The resulting NMRD profiles verify that the ^1H relaxivities decrease from **3** to **2** to **1** in the range 20–40 MHz, in accord with the value above obtained at 60 MHz. In addition, all profiles exhibit a single dispersion occurring near 10 MHz. However, the ratio between the relativities at 40 MHz and low field (< 1 MHz) differ between the complexes, indicating that both the field dependent τ_s and τ_r contribute to the dipolar relaxation correlation time (τ_c).

The temperature dependence of the profiles shows that r_1 decreases upon heating for all complexes, thus indicating that the water molecules are in fast exchange. This observation indicates that τ_m is smaller than the nuclear relaxation time of the protons on coordinated H_2O molecules, in agreement with the observed value of 60 ns at 37 °C.

Table 4.1 τ_s values at 1 T obtained from fits of the NMRD profiles, for q ranging from 5 to 6 for **1** and **3** and from 6 to 7 for **2**. The number of water molecules coordinated to Gd^{III}, q, is reported for each complex based on measurements of the Dy^{III} analogue.

	1		**2**		**3**	
T (°C)	25	37	25	37	25	37
τ_s (ns)	0.065 (±0.025)	0.065 (±0.025)	0.135 (±0.025)	0.145 (±0.025)	2.6 (±0.7)	2.5 (±0.7)
q	6.0(±0.2)		5.0(±0.2)		5.6(±0.2)	

The NMRD profiles were fit using the SBM model assuming isotropic motion for inner-sphere dipolar relaxation (see Figure 4.10), including a minor outer-sphere contribution due to freely diffusing water. This second contribution was calculated according to the Freed equation,[55] as described by the distance of closest approach d (fixed to 3.6 Å) and the diffusion coefficient D (2.5 × 10^{-9} m^2/s and 3.5 × 10^{-9} m^2/s at 25 and 37 °C, respectively). Application of the Bloembergen-Morgan equation to describe the field dependence of electron relaxation in a magnetically coupled system may be debatable. Indeed, we found this model does heuristically describes the field dependence of τ_s in **1** (Co^{II} analogue), but does not fully characterize **2** (Cu^{II} analogue). The field dependence of τ_s of Gd^{III} in **2** is parameterized by including a field independent contribution for electronic relaxation. This difference in behavior is ascribed to the fact τ_s of Co^{II} is always smaller than τ_s of Gd^{III}, whereas τ_s for Cu^{II} is longer at low field and shorter at high field than Gd^{III}. In the presence of magnetic coupling between two metal ions, as measured between Gd^{III} and Co^{II} or Cu^{II}, the SBM equation was rescaled by a constant to account for the coupling in the high-temperature limit.

In the minimization, $r_{Gd–H}$ was fixed to 3.0 Å, q was fixed to either 5 or 6, and τ_m to 100 ns and 60 ns at 25 and 37 °C, respectively. The best-fit parameters included the electronic parameters D_t (transient zero-field splitting), τ_v (correlation time for the zero-field splitting modulation), and τ_r.

Here, the values of D_t and τ_v should change depending on the identity of the transition metal, while τ_r is expected to remain essentially constant. A relatively good fit with constant τ_r is possible only if q, fixed to 5 for **1** and **3**, is increased to 6 for **2** (Figure 4.10, lower). The larger q obtained for **2** can account for the contribution to the water proton relaxation from the dipole-dipole interactions between a water molecule coordinated to the Cu^{II} center. Different from Co^{II}, this contribution may not be negligible due to the long τ_s of Cu^{II}. If in fast exchange, it can provide a contribution to the low-field relaxivity up to ~ 1 s^{-1} (corresponding to an apparent increase in q of ~ 0.2).

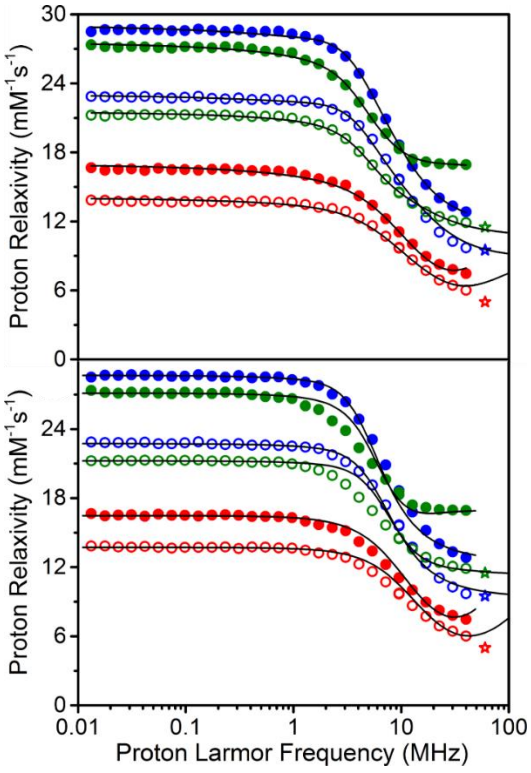

Figure 4.10 Best fit NMRD profiles obtained in the assumption of anisotropic (top) or isotropic (bottom) reorientation time. Aqueous solutions of **1** (red), **2** (blue), and **3** (green). The corresponding red, blue, and green stars represent the relaxivity measured at 1.4 T reported above. Solid and hollow spheres represent data obtained at 25 and 37 °C respectively. Lines represent the best fits obtained from the minimization.

Upon closer inspection, the best-fit profiles (see Figure 4.10, lower) are suboptimal, with dispersion occurring with a frequency dependence less steep than what is obtained from a single Lorentzian function. Moreover, the nonspherical, planar structure of the complexes suggests that the reorientation should be anisotropic, such that two rotational correlation times should be considered with a weighting factor described by the parameter S_{LS}.[25] The NMRD profiles were therefore fit using an anisotropic rotation model that accounts for two separate rotational correlation times (τ_{r1} and τ_{r2}). In this case, the NMRD fits were excellent (see Figure 4.10, upper) for q ranging between

5 and 6 for **1** and **3** and between 6 and 7 for **2**. In addition, values for $S_{LS}^2 = 0.39$, $\tau_{r1} = 150$ ps, and $\tau_{r2} = 30$ ps were obtained at 25 °C. Most importantly, the fits reveal that τ_s at high fields is much shorter in the complexes with magnetic exchange coupling. For instance, at 25 °C and 1 T, values of $\tau_s = 0.065 \pm 0.025$ and 0.135 ± 0.025 ns were obtained for **1** and **2**, respectively, considerably shorter than that of $\tau_s = 2.6(07)$ ns for **3**.

4.4 Conclusion and Outlook

The foregoing results demonstrate that magnetic exchange coupling between Gd^{III} and transition metal ions provides a route toward low-background MR imaging contrast agents. This approach is exemplified by a study of the complexes $LMLn(\mu\text{-}O_2CCH_3)(O_2CCH_3)_2$ (M = Co, Cu, Zn). Solid-state magnetic susceptibility measurements reveal the presence magnetic coupling between Gd^{III} and the paramagnetic transition metal ions, with $J = +0.22$ cm^{-1} for the $LCoGd(\mu\text{-}O_2CCH_3)(O_2CCH_3)_2$ (**1**) complex and $J = +2.6$ cm^{-1} for the $LCuGd(\mu\text{-}O_2CCH_3)(O_2CCH_3)_2$ (**2**) complex. The three complexes are shown by ^1H and ^{17}O NMR spectroscopy to be $[LCoGd(H_2O)_6]^{3+}$, $[LCoGd(H_2O)_5]^{3+}$, and $[LCoGd(H_2O)_{5.6}]^{3+}$ in aqueous solution.

Further, NMR experiments demonstrate that relaxivity values are lower by half for $LCoGd(\mu\text{-}O_2CCH_3)(O_2CCH_3)_2$ in comparison to $LZnGd(\mu\text{-}O_2CCH_3)(O_2CCH_3)_2$ by virtue of the short τ_s of Co^{II}. Finally, NMRD analysis confirms that these differences in relaxivity are associated with differences in modulation of τ_s of Gd^{III}, with fits to the profiles giving values of $\tau_s = 0.065 \pm 0.025$, 0.135 ± 0.025, and 2.6 ± 0.7 ns for $LCoGd(\mu\text{-}O_2CCH_3)(O_2CCH_3)_2$, $LCuGd(\mu\text{-}O_2CCH_3)(O_2CCH_3)_2$, and $LZnGd(\mu\text{-}O_2CCH_3)(O_2CCH_3)_2$, respectively. These dinuclear complexes provide the proof-of-concept to develop biologically applicable complexes.

Future work will focus on alternative pathways to generate near zero-background probes through incorporation pathways for both better donor ligands and stronger magnetic coupling. Finally, we are using the critical lessons learned from this work to synthesize bioresponsive agents that are redox-sensitive where the τ_s can be modulated via biochemical redox events. This can be conceived as starting from a zero-background, magnetically coupled (fast τ_s) state being oxidized/reduced to break the coupling and restore the τ_s of Gd^{III} thus, subsequently increasing the relaxivity.

Chapter Five: Selective Binding and Quantitation of Calcium with a Cobalt-Based Magnetic Resonance Probe

Du, K. and Harris, T. D. *Submitted*

This work was performed in collaboration with the co-authors listed above.

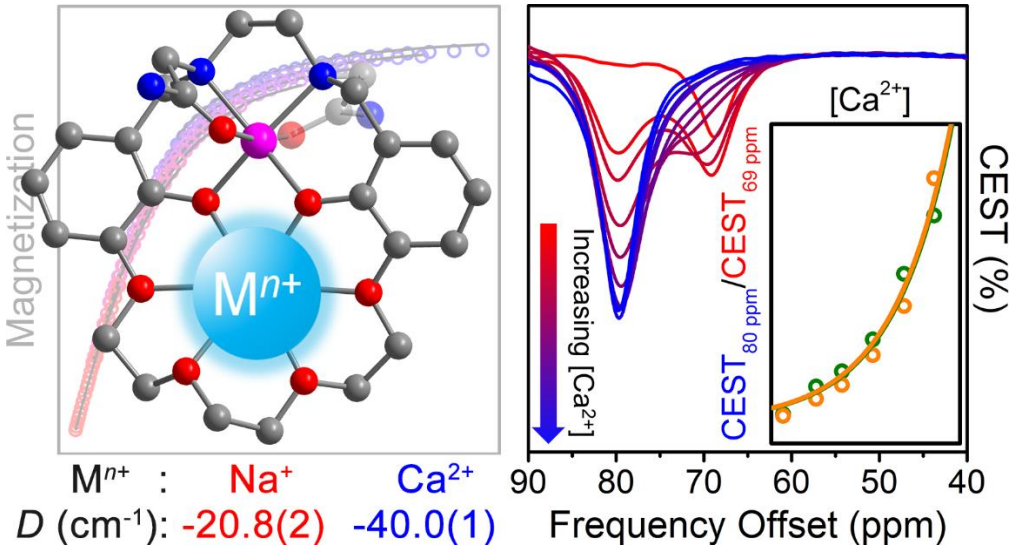

5.1 Introduction

The concentration of Ca^{2+} in serum is a vital biomarker for bone-related diseases such as cancer,[1] hyperparathyroidism,[2] and Paget's disease.[3] These diseases are associated with the dissolution of bone tissue, which releases Ca^{2+} into the blood stream and results in hypercalcemia, a medical condition where the total Ca^{2+} concentration in serum exceeds 2.6 mM[4] In current clinical settings, the presence and extent of hypercalcemia is evaluated by blood tests. This form of analysis provides only an average estimate of the total Ca^{2+} concentration in serum, with no information on the spatial distribution or local concentration of Ca^{2+} near the bone lesion. As such, while blood tests can conveniently confirm the presence of hypercalcemia, they do not enable an assessment of the underlying source and cause of high Ca^{2+} concentrations.[5] For these reasons, realization of an imaging technique able to quantitate the local Ca^{2+} concentration near bone tissue would be highly useful in the early detection of bone-related diseases and in pathological studies.

Magnetic resonance imaging (MRI) is a non-invasive technique that is particularly well-suited for measuring the concentration of Ca^{2+} near bone tissue, owing to its unlimited depth penetration of tissue and its ability to provide spatiotemporal images.[6] Toward this end, several Gd^{III}-based probes have been developed to detect Ca^{2+} ions, by virtue of relaxivity changes upon binding Ca^{2+}.[7] Here, extensive synthetic modifications have been employed to impart selective binding of Ca^{2+} in the presence of other cations.**Error! Bookmark not defined.**[7] Nevertheless, the utility of these probes is limited by heterogeneous biodistribution of Ca^{2+} or of the probes themselves. It is therefore critical to develop MRI probes capable of selectively binding and quantitating Ca^{2+} through a concentration-independent method.

Lanthanide-[8] and transition metal-based[9] paramagnetic chemical exchange saturation transfer (PARACEST) probes, which deliver magnetization to bulk H_2O through chemical exchange of protons, have been reported to detect a number of biomarkers, such as redox environment,[10] pH,[11] temperature[12] and Zn^{2+} ions.[13] The frequency-specific contrast afforded by PARACEST enables simultaneous detection of more than one CEST peak. As a result, a probe wherein the intensity ratio of two distinct CEST peaks that exhibit different responses can provide an effective and concentration-independent measure of biomarkers.[10c, 11g, h]

An ideal Ca^{2+}-responsive PARACEST probe should feature a recognition moiety that is modestly selective for Ca^{2+}, yet can reversibly bind other cations of concentrations that are relatively constant in serum, in order to allow ratiometric measurement. One such cation is Na^+, which features a concentration of ca. 140 mM in serum.[14] In addition, the frequencies of CEST peaks, corresponding to chemical shifts of labile protons, for Na^+- and Ca^{2+}-bound probes should be well-separated to avoid interference, analogous to the attributes of a ^{19}F probe.[15] Indeed, it has been shown that alkali and alkaline earth cations can significantly influence the magnetic anisotropy of a nearby paramagnetic metal ion, by causing distortions in the local coordination environment.[16] Because proton hyperfine shift is highly sensitive to changes in coordination environment and magnetic anisotropy, CEST peaks with unique chemical shifts can be indicative of the identity of the bound cation.[17] Herein, we present a Co^{II}-based PARACEST probe that can reversibly bind Ca^{2+} and Na^+. The ratio of CEST signal intensities from the resulting Ca^{2+}- and Na^+-bound probes enables, for the first time, the concentration-independent quantitation of Ca^{2+} by MR.

5.2 Experimental Section

General considerations. Unless otherwise specified, chemicals and solvents were purchased from commercial vendors and used without further purification. Deuterated solvents were purchased from Cambridge Isotope Laboratories. When necessary for moisture sensitive experiments, glassware was flame dried or stored in an oven at 150 °C for at least 4 hours, followed by cooling in a desiccator. Air- and water-free manipulations were carried out using standard Schlenk techniques. Acetonitrile was dried using a commercial solvent purification system from Pure Process Technology and stored over 4 Å molecular sieves prior to use. Water was obtained from a purification system from EMD Millipore.

Synthesis of 1,8-ditosyl-3,6-dioxaoctane.[18] Triethylene glycol (20 g, 0.13 mol) and p-toluenesulfonyl chloride (51 g, 0.27 mol) were dissolved in 150 mL of DCM. The resulting colorless solution was cooled by an ice/H_2O bath. To this solution KOH (60 g, 1.1 mol) was added in small portions with vigorous stirring. After 12 hours of stirring, cold H_2O (300 mL) was added and the DCM layer was collected. The aqueous layer was then extracted by DCM (150 mL × 3). The combined DCM solution was washed by H_2O (50 mL × 2) and dried by $MgSO_4$. Evaporation of the solvent resulted in a white solid (55 g, 90%). ^{1}H NMR ($CDCl_3$): 7.79 (d, 4H), 7.34 (d, 4H), 4.14 (t, 4H), 3.65 (t, 4H), 3.52 (s, 4H), 2.44 (s, 6H).

Synthesis of 3,3'-(3,6-dioxaoctane-1,8-diyldioxy)bis(2-hydroxybenzaldehyde).[19] Under a dry dinitrogen atmosphere, 2,3-dihydroxybenzaldehyde (7.0 g, 0.050 mol) was dissolved in anhydrous DMSO (30 mL). The resulting dark yellow solution was slowly transferred via a cannula (ca. 1 drop per second), to a suspension of NaH (2.6 g, 0.11 mol) in anhydrous DMSO (30 mL), which was cooled by an ice/H_2O bath. After the addition was complete, the dark brown mixture was stirred for 1 hour at room temperature. Under a dry dinitrogen atmosphere, 1,8-

ditosyl-3,6-dioxaoctane (11 g, 0.025 mol) was added, and the dark brown mixture was stirred for 20 hours at room temperature. The resulting dark brown solution was added to H_2O (400 mL), and was washed by $CHCl_3$ (200 mL × 2). The pH of the aqueous layer was adjusted to 1 by addition of 6 M HCl in H_2O. The brown slurry was then extracted by $CHCl_3$ (100 mL × 3). The combined organic layers were washed by 1 M HCl in H_2O (200 mL × 5). After dried by $MgSO_4$, the brown solution was evaporated to dryness. The resulting brown oil was purified by a silica column. DCM was passed through the column until no byproduct was present in the eluent. Then 2% MeOH in DCM was used to elute the desired product (R_f = 0.35 in 2% MeOH/DCM). Evaporation of the yellow solution resulted in a yellow solid (4.5 g, 46%). ^{1}H NMR ($CDCl_3$): 10.87 (s, 2H), 9.95 (s, 2H), 7.23 (d, 2H), 7.19 (d, 2H), 6.94 (t, 2H), 4.24 (t, 4H), 3.92 (t, 4H), 3.79 (s, 4H).

Synthesis of (9,10,12,13,15,16,18,19,21,22-decahydro-3,7:24,28-dimetheno-8,11,14,17,20,23,1,30-benzohexaoxadiazacyclodotriacontine-35,36-diol-*O*^{8},*O*^{11},*O*^{14},*O*^{17},*O*^{20},*O*^{23},*O*^{35},*O*^{36})barium(2+) diperchlorate.[2] $Ba(ClO_4)_2$ (1.7 g, 5.1 mmol) was dissolved in MeOH (80 mL) and heated at reflux. To the colorless solution, 3'-(3,6-dioxaoctane-1,8-diyldioxy)bis(2-hydroxybenzaldehyde) (2.0 g, 5.1 mmol) dissolved in MeOH (20 mL) was added to give a yellow solution. After 15 minutes of heating, ethylenediamine (0.31 g, 5.1 mmol) dissolved in MeOH (100 mL) was added dropwise to the yellow solution over the course of 4 hours. The yellow solution was heated at reflux for another 2 hours. After cooled to room temperature, the yellow solution was filtered by filter paper and the solvent was slowly evaporated to give a yellow crystalline solid, which was collected by filtration (2.3 g, 59%). ^{1}H NMR (DMSO-d_6): 15.12 (s, 2H), 8.78 (d, 2H), 7.05 (d, 2H), 6.65 (t, 2H), 4.15 (d, 4H), 3.97 (s, 4H), 3.86 (d, 4H), 3.72 (s, 4H).

Synthesis of 9,10,12,13,15,16,18,19,21,22-decahydro-3,7:24,28-dimetheno-8,11,14,17,20,23,1,30-benzohexaoxadiazacyclodotriacontine-35,36-diol.[2] (9,10,12,13,15,16,18,19,21,22-decahydro-3,7:24,28-dimetheno-8,11,14,17,20,23,1,30-benzohexaoxadiazacyclodotriacontine-35,36-diol-O^8,O^{11},O^{14},O^{17},O^{20},O^{23},O^{35},O^{36})barium(2+) diperchlorate (1.3 g, 1.7 mmol) was suspended in DCM (50 mL). To the white slurry, guanidinium sulfate (1.8g, 17 mmol) in H_2O (50 mL) was added. The mixture was stirred vigorously for 1 hour. The DCM layer was collected and dried by $MgSO_4$. Evaporation of the solvent and subsequent drying in vacuo resulted in a yellow solid (0.61 g, 89%). ^{1}H NMR (DMSO-d_6): 14.08 (s, 2H), 8.65 (s, 2H), 6.99 (m, 2H), 6.73 (t, 2H), 4.06 (m, 4H), 3.87 (s, 4H), 3.69 (m, 4H), 3.60 (s, 4H).

Synthesis of 9,12,15,18-tetraoxa-3,6-diaza-1,8(1,3)-dibenzenacyclooctadecaphane-12,82-diol. 9,10,12,13,15,16,18,19,21,22-decahydro-3,7:24,28-dimetheno-8,11,14,17,20,23,1,30-benzohexaoxadiazacyclodotriacontine-35,36-diol (0.61g, 1.5 mmol) was dissolved by DCM (20 mL) and the yellow solution was stirred in an ice bath. MeOH (50 mL) was added to the yellow solution (More DCM can be added if there are precipitate). Tetramethylammonium borohydride (0.26 g, 3.0 mmol) was added to the yellow solution in small portions. Small amount of bubbles formed and the solution became a pale slurry. The mixture was stirred in the ice bath for 1 hour, and then at room temperature for 20 minutes. The pH (as indicated by pH paper) of the off-white mixture was adjusted to 1 by addition of HCl (5 M). The mixture was then evaporated to dryness to give a colorless oil. The oil was dissolved by H_2O (50 mL) and the pH of the solution was adjusted to 8 by tetramethylammonium hydroxide solution (1 M). The slurry was extracted by DCM (50 mL × 3). The combined organic layers were dried by $MgSO_4$ and evaporated to dryness. After drying in vacuo, an off-white solid was obtained (0.44 g, 71%). ^{1}H NMR ($CDCl_3$): 6.70-6.72

(m, 2H), 6.66-6.67 (m, 4H), 4.10 (m, 4H), 3.87 (s, 4H), 3.85 (m, 4H), 3.74 (s, 4H), 2.90 (s, 4H).

Synthesis of 2,2'-(12,82-dihydroxy-9,12,15,18-tetraoxa-3,6-diaza-1,8(1,3)-dibenzenacyclooctadecaphane-3,6-diyl)diacetamide (H_2L). Under a dry dinitrogen atmosphere, 9,12,15,18-tetraoxa-3,6-diaza-1,8(1,3)-dibenzenacyclooctadecaphane-12,82-diol (0.20 g, 0.48 mmol) and diisopropylethylamine (0.12 g, 0.96 mmol) were dissolved by MeCN (20 mL). The brown solution was heated at reflux. To the boiling solution, 2-bromo-acetamide (0.13 g, 0.96 mmol) was added dropwise with vigorous stirring. After 12 hours of heating, basic alumina (2 g) was added and the mixture was evaporated to dryness. The powder was dry-loaded on a basic alumina column, which was packed by 100% DCM. After loading, the column was first eluted by 2% MeOH/DCM until no substance detected on TLC (visualized by I_2 vapor) to remove an impurity (R_f ~ 0.6 in 5% MeOH/DCM). The column was then eluted by 5% MeOH/DCM to obtain the desired product (R_f ~ 0.3 in 5% MeOH/DCM). The combined fractions were evaporated to dryness to give an off-white solid (25 mg, 10%). ^{1}H NMR (MeOH-d_4): 6.88 (t, 2H), 6.72 (m, 4H), 4.14 (m, 4H), 3.88 (m, 4H), 3.77 (s, 4H), 3.65 (s, 4H), 3.03 (s, 4H), 2.72 (s, 4H).

Synthesis of $LCo\cdot 3.1H_2O$ (1). Under a dinitrogen atmosphere, H_2L (25 mg, 4.7 mmol) was dissolved by MeOH (5 mL). $Co(OAc)_2\cdot 4H_2O$ dissolved in MeOH (5 mL) was added to the stirring colorless solution. The resulting light magenta solution was heated at reflux under a dinitrogen atmosphere for 12 hours. The solution was evaporated to dryness and the residue was dissolved by MeOH (2 mL). The pink solution was added to Et_2O (15 mL) with vigorous stirring, to induce a pink precipitate. The pink solid was collected by filtration, washed by Et_2O (5 mL) and dried in vacuo (25 mg, 90%). Anal. Calcd. for $C_{26}H_{40.2}N_4O_{11.1}Co$: C, 48.4; H, 6.28; N, 8.68. Found: C, 48.2; H, 5.62; N, 9.14. UV/Visible absorption spectrum: 517 nm (ε = 59.5 $M^{-1}\,cm^{-1}$), 526 nm (ε =

57.7 M^{-1} cm^{-1}). FT-IR (ATR, cm^{-1}): 3341 (s, broad); 2916 (m); 2872 (m); 1662 (s); 1589 (s); 1562 (s); 1456 (s); 1304 (m); 1229 (s); 1110 (s); 1070 (s); 987 (m); 955 (m); 932 (m); 894 (m); 840 (m); 737 (s); 587 (w); 439 (w); 407 (w). Solution magnetic moment $\chi_M T$ = 2.4(3) cm^3K/mol (310 K). Slow diffusion of acetone into the pink solution of **1** in H_2O over two weeks yield single crystals of $LCo{\cdot}0.50C_3H_6O{\cdot}0.55H_2O$ (**1′**) suitable for X-ray structural analysis.

Synthesis of $LCoNaNO_3{\cdot}1.7H_2O$ (2). **1** (30 mg, 51 μmol) was dissolved in MeOH (5 mL). To the stirring pink solution, $NaNO_3$ (4.3 mg, 51 μmol) in MeOH (0.5 mL) was added. The pink solution was stirred for 5 minutes and filtered by a celite column. Slow diffusion of E_2O into the pink solution over 3 days resulted in pink crystalline solid, which was collected by filtration (34 mg, 94%). Anal. Calc. for $C_{26}H_{37.3}N_5O_{12.7}CoNa$: C, 44.3; H, 5.34; N, 9.94. Found: C, 44.3; H, 5.16; N, 10.1. FT-IR (ATR, cm^{-1}): 3356 (s, broad); 2921 (m); 2873 (m); 1666 (s); 1591 (m); 1564 (m); 1476 (s); 1458 (s); 1302 (m); 1270 (m); 1231 (s); 1107 (s); 1086 (s); 987 (m); 956 (m); 930 (m); 896 (m); 840 (m); 741 (s); 409 (m). Slow diffusion of acetone into the pink solution of **1** in H_2O over two weeks yield single crystals of $[LCoNa(H_2O)](NO_3)$ (**2′**) suitable for X-ray structural analysis

Synthesis of $LCoCa(NO_3)_2{\cdot}0.25Et_2O{\bullet}0.50H_2O$ (3). **1** (30 mg, 51 μmol) was dissolved in MeOH (5 mL). To the stirring pink solution, $Ca(NO_3)_2{\cdot}4H_2O$ (12 mg, 51 μmol) in H_2O (0.5 mL) was added. The pink solution was stirred for 5 minutes and filtered by a celite column. Slow diffusion of E_2O into the pink solution over 4 days resulted in pink crystalline solid, which was collected by filtration (36 mg, 90%). Anal. Calc. for $C_{27.0}H_{37.5}N_6O_{14.7}CaCo$: C, 41.5; H, 4.84; N, 10.8. Found: C, 41.5; H, 5.03; N, 10.9. FT-IR (ATR, cm^{-1}): 3341 (s, broad); 2922 (m); 2874 (m); 1662 (s); 1600 (m); 1566 (m); 1475 (s); 1325 (s); 1303 (m); 1233 (s); 1105 (s); 1086 (s); 1071 (s);

1022 (m); 983 (m); 958 (m); 942 (m); 843 (m); 828 (m); 738 (s); 444 (w); 431 (m). Slow diffusion of Et_2O into the pink solution of **3** in MeOH over two weeks yield single crystals of $[LCoCa(NO_3)(MeOH)](NO_3)\cdot MeOH$ (**3′**) suitable for X-ray structural analysis

X-ray structure determination. Single crystals of **1′**, **2′** and **3′** were directly coated with Paratone-N oil and mounted on a MicroMounts™ rod. The crystallographic data were collected at 100 K on a Bruker APEX II diffractometer equipped with MoKα sealed tube source. Raw data were integrated and corrected for Lorentz and polarization effects using Bruker APEX2 v. 2009.1.[20] The program SADABS was used to apply absorption correction.[21] Space group assignments were determined by examining systematic absences, E-statistics and successive refinement of the structure. Structures were solved by SHELXT[22] using direct methods and refined by SHELXL within the OLEX interface.[23] Solvent mask was applied to the structures for **1′**, **2′** to account for severely disordered solvent molecules that cannot be properly modeled.

Solid-state Magnetic measurements. Magnetic measurements of **1**, **2** and **3** were performed on polycrystalline samples dispensed in icosane loaded in quartz tubes under a dinitrogen atmosphere. The samples were attached to a sealable hose-adapter and flame sealed under vacuum on a Schlenk manifold. All data were collected using a Quantum Design MPMS-XL SQUID magnetometer at 1.8 K. The reduced magnetization data were collected at applied dc fields ranging from 0 to +7 T. Ac susceptibility data were collected under a dc field of 1000 Oe and an ac field of 4 Oe, oscillating at frequencies in the range of 1–1500 Hz. The reduced magnetization data were fitted using *PHI*[24] with isotropic *g* values, 2.30(1), 2.28(1) and 2.33(1) for **1**, **2** and **3**, respectively, to get zero-field splitting parameters (*D*). Ac susceptibility plots were fitted using a generalized Debye model[25] at 1.8 K to estimate relaxation times (τ).

Solution magnetic measurements. The magnetic moments of **1** was carried out using Evan's method[26] at 310 K. Typical samples contained 5 mM of **1** in a mixture of 0.5 w/w % of DMSO in D_2O. A capillary containing same solvent mixture (without **1**) was inserted into each NMR sample as reference. Diamagnetic correction was carried out based on the empirical formula of **1** using Pascal's constants.[27]

NMR and CEST experiments. NMR and CEST experiments were performed on an Agilent DD2 500 MHz (11.75 T) system. All chemical shifts were referenced to the H_2O resonance (0 ppm). Unless otherwise noted in the text, typical samples contained 5 mM of **1**, 50 mM of HEPES buffered at pH 7.4. Samples were prepared and stored under dinitrogen atmosphere to ensure no degradation due to oxidation by air. Note that the pH of buffer was adjusted using HCl and NMe_4OH to avoid introduction of inorganic cations. Z-spectra (CEST spectra) were obtained according to the following protocol. NMR spectra were acquired using the presaturation pulse applied for 3 s at a power level of 21 μT. The B_1 values are calculated based on the calibrated 90-degree pulse on a linear amplifier. The saturaton frequency offsets were screened ranging from –100 to 100 ppm with a step increase of 1 ppm. The obtained NMR spectra were plotted as normalized water intensity against frequency offset (chemical shifts with respect to H_2O) to produce a Z-spectrum. Direct saturation of the water signal was set to 0 ppm. CEST intensities from 20 to 40 ppm were fitted by a linear model to construct baselines, based on which the relevant CEST intensities were corrected. D_2O was placed in an inner capillary to lock the sample. Exchange rate constants were calculated based off a reported method.[28] The NMR spectra were acquired at various presaturation powers ranging from 7.4 to 21 μT applied for 6 s.

NMR titrations for Na^+ or Ca^{2+} binding affinities. To determine the affinity for Na^+, samples

containing 5 mM of **1**, 50 mM of HEPES buffered at pH 7.3, 7.4 and 7.5 in H_2O were added with various amount of $NaNO_3$ to give final concentrations of Na^+ ranging from 0 to 20 mM. The conversion rate for LCo + Na^+ $\rightleftharpoons$ $[LCoNa]^+$ was fast caompared to NMR acquisition time scale (~ms), as evidenced by the presence of only one set of NMR peaks for the whole series of spectra. The most dramatic change in shift, with relatively narrow peak width, occurs on a resonance located at ~128 ppm (LCo), which shifted to ~130 ppm upon binding Na^+ ($[LCoNa]^+$). Such change in chemical shifts was monitored and fitted using Dynafit[29] to get K_d, using following scripts. Reported values of K_d were averaged from three experiments.

To determine the affinity for Ca^{2+}, samples containing 2 mM of **1** and 150 mM of $NaNO_3$ in D_2O were added with various amount of $Ca(NO_3)_2$ to give final concentrations of Ca^{2+} ranging from 0 to 4 mM. Because the K_d for Ca^{2+} was expected to be lower than Na^+, 150 mM of Na^+ was introduced to compete with Ca^{2+}, so an equilibrium can be established at a concentration of **1**, high enough to be observed by NMR. The conversion rate for $[LCoNa]^+ + Ca^{2+}$ $\rightleftharpoons$ $[LCoCa]^{2+} + Na^+$ was observed to be slow compare to the NMR acquisition time scale, as evidenced by the presences of two sets of NMR peaks for the series of spectra (see Figure 5.4). Because the integrations of respective peaks needed to be measured with high accuracy, D_2O were used as solvent to increase signal-to-noise ratio. The ratios of integrations at 250 and 216 ppm, 71 and 52 ppm were used to get the normalized percentage of $[LCoCa]^{2+}$. Attempts to fit the data using a competition model was not successful, likely due to a low K_d for Ca^{2+}.

Electrochemical measurements. Cyclic voltammetry was carried out in a standard one-compartment cell inside a nitrogen glove box at room temperature, equipped with a glassy carbon working electrode, a platinum wire as counter electrode and a SCE reference electrode using a

CHI 760c potentiostat. The analyte solution was prepared with 100 mM NMe_4Cl and 50 mM HEPES buffered at pH 7.4. The voltammogram was converted and shown as values referred to the normal hydrogen electrode (NHE), using a literature conversion factor.[30]

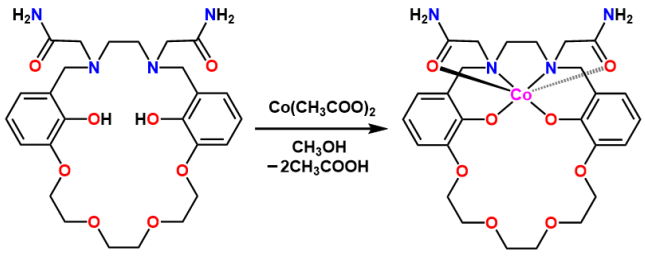

Figure 5.1 Synthesis and chemical structure of LCo.

Other physical measurements. Infrared spectra were recorded on a Bruker Alpha FTIR spectrometer equipped with an attenuated total reflectance accessory. Solution UV-Vis-NIR spectra were obtained using an Agilent Cary 5000 spectrophotometer. Elemental analyses of **1**, **2** and **3** were performed by Midwest Microlab (Indianapolis, IN).

5.3 Results and Discussion

Reaction of H_2L[16a, 31] with $Co(CH_3COO)_2{\cdot}4H_2O$ afforded the pink compound $LCo{\cdot}3.1H_2O$ (**1**) in 90% yield (see Figure 5.1). Subsequent addition of stoichiometric $NaNO_3$ or $Ca(NO_3)_2{\cdot}4H_2O$ yielded the compounds $LCoNa(NO_3){\cdot}1.7H_2O$ (**2**) or $LCoCa(NO_3)_2{\cdot}0.25Et_2O{\cdot}0.50H_2O$ (**3**), respectively. Slow diffusion of acetone into aqueous solutions of **1** or **2**, or Et_2O into a solution of **3** in CH_3OH, gave pink block-shaped crystals of $LCo{\cdot}0.50C_3H_6O{\cdot}0.55H_2O$ (**1′**), $[LCoNa(H_2O)](NO_3)$ (**2′**) and $[LCoCa(NO_3)(CH_3OH)](NO_3){\cdot}CH_3OH$ (**3′**), respectively, suitable for single-crystal X-ray diffraction analysis.

In all three structures, the Co^{II} ion resides in distorted octahedral environments, with the N_2O_2 pocket of L^{2-} comprising the equatorial plane and the O atoms from the carboxamide groups coordinating the axial sites (see Figure 5.2, upper). In **2′**, a Na^+ ion is ligated by four of six O atoms from the crown ether unit of L^{2-} and an aqua ligand to give an irregular five-coordinate complex. In contrast, **3′** features a Ca^{2+} ion that induces minimal distortion of the crown ether, with all six $Na–O_{crown}$ distances shorter than 2.74 Å. Because Ca^{2+} and Na^+ have similar ionic radii,[32] the less distorted structure in **3′** likely stems from the increase in electrostatic attraction between Ca^{2+} and O. The nine-coordinate Ca^{2+} ion is additionally ligated by a MeOH molecule and an η^2-NO_3^- ion.

The conformational differences in the crown ether units in **1′**, **2′**, and **3′** cause significant structural differences at Co between the compounds. This effect can be quantified by examination

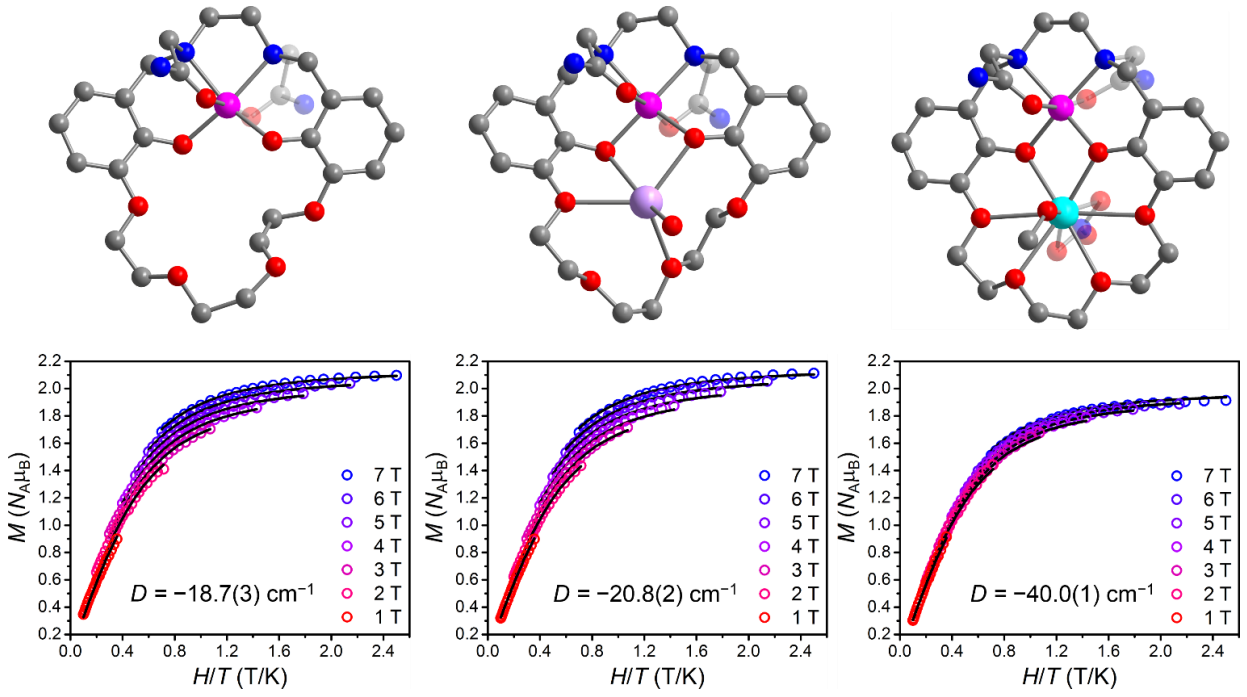

Figure 5.2 Upper: crystal structures of LCo (left), $[LCoNa(H_2O)]^+$ (middle) and $[LCoCa(CH_3OH)(NO_3)]^+$ (right), as observed in **1′**, **2′** and **3′**, respectively. Magenta, cyan, lilac, red, blue and gray spheres represent Co, Ca, Na, O, N, and C atoms, respectively; H atoms are omitted for clarity. Lower: low-temperature magnetization data for **1** (left), **2** (middle) and **3** (right), collected at selected fields. Circles and black solid lines represent experimental data and corresponding fits, respectively.

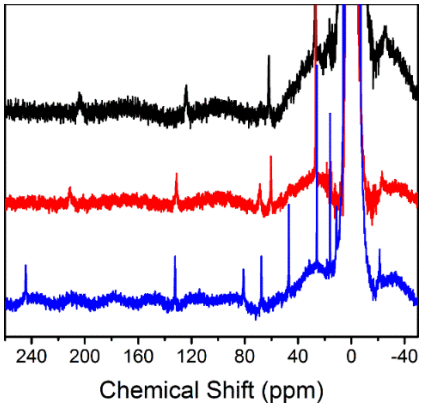

Figure 5.3 Stacked NMR spectra for solutions containing 5 mM of **1** and 50 mM of HEPES buffered at pH7.4 without any inorganic cations (black); in the presence of 15 mM of $NaNO_3$ (red) or $Ca(NO_3)_2$ (blue).

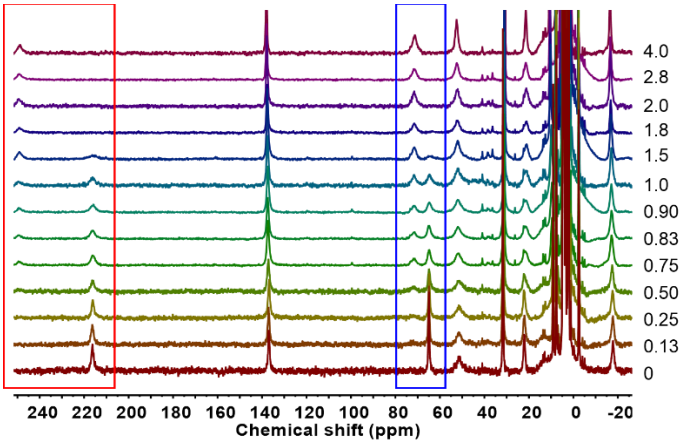

Figure 5.4 Stacked NMR spectra of solutions containing 2 mM of **1** and 150 mM of NaCl in D_2O with various concentrations of $Ca(NO_3)_2$, ranging from 0 to 4 mM. Legend: the concentration of Ca^{2+} in mM.

of the octahedral distortion parameter (Σ), which is calculated as the sum of the absolute deviations from 90° for all *cis* L-Co-L angles.[33] Across the series, **1′** features the largest distortion from an octahedral geometry at Co, with Σ = 97.8(5)°, followed by **2′** with Σ = 91.6(4)°, and **3′** with Σ = 66.3(2)° (see Table 5.1).

Given the significant differences in coordination geometry at Co across the three compounds, one would expect associated differences in magnetic anisotropy. To probe this possibility, low-temperature magnetization data were collected for **1**, **2**, and **3** at selected dc fields (see Figure 5.2, lower). The nonsuperimposability of the resulting isofield curves for all compounds, along with their saturation below the expected $M = 3\ \mu_B$ for an $S = {}^3/_2$ Co^{II} center, indicates the presence of significant zero-field splitting. Fits to the data quantify this effect,[24] giving axial zero-field splitting values of D = −18.7(3), −20.8(2),

Table 5.1 Selected mean interatomic distances and octahedral distortion parameter (Σ) for **1′**–**3′**; axial zero-field splitting parameter (D) for **1**–**3**.

	1′ / 1	**2′ / 2**	**3′ / 3**
Co−O_{amide} (Å)	2.158(4)	2.15(3)	2.12(3)
Co−$O_{phenoxo}$ (Å)	2.00(2)	2.009(8)	1.978(1)
Co−N (Å)	2.22(3)	2.18(3)	2.141(5)
Σ (°)	97.8(5)	91.6(4)	66.3(2)
D (cm^{-1})	−18.7(3)	−20.8(2)	−40.0(1)

and −40.0(1) cm^{-1} for **1**, **2**, and **3**, respectively. Here, the magnitude of D increases with decreasing distortion from octahedral geometry at Co, in line with a progression toward orbital degeneracy in moving from **1** to **3**.

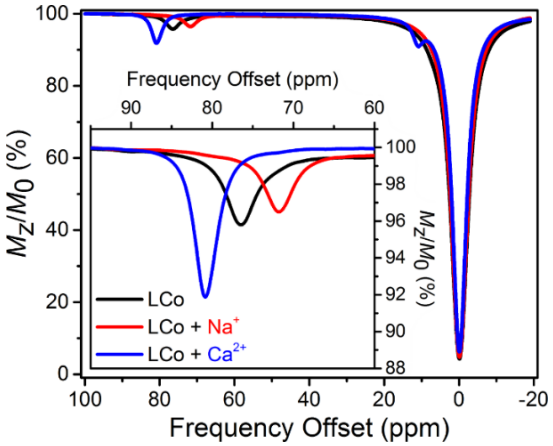

Figure 5.5 CEST spectra of 5 mM **1** at pH 7.4 (black), and with 15 mM of Na^+ (red) or Ca^{2+} (blue). Inset: expanded view of relevant CEST peaks.

Since the hyperfine shifts of ^{1}H NMR spectra are dependent on D and the local coordination environment of Co,[17] one would expect significant differences in the spectra for **1**–**3**. To probe this possibility, spectra were collected at 37 °C for solutions containing 5 mM **1** and 50 mM HEPES, buffered at pH 7.4, with and without 15 mM $NaNO_3$ or $Ca(NO_3)_2{\cdot}4H_2O$ (see Figure 5.3). Note that excess salt was used to ensure complete cation binding, and no further spectral changes were observed beyond this concentration. Spectra for all three solutions display sharp peaks spanning −40 to 240 ppm vs H_2O, consistent with high-spin Co^{II}. For the solutions of **1**, **1** + Na^+, and **1** + Ca^{2+}, a single carboxamide resonance was observed at 77, 69, and 80 ppm, respectively, suggesting chemical equivalence of the two functional groups in each molecule. The difference in chemical shift of 11 ppm between the three solutions, more than two orders of magnitude greater than that of a diamagnetic analogue,[16a] highlights the sensitivity of chemical shift toward structural and magnetic differences at Co. The dissociation constants for **1** + Na^+ at pH 7.3, 7.4, and 7.5, were measured as K_d = 3.7(9), 1.8(9) and 2(1) mM, respectively, indicating minimal effects of pH on Na^+ binding. The value of K_d for the calcium adduct was too small to be measured using NMR (see Figure 5.4).

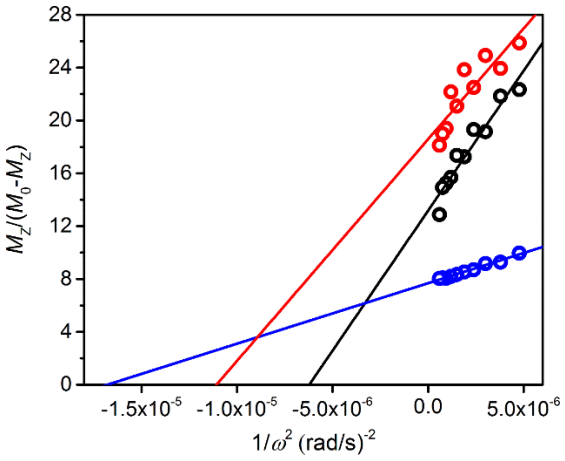

Figure 5.6 Omega plots for samples containing 5 mM of **1** and 50 mM of HEPES buffered at pH 7.4 without any inorganic cations (black); in the presence of 15 mM of $NaNO_3$ (red) or $Ca(NO_3)_2$ (blue).

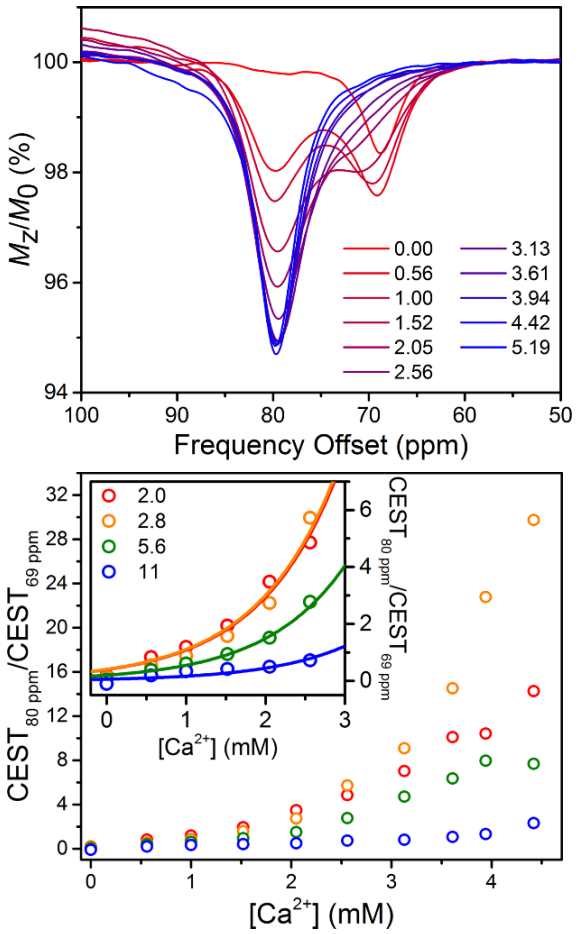

Figure 5.7 Upper: CEST spectra of solutions containing 2 mM **1** and 150 mM NaCl at pH 7.4 with increasing concentration of Ca^{2+}. The legend denotes [Ca^{2+}] (mM). Lower: ratio of CEST peak intensities from presaturation at 80 and 69 ppm vs [Ca^{2+}]. Inset: expanded view of the relevant data. Circles and solid lines represent experimental data and fits, respectively. The legend denotes [**1**] (mM).

CEST spectra for solutions containing 5 mM **1** and 50 mM HEPES, buffered at pH 7.4, with and without 15 mM Na^+ and Ca^{2+}, were collected at 37 °C. For solutions of **1**, **1** + Na^+, and **1** + Ca^{2+}, CEST peaks were observed at 77, 69, and 80 ppm, respectively, with 4.8, 3.9, and 8.5% H_2O signal reduction (see Figure 5.5). Despite these low intensities, the separation in frequency of the CEST peaks highlights the effectiveness of LCo to distinguish Na^+ and Ca^{2+} in solution. An additional CEST peak at 11 ppm observed for **1** + Ca^{2+} likely stems from a coordinated H_2O molecule. Carboxamide exchange rates were estimated by the Omega plot method[22] as k_{ex} 4.0(5) × 10^2, 3.0(6) × 10^2 and 2.4(2) × 10^2 s^{-1} for **1**, **1** + Na^+, and **1** + Ca^{2+}, respectively (see Figure 5.6), consistent with reported carboxamide-based PARACEST

agents.[9, 10] To our knowledge, **1** represents the first example of a PARACEST-based calcium probe.

To evaluate the ability of **1** to enable ratiometric quantitation of Ca^{2+} concentration under physiological conditions, CEST spectra were collected at 37 °C for a solution containing 2.0 mM **1**, 150 mM NaCl, and 50 mM HEPES, buffered at pH 7.4, upon incremental addition of $Ca(NO_3)_2 \cdot 4H_2O$. In the absence of Ca^{2+}, a single CEST peak at 69 ppm was observed, indicating complete formation of $[LCoNa]^+$. Upon addition of Ca^{2+}, a new peak appeared at 80 ppm and monotonically increased in intensity until reaching saturation at $[Ca^{2+}]$ = 3.13 mM. Due to partial overlap with the peak at 80 ppm, the CEST intensity at 69 ppm first increased to $[Ca^{2+}]$ = 1.00 mM, then decreased until saturating at $[Ca^{2+}]$ = 3.13 mM (see Figure 5.7, upper). The appearance of the CEST peak at 80 ppm indicates selective binding of Ca^{2+} over Na^+ under physiological conditions.[14] Importantly,

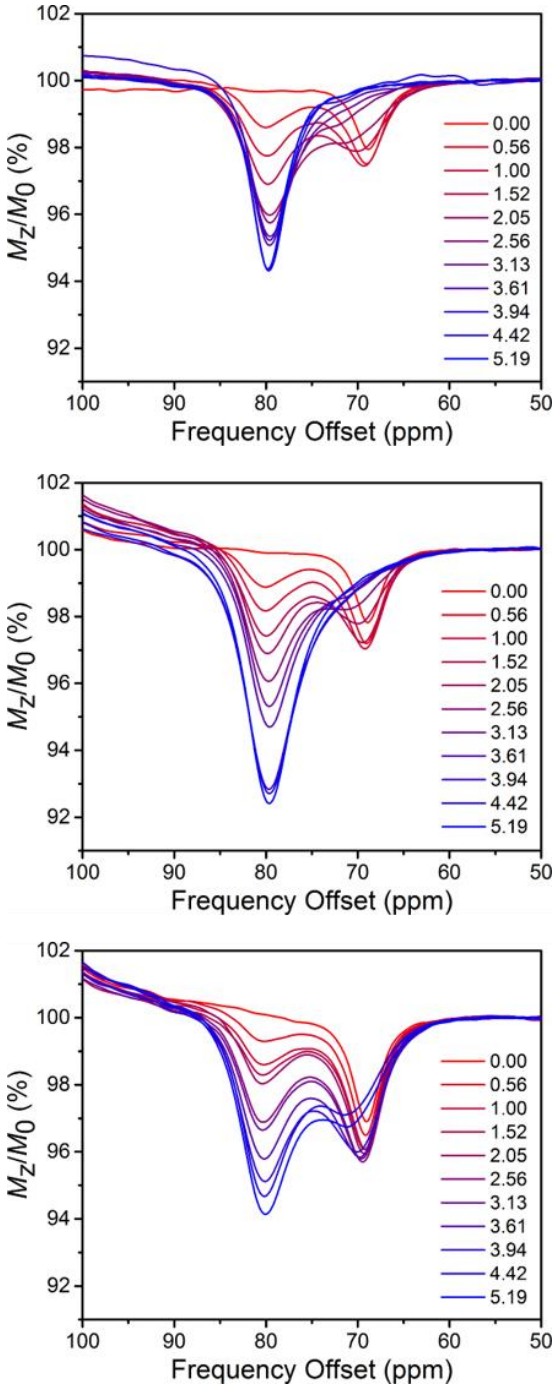

Figure 5.8 Stacked CEST spectra of solutions containing 2.8 (upper), 5.6 (middle) and 11 (lower) mM of **1**, 150 mM NaCl, 50 mM of HEPES with various concentrations of $Ca(NO_3)_2$, ranging from 0 to 5.19 mM. Legend: the concentration of Ca^{2+} in mM.

the saturation in intensity of this peak at $[Ca^{2+}]$ = 3.13 mM rather than 2.00 mM suggests that the selectivity is modest enough to allow for an equilibrium between $[LCoNa]^{+}$ and $[LCoCa]^{2+}$, a prerequisite for ratiometric quantitation.

To assess the influence of probe concentration on CEST, variable-$[Ca^{2+}]$ CEST spectra were collected for various concentrations of **1** (see Figure 5.8). The peak intensities at 80 and 69 ppm change as the concentrations of **1** change, demonstrating the shortcoming of detecting Ca^{2+} solely based on CEST intensities. Nevertheless, plotting the ratio of intensities at 80 and 69 ppm vs $[Ca^{2+}]$ (see Figure 5.7, lower) provides a concentration-independent measure. Indeed, data for $[Ca^{2+}] < 3$ mM can be fit using the following empirical exponential model:

$$CEST_{80\ ppm}/CEST_{69\ ppm} = \exp([Ca^{2+}] - x);$$

where x = 0.92(4), 0.90(6), 1.6(1) and 2.8(2) for 2.0, 2.8, 5.6 and 11 mM of **1**, respectively.

Despite a 40% difference in concentration, the equations for 2.0 and 2.8 mM of **1** are statistically indistinguishable (see Figure 5.7, lower inset). However, those for 5.6 and 11 mM **1** are significantly different,

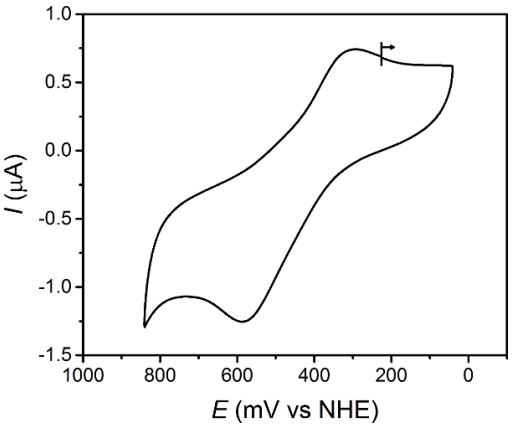

Figure 5.9 Cyclic voltammogram of **1** in a solution containing 100 mM NMe_4Cl and 50 mM HEPES buffered at pH 7.4.

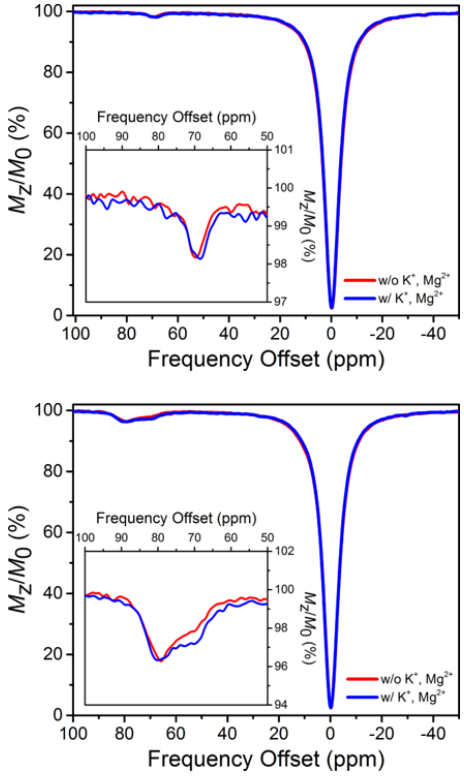

Figure 5.10 CEST spectra of samples containing 2 mM of **1**, 150 mM of NaCl and 50 mM of HEPES buffered at pH 7.4 in the absence (red) or presence (blue) of 4 mM KNO_3 and 0.2 mM $Mg(NO_3)_2$.

suggesting that $[LCoNa]^+$ and $[LCoCa]^{2+}$ are not in equilibrium, likely due to strong Ca^{2+} binding at higher concentrations of **1** (≥ 5.6 mM). These results establish the validity of using the CEST intensity ratio to quantitate Ca^{2+} concentration in a regime where the concentration of **1** is sufficiently low to allow an equilibrium between $[LCoNa]^+$ and $[LCoCa]^{2+}$.

5.4 Conclusion and Outlook

The positive $Co^{II/III}$ redox potential of **1** and minimal interference from K^+ and Mg^{2+} under physiological conditions (see Figures 5.9–10).[14] further support its utility in calcium sensing. While the low CEST intensities of this first-generation probe preclude its use in *in vivo* applications, the foregoing proof-of-concept study demonstrates a new approach to ratiometrically determine Ca^{2+} concentration by MR. Future efforts will focus on increasing signal intensities through chemical modifications of the ligand.

REFERENCES

References for Chapter One

(1) Lauffer, R. B. *Chem. Rev.* **1987**, *87*, 901.

(2) (a) Carava, P.; Ellison, J. J.; McMurry, T. J.; Lauffer, R. B. *Chem. Rev.* **1999**, *99*, 2293. (b) Caravan, P. *Chem. Soc. Rev.* **2006**, *35*, 512. (c) Yoo, B.; Pagel, M. D. *Front. Biosci.* **2008**, *13*, 1733. (d) Major, J. L.; Meade, T. J. *Acc. Chem. Res.* **2009**, *42*, 893.

(3) Werner, E. J.; Datta, A.; Jocher, C. J.; Raymond, K. N. *Angew. Chem. Int. Ed.* **2008**, *47*, 8568.

(4) Selected references: (a) Xu, J.; Franklin, S. J.; Whisenhunt, D. W.; Raymond, K. N. *J. Am. Chem. Soc.* **1995**, *117*, 7245 (b) Tóth, É.; Bürai, L.; Brucher, E.; Merbach, A. E. *J. Chem. Soc. Dalton Trans.* **1997**, 1587. (c) Cohen, S. M.; Xu, J. D.; Radkov, E.; Raymond, K. N.; Botta, M.; Barge, A.; Aime, S. *Inorg. Chem.* **2000**, *39*, 5747. (d) Johnson, A. R.; O'Sulliva, B.; Raymond, K. N. *Inorg. Chem.* **2000**, *39*, 2652. (e) Thompson, M. K.; Botta, M.; Nicolle, G.; Helm, L.; Aime, S.; Merbach, A. E.; Raymond, K. N. *J. Am. Chem. Soc.* **2003**, *125*, 14284. (f) Helm, L; Merbach, A. E. *Chem. Rev.* **2005**, *105*, 1923. (g) Pierre, V. C.; Botta, M.; Aime, S.; Raymond, K. N. *J. Am. Chem. Soc.* **2006**, *128*, 5344. (h) Pierre, P. C.; Botta, M.; Aime, S.; Raymond, K. N. *Inorg. Chem.* **2006**, *45*, 8355.

(5) Ward, K. M.; Aletras, A. H.; Balaban, R. S. *J. Magn. Reson.* **2000**, *143*, 79

(6) Selected references: (a) Zhang, S.; Winter, P.; Wu, K.; Sherry, A. D. *J. Am. Chem. Soc.* **2001**, *123*, 1517. (b) Zhang, S.; Merritt, M.; Woessner, D. E.; Lenkinski, R. E.; Sherry, A. D. *Acc. Chem. Res.* **2003**, *36*, 783. (c) Zhou, J.; van Zijl, P. C. M. *Prog. Nucl. Magn. Reson. Spectrosc.* **2006**, *48*, 109. (d) Ali, M. M.; Liu, G.; Shah, T.; Flask, C. A.; Pagel, M. D. *Acc. Chem. Res.* **2009**, *42*, 915. (e) Viswanathan, S.; Kovacs, Z.; Green, K. N.; Ratnakar, S. J.; Sherry, A. D. *Chem. Rev.* **2010**, *110*, 2960. (f) Terreno, E.; Castelli, D. D.; Viale, A.; Aime, S. *Chem. Rev.* **2010**, *110*, 3019.

(7) Selected references: (a) Zhang, S.; Michaudet, L.; Burgess, S.; Sherry, A. D. *Angew. Chem. Int. Ed.* **2002**, *41*, 1919. (b) Aime, S; Castelli, D. D.; Terreno, E. *Angew. Chem. Int. Ed.* **2002**, *41*, 4334. (c) Terreno, E.; Castelli, D. D.; Cravotto, G.; Milone, L.; Aime, S. *Invest. Radiol.* **2004**, *39*, 235. (d) Woods, M.; Woessner, D. E.; Zhao, P.; Pasha, A.; Yang, M.-Y.; Huang, C.-H.; Vasalitiy, O.; Morrow, J. R.; Sherry, A. D. *J. Am. Chem. Soc.* **2006**, *128*, 10155.

(8) Zhang, S.; Sherry, A. D. *J. Solid State Chem.* **2003**, *171*, 38.

(9) Selected references: (a) Dorazio, S. J.; Tsitovich, P. B.; Siter, K. E.; Spernyak, J. A.; Morrow, J. R. *J. Am. Chem. Soc.* **2011**, *133*, 14154. (b) Tsitovich, P. B.; Morrow, J. R. *Inorg. Chim. Acta* **2012**, *393*, 3. (c) Olatunde, A. O.; Dorazio, S. J.; Spernyak, J. A.; Morrow, J. R. *J. Am. Chem. Soc.* **2012**, *134*, 18503. (d) Dorazio, S. J.; Morrow, J. R. *Inorg. Chem.* **2012**, *51*, 7448. (e) Dorazio, S. J.; Olatunde, A. O.; Spernyak, J. A.; Morrow, J. R. *Chem. Commun.* **2013**, *49*, 10025.

(10) Selected references: (a) Moats, R. A.; Fraser, S. E.; Meade, T. J. *Angew. Chem., Int. Ed.* **1997**, *36*, 726. (b) Woods, M.; Zhang, S.; Ebron, V. H.; Sherry, A. D. *Chem. Eur. J.* **2003**, *9*, 4634. (c) Duimstra, J. A.; Femia, F. J.; Meade, T. J. *J. Am. Chem. Soc*. **2005**, *127*, 12847. (d) Tóth, É.; Bolskar, R. D.; Borel, A.; González, G.; Helm, L.; Merbach, A. E.; Sitharaman, B.; Wilson, L. J. *J. Am. Chem. Soc.* **2005**, *127*, 799. (e) Que, E. L.; Chang, C. J. *J. Am. Chem. Soc.* **2006**, *128*, 15942. (f) Kálmán, F. K.; Woods, M.; Caravan, P.; Jurek, P.; Spiller, M.; Tircsó, G.; Király, R.; Brücher, E.; Sherry, A. D. *Inorg. Chem.* **2007**, *46*,

5260. (g) Giardiello, M.; Lowe, M. P.; Botta, M. *Chem. Commun.* **2007**, *39*, 4044. (h) Esqueda, A. C.; López, J. A.; Andreu-de-Riquer, G.; Alvarado-Monzón, J. C.; Ratnakar, J.; Lubag, A. J.; Sherry, A. D.; De León-Rodríguez, L. M. *J. Am. Chem. Soc.* **2009**, *131*, 11387. (i) Keliris, A.; Mamedov, I.; Hagberg, G. E.; Logothetis, N. K.; Scheffler, K.; Engelmann, J. *Contrast Media Mol. Imaging.* **2012**, *7*, 478 (j) Matosziuk, L. M.; Leibowitz, J. H.; Heffern, M. C.; MacRenaris, K. W.; Ratner, M. A.; Meade, T. J. *Inorg. Chem.* **2013**, *52*, 12250. (k) Wang, Y.; Song, R.; Guo, K.; Meng, Q.; Zhang, R.; Kong, X.; Zhang, Z. *Dalton Trans.* **2016**, *45*, 17616. (l) MacRenaris, K. W.; Ma, Z.; Krueger, R. L.; Carney, C. E.; Meade, T. J. *Bioconj. Chem.* **2016**, *27*, 465.

(11) Ekanger, L. A.; Polin, L. A.; Shen, Y.; Haacke, E. M.; Martin, P. D.; Allen, M. J. *Angew. Chem. Int. Ed.* **2015**, *54*, 14398.

(12) (a) Tsitovich, P. B.; Spernyak, J. A.; Morrow, J. R. *Angew. Chem. Int. Ed.* **2013**, *52*, 13997. (b) Jeon, I.-R.; Park, J. G.; Haney, C. R.; Harris, T. D. *Chem. Sci.* **2014**, *5*, 2461

References for Chapter Two

(1) (a) Zhang, S.; Winter, P.; Wu, K.; Sherry, A. D. *J. Am. Chem. Soc.* **2001**, *123*, 1517. (b) Zhang, S.; Merritt, M.; Woessner, D. E.; Lenkinski, R. E.; Sherry, A. D. *Acc. Chem. Res.* **2003**, *36*, 783. (c) Zhou, J.; van Zijl, P. C. M. *Prog. Nucl. Magn. Reson. Spectrosc.* **2006**, *48*, 109. (d) Ali, M. M.; Liu, G.; Shah, T.; Flask, C. A.; Pagel, M. D. *Acc. Chem. Res.* **2009**, *42*, 915. (e) Viswanathan, S.; Kovacs, Z.; Green, K. N.; Ratnakar, S. J.; Sherry, A. D. *Chem. Rev.* **2010**, *110*, 2960. (f) Terreno, E.; Castelli, D. D.; Viale, A.; Aime, S. *Chem. Rev.* **2010**, *110*, 3019.

(2) Ward, K. M.; Aletras, A. H.; Balaban, R. S. *J. Magn. Reson.* **2000**, *143*, 79.

(3) Selected references: (a) Zhang, S.; Michaudet, L.; Burgess, S.; Sherry, A. D. *Angew. Chem. Int. Ed.* **2002**, *41*, 1919. (b) Aime, S; Castelli, D. D.; Terreno, E. *Angew. Chem. Int. Ed.* **2002**, *41*, 4334. (c) Terreno, E.; Castelli, D. D.; Cravotto, G.; Milone, L.; Aime, S. *Invest. Radiol.* **2004**, *39*, 235. (d) Woods, M.; Woessner, D. E.; Zhao, P.; Pasha, A.; Yang, M.-Y.; Huang, C.-H.; Vasalitiy, O.; Morrow, J. R.; Sherry, A. D. *J. Am. Chem. Soc.* **2006**, *128*, 10155.

(4) Selected references: (a) Dorazio, S. J.; Tsitovich, P. B.; Siter, K. E.; Spernyak, J. A.; Morrow, J. R. *J. Am. Chem. Soc.* **2011**, *133*, 14154. (b) Tsitovich, P. B.; Morrow, J. R. *Inorg. Chim. Acta* **2012**, *393*, 3. (c) Olatunde, A. O.; Dorazio, S. J.; Spern-yak, J. A.; Morrow, J. R. *J. Am. Chem. Soc.* **2012**, *134*, 18503. (d) Dorazio, S. J.; Morrow, J. R. *Inorg. Chem.* **2012**, *51*, 7448. (e) Dorazio, S. J.; Olatunde, A. O.; Spernyak, J. A.; Morrow, J. R. *Chem. Commun.* **2013**, *49*, 10025. (f) Tsitovich, P. B.; Spernyak, J. A.; Morrow, J. R. *Angew. Chem. Int. Ed.* **2013**, *52*, 13997. (g) Jeon, I.-R.; Park, J. G.; Haney, C. R.; Harris, T. D. *Chem. Sci.* **2014**, *5*, 2461.

(5) Woods, M.; Woessner, D. E.; Sherry, A. D. *Chem. Soc. Rev.* **2006**, *35*, 500.

(6) Selected references: (a) Zhang, S.; Trokowski, R.; Sherry, A. D. *J. Am. Chem. Soc.* **2003**, *125*, 15288. (b) Zhang, S.; Malloy, C. R.; Sherry, A. D. *J. Am. Chem. Soc.* **2005**, *127*, 17572. (c) Trokowski, R.; Ren, J.; Kálmán, F. K.; Sherry, A. D. *Angew. Chem. Int. Ed.* **2005**, *44*, 6920. (d) Que, E. L.; Chang, C. J. *J. Am. Chem. Soc.* **2006**, *128*, 15942. (e) Huang, C.-H.; Morrow, J. R. *J. Am. Chem. Soc.* **2009**, *131*, 4206. (f) Que, E. L.; Chang, C. J. *Chem. Soc. Rev.* **2010**, *39*, 51. (g) Ratnakar, S. J.; Viswa-nathan, S.; Kovacs, Z.; Jindal, A. K.; Green, K. N.; Sherry, A. D. *J. Am. Chem. Soc.* **2012**, *134*, 5798. (h) Hingorani, D. V.; Randtke, E. A.; Pagel, M. D. *J. Am. Chem. Soc.* **2013**, *135*, 6396. (i) Ekanger, L. A.; Ali, M. M.; Allen, M. J. *Chem. Commun.* **2014**, *50*, 14835.

(7) (a) Bertini, I.; Luchinat, C. *NMR of Paramagnetic Molecules in Biological Systems*; The Benjamin/Cummings Publishing Com-pany, Inc.: Menlo Park, 1986. (b) Bertini, I.; Luchinat, C. *Coord. Chem. Rev.* **1996**, *150*, 1. (c) Bertini, I.; Luchinat, C.; Parigi, G. *Solution NMR of Paramagnetic Molecules: Applica-tions to Metallobiomolecules and Models*; Elsevier Science B. V.: Amsterdam, 2001.

(8) (a) Nishida, Y.; Shimo, H.; Maehara, H.; Kida, S. *J. Chem. Soc. Dalton Trans.* **1985**, 1945. (b) Murthy, N. N.; Karlin, K. D.; Bertini, I.; Luchinat, C. *J. Am. Chem. Soc.* **1997**, *119*, 2156. (c) Siluvai, G. S.; Murthy, N. N. *Polyhedron* **2009**, *28*, 2149.

(9) Trost, B. M.; Yeh, V. S. C.; Ito, H.; Bremeyer, N. *Org. Lett.* **2002**, *4*, 2621.

(10) Johnson, H. E.; Crosby, D. G. *J. Org. Chem.* **1962**, *27*, 798.

(11) APEX2, v. 2009 ; Bruker Analytical X-Ray Systems, Inc: Madison, WI, 2009
(12) Sheldrick, G. *SADABS, Program for Empirical Absorption Correction of Area Detector Data;* University of Göttingen, Germany, 1996.
(13) Sheldrick, G. M. SHELXTL, Version 6.12; Bruker Analytical X-ray Systems, Inc.: Madison, WI, 2000
(14) Sheldrick, G. M. *Acta Crystallogr., Sect. A: Found. Adv.* **2015**, *71*, 3.
(15) van der Sluis, P.; Spek, A. L. *Acta Crystallogr., Sect. A: Found. Crystallogr.* **1990**, *A46*, 194.
(16) Dixon, W. T.; Ren, J.; Lubag, A. J. M.; Ratnakar, J.; Vinogradov, E.; Hancu, I.; Lenkinski, R. E.; Sherry, A. D. *Magn. Reson. Med.* **2010**, *63*, 625.
(17) Sawyer, D. T.; Sobkowiak, A. J.; Roberts, J. *Electrochemistry for Chemists*, 2nd ed.; John Wiley & Sons: New York, 1995.
(18) Kuzmič, P *Anal. Biochem.* **1996**, *237*, 260.
(19) These values correspond to the spin Hamiltonian $\hat{H} = -2J(\hat{S}_{Cu1}\cdot\hat{S}_{Cu2})$.
(20) Lee, D. H.; Im, J. H.; Son, S. U.; Chung, Y. K.; Hong, J.-I. *J. Am. Chem. Soc.* **2003**, *125*, 7752.
(21) Osório, R. E. H. M. B.; Peralta, R. A.; Bortoluzzi, A. J.; de Al-meida, V. R.; Szpoganicz, B.; Fischer, F. L.; Terenzi, H.; Man-grich, A. S.; Mantovani, K. M.; Ferreira, D. E. C.; Rocha, W. R.; Haase, W.; Tomkowicz, Z.; dos Anjos, A.; Neves, A. *Inorg. Chem.* **2012**, *51*, 1569.
(22) Torelli, S.; Belle, C.; Gautier-Luneau, I.; Pierre, J. L.; Saint-Aman, E.; Latour, J. M.; Le Pape, L.; Luneau, D. *Inorg. Chem.* **2000**, *39*, 3526.
(23) Baker, A. T. *J. Chem. Educ.* **1998**, *75*, 98.
(24) Note that the peak maxima in the UV/Visible spectra of **1** in both H_2O and 1:1 H_2O/glycerol are identical (see Figure 2.S9).
(25) (a) Magnetic susceptibility data were simulated using the pro-gram *MagProp: Tregenna-Piggott, P. L. W.; MagProp (part of the NIST DAVE software suite)*, version 2.0, 2008, http://www.ncnr.nist.gov/dave (b) Azuah, R. T.; Kneller, L. R.; Qiu, Y. M.; Tregenna-Piggott, P. L. W.; Brown, C. M.; Copley, J. R. D.; Dimeoo, R. M. *J. Res. Natl. Inst. Stand. Technol.* **2009**, *114*, 341.
(26) Tsitovich, P. B.; Bums, P. J.; McKay, A. M.; Morrow, J. R. *J. Inorg. Biochem.* **2014**, *133*, 143.

References for Chapter Three

(1) (a) *Redox in Biochemistry*, ed. Banerjee, R. John Wiley & Sons: Hoboken, 2008. (b) Chaiswing, L.; Oberley, T. D. *Antioxid. Redox Signal.* **2010**, *13*, 449. (c) Banerjee, R. *J. Biol. Chem.* **2012**, *287*, 4397.

(2) (a) Jones, D. P.; Carlson, J. L.; Mody, V. C. Jr; Cai, J.; Lynn, M. J.; Sternberg, P. Jr *Free Radical Biol. Med.* **2000**, *28*, 625. (b) Go, Y. -M.; Jones, D. P. *Methods Enzymol.* **2010**, *474*, 165.

(3) Lou, Z.; Li, P.; Han, K. *Acc. Chem. Res.* **2015**, *48*, 1358.

(4) Selected examples: (a) Jiang, S.; Moriarty-Craige, S. E.; Orr, M.; Cai, J.; Sternberg, P. Jr Jones, D. P. *Invest. Ophthalmol. Vis. Sci.* **2005**, *46*, 1054. (b) Chaiswing, L.; Zhong, W.; Cullen, J. J.; Oberley, L. W.; Oberley, T. D. *Cancer Res.* **2008**, *68*, 5820. (c) Chaiswing, L.; Zhong, W.; Liang, Y.; Jones, D. P.; Oberley, T. D. *Free Radic. Biol. Med.* **2012**, *52*, 452. (d) Iyer, S. S.; Ramirez, A. M.; Ritzenthaler, J. D.; Torres-Gonzalez, E.; Rose-Page, S.; Mora, A. L.; Brigham, K. L.; Jones, D. P.; Roman, J.; Rojas, M. *Am. J. Physiol. Lung Cell Mol. Physiol.* **2009**, *296*, 37.

(5) Wang, B.; Li, P.; Yu, F.; Chen, J.; Qu, Z.; Han, K. *Chem. Commun.* **2013**, *49*, 5790.

(6) (a) Lauffer, R. B. *Chem. Rev.* **1987**, *87*, 901. (b) Caravan, P.; Ellison, J. J.; McMurry, T. J.; Lauffer, R. B. *Chem. Rev.* **1999**, *99*, 2293. (c) Caravan, P. *Chem. Soc. Rev.* **2006**, *35*, 512.

(7) (a) Aime, S.; Botta, M.; Gianolio, E.; Terreno, E. *Angew. Chem. Int. Ed.* **2000**, *39*, 747. (b) Krohn, K. A.; Link, J. M.; Mason, R. P. *J. Nucl. Med.* **2008**, *49*, 129S. (c) Tsitovich, P. B.; Spernyak, J. A.; Morrow, J. R. *Angew. Chem. Int. Ed.* **2013**, *52*, 13997. (d) Ekanger, L. A.; Polin, L. A.; Shen, Y.; Haacke, E. M.; Martin, P. D.; Allen, M. J. *Angew. Chem. Int. Ed.* **2015**, *54*, 14398. (e) Xie, D.; King, T. L.; Banerjee, A.; Kohli, V.; Que, E. L. *J. Am. Chem. Soc.* **2016**, *138*, 2937.

(8) Yu, M.; Ambrose, S. L.; Whaley, Z. L.; Fan, S.; Gorden, J. D.; Beyers, R. J.; Schwartz, D. D.; Goldsmith, C. R. *J. Am. Chem. Soc.* **2014**, *136*, 12836.

(9) (a) Jagadish, B.; Guntle, G. P.; Zhao, D.; Gokhale, V.; Ozumerzifon, T. J.; Ahad, A. M.; Mash, E. A.; Raghunand, N.; *J. Med. Chem.* **2012**, *55*, 10378. (b) Loving, G. S.; Mukherjee, S.; Caravan, P. *J. Am. Chem. Soc.* **2013**, *135*, 4620.

(10) Ratnakar, S. J.; Viswanathan, S.; Kovacs, Z.; Jindal, A. K.; Green, K. N.; Sherry, A. D. *J. Am. Chem. Soc.* **2012**, *134*, 5798.

(11) Que, E. L.; Chang, C. J. *Chem. Soc. Rev.* **2010**, *39*, 51.

(12) (a) Zhang, S.; Winter, P.; Wu, K.; Sherry, A. D. *J. Am. Chem. Soc.* **2001**, *123*, 1517. (b) Zhang, S.; Merritt, M.; Woessner, D. E.; Lenkinski, R. E.; Sherry, A. D. *Acc. Chem. Res.* **2003**, *36*, 783. (c) Zhou, J.; van Zijl, P. C. M. *Prog. Nucl. Magn. Reson. Spectrosc.* **2006**, *48*, 109. (d) Ali, M. M.; Liu, G.; Shah, T.; Flask, C. A.; Pagel, M. D. *Acc. Chem. Res.* **2009**, *42*, 915. (e) Viswanathan, S.; Kovacs, Z.; Green, K. N.; Ratnakar, S. J.; Sherry, A. D. *Chem. Rev.* **2010**, *110*, 2960. (f) Terreno, E.; Castelli, D. D.; Viale, A.; Aime, S. *Chem. Rev.* **2010**, *110*, 3019. (g) Tsitovich, P. B.; Burns, P. J.; McKay, A. M.; Morrow, J. R. *J. Inorg. Biochem.* **2014**, *133*, 143.

(13) (a) Bertini, I.; Luchinat, C. *NMR of Paramagnetic Molecules in Biological Systems* The Benjamin/Cummings Publishing Company, Inc.: Menlo Park, 1986. (b) Bertini, I.; Luchinat, C. *Coord. Chem. Rev.* **1996**, *150*, 1. (c) Bertini, I.; Luchinat, C.; Parigi, G. *Solution NMR of Paramagnetic Molecules: Applications to Metallobiomolecules and Models* Elsevier Science B. V.: Amsterdam, 2001.

(14) Du, K.; Harris, T. D. *J. Am. Chem. Soc.* **2016**, *138*, 7804.

(15) APEX2, v. 2009 ; Bruker Analytical X-Ray Systems, Inc: Madison, WI, 2009.

(16) Sheldrick, G. SADABS, Program for Empirical Absorption Correction of Area Detector Data. University of Göttingen, Germany. 1996.

(17) Sheldrick, G. M. SHELXTL, Version 6.12; Bruker Analytical X-ray Systems, Inc.: Madison, WI, 2000.

(18) Sheldrick, G. M. *Acta Crystallogr., Sect. A: Found. Adv.* **2015**, *71*, 3.

(19) Dixon, W. T.; Ren, J.; Lubag, A. J. M.; Ratnakar, J.; Vinogradov, E.; Hancu, I.; Lenkinski, R. E.; Sherry, A. D. *Magn. Reson. Med.* **2010**, *63*, 625.

(20) Bain, G. A.; Berry, J. F. *J. Chem. Ed.* **2008**, *85*, 532.

(21) (a) Magnetic susceptibility data were simulated using the program MagProp: P. L. W. Tregenna-Piggott, *MagProp (part of the NIST DAVE software suite)*, version 2.0, 2008, http://www.ncnr.nist.gov/dave. (b) Azuah, R. T.; Kneller, L. R.; Qiu, Y. M.; Tregenna-Piggott, P. L. W.; Brown, C. M.; Copley, J. R. D.; Dimeoo, R. M. *J. Res. Natl. Inst. Stand. Technol.* **2009**, *114*, 341.

(22) (a) Evans, D. F. *J. Chem. Soc.* **1959**, 2003. (b) Schubert, E. M. *J. Chem. Educ.* **1992**, *69*, 61.

(23) Sawyer, D. T.; Sobkowiak, A. J.; Roberts, J. *Electrochemistry for Chemists*, 2nd ed.; John Wiley & Sons: New York, 1995

(24) (a) Kestner, N. R.; Logan, J.; Jortner, J. *J. Phys. Chem.* **1974**, *78*, 2148. (b) Hopfield, J. J. *Proc. Natl. Acad. Sci. U. S. A.* **1974**, *71*, 3640. (c) Meyer, T. J. *Chem. Phys. Lett.* **1979**, *64*, 417. (d) A. S. Borovik, V. Papaefthymiou, L. F. Taylor, O. P. Anderson, L. Que Jr, *J. Am. Chem. Soc.* **1989**, *111*, 6183.

(25) Mashuta, M. S.; Webb, R. J.; Oberhausen, K. J.; Richardson, J. F.; Buchanan, R. M.; Hendrickson, D. N. *J. Am. Chem. Soc.* **1989**, *111*, 2745.

(26) (a) Borovik, A. S.; Papaefthymiou, V.; Taylor, L. F.; Anderson, O. P.; Que, L. Jr *J. Am. Chem. Soc.* **1989**, *111*, 6183. (b) Lambert, E.; Chabut, B.; Chardon-Noblat, S.; Deronzier, A.; Chottard, G.; Bousseksou, A.; Tuchagues, J.-P.; Laugier, J.; Bardet, M.; Latour, J.-M. *J. Am. Chem. Soc.* **1997**, *119*, 9424. (c) Gouré, E.; Carboni, M.; Troussier, A.; Lebrun, C.; Pécaut, J.; Jacquot, J.-F.; Dubourdeaux, P.; Clémancey, M.; Blondin, G.; Latour, J.-M. *Chem. Eur. J.* **2015**, *21*, 8064. (d) Mashuta, M.; Webb, R. J.; McCusker, J. K.; Schmitt, E. A.; Oberhausen, K. J.; Richardson, J. F.; Buchanan, R. M.; Hendrickson, D. N. *J. Am. Chem. Soc.* **1992**, *114*, 3815.

(27) Fultz, B. *Characterization of Material* ed. Kaufmann, E. John Wiley: New York, 2011, pp. 1-21.

(28) Borovik, A. S.; Que, L. Jr *J. Am. Chem. Soc.* **1988**, *110*, 2345.

(29) Hush, N. S. *Prog. Inorg. Chem.* **1967**, *8*, 391.
(30) (a) Kestner, N. R.; Logan, J.; Jortner, J. *J. Phys. Chem.* **1974**, *78*, 2148; (b) Hopfield, J. J. *Proc. Natl. Acad. Sci. U. S. A.* **1974**, *71*, 3640; (c) Meyer, T. J. *Chem. Phys. Lett.* **1979**, *64*, 417.
(31) Murch, B. P.; Bradley, F. C.; Que, L. Jr *J. Am. Chem. Soc.* **1986**, *108*, 5028.
(32) (a) Magnetic susceptibility data were simulated using the program MagProp: Tregenna-Piggott, P. L. W. *MagProp (part of the NIST DAVE software suite), version 2.0, 2008*, http://www.ncnr.nist.gov/dave. (b) Azuah, R. T.; Kneller, L. R.; Qiu, Y. M.; Tregenna-Piggott, P. L. W.; Brown, C. M.; Copley, J. R. D.; Dimeoo, R. M. *J. Res. Natl. Inst. Stand. Technol.* **2009**, *114*, 341.
(33) (a) Tsitovich, P. B.; Morrow, J. R. *Inorg. Chim. Acta* **2012**, *393*, 3; (b) Dorazio, S. J.; Morrow, J. R. *Inorg. Chem.* **2012**, *51*, 7448; (c) Olatunde, A. O.; Bond, C. J.; Dorazio, S. J.; Cox, J. M.; Benedict, J. B.; Daddario, M. D.; Spernyak, J. A.; Morrow, J. R. *Chem. Eur. J.* **2015**, *21*, 18290.
(34) Wan, Q. J.; Kubáň, P.; Tanyanyiwa, J.; Rainelli, A.; Hauser, P. C. *Anal. Chim. Acta* **2004**, *525*, 11.

References for Chapter Four

(1) Major, J. L.; Meade, T. J. *Acc. Chem. Res.* **2009**, *42*, 893.
(2) Heffern, M. C.; Matosziuk, L. M.; Meade, T. J. *Chem. Rev.* **2014**, *114*, 4496.
(3) Louie, A. Y.; Huber, M. M.; Ahrens, E. T.; Rothbacher, U.; Moats, R.; Jacobs, R. E.; Fraser, S. E.; Meade, T. J. *Nat. Biotechnol.* **2000**, *18*, 321.
(4) Duimstra, J. A.; Femia, F. J.; Meade, T. J. *J. Am. Chem. Soc.* **2005**, *127*, 12847.
(5) Li, W-H.; Fraser, S. E.; Meade, T. J. *J. Am. Chem. Soc.* **1999**, *121*, 1413.
(6) Caravan, P. *Chem. Soc. Rev.* **2006**, *35*, 512.
(7) Hingorani, D. V.; Bernstein, A. S.; Pagel, M. D. *Contrast Media Mol. Imaging.* **2015**, *10*, 245.
(8) Powell, D.H.; Ni Dhubhghaill, O.M.; Pubanz, D.; Helm, L.; Lebedev, Y.S.; Schlaepfer, W.; Merbach, A.E. *J. Am. Chem. Soc.* **1996**, *229*, 9333.
(9) Moats, R. A.; Fraser, S. E.; Meade, T. J. *Angew. Chem., Int. Ed.* **1997**, *36*, 726.
(10) Giardiello, M.; Lowe, M. P.; Botta, M. *Chem. Commun.* **2007**, *39*, 4044.
(11) Keliris, A.; Mamedov, I.; Hagberg, G. E.; Logothetis, N. K.; Scheffler, K.; Engelmann, J. *Contrast Media Mol. Imaging* **2012**, *7*, 478.
(12) Que, E. L.; Chang, C. J. *J. Am. Chem. Soc.* **2006**, *128*, 15942.
(13) MacRenaris, K. W.; Ma, Z.; Krueger, R. L.; Carney, C. E.; Meade, T. J. *Bioconj. Chem.* **2016**, *27*, 465.
(14) Matosziuk, L. M.; Leibowitz, J. H.; Heffern, M. C.; MacRenaris, K. W.; Ratner, M. A.; Meade, T. J. *Inorg. Chem.* **2013**, *52*, 12250.
(15) Esqueda, A. C.; López, J. A.; Andreu-de-Riquer, G.; Alvarado-Monzón, J. C.; Ratnakar, J.; Lubag, A. J.; Sherry, A. D.; De León-Rodríguez, L. M. *J. Am. Chem. Soc.* **2009**, *131*, 11387.
(16) Wang, Y.; Song, R.; Guo, K.; Meng, Q.; Zhang, R.; Kong, X.; Zhang, Z. *Dalton Trans.* **2016**, *45*, 17616.
(17) Woods, M.; Zhang, S.; Ebron, V. H.; Sherry, A. D. *Chem. Eur. J.* **2003**, *9*, 4634.
(18) Kálmán, F. K.; Woods, M.; Caravan, P.; Jurek, P.; Spiller, M.; Tircsó, G.; Király, R.; Brücher, E.; Sherry, A. D. *Inorg. Chem.* **2007**, *46*, 5260.
(19) Tóth, É.; Bolskar, R. D.; Borel, A.; González, G.; Helm, L.; Merbach, A. E.; Sitharaman, B.; Wilson, L. J. *J. Am. Chem. Soc.* **2005**, *127*, 799.
(20) Caravan, P.; Parigi, G.; Chasse, J. M.; Cloutier, N. J.; Ellison, J. J.; Lauffer, R. B.; Luchinat, C.; McDermid, S. A.; Spiller, M.; McMurry, T. J. *Inorg. Chem.* **2007**, *46*, 6632.
(21) Overoye-Chan, K.; Koerner, S.; Looby, R. J.; Kolodziej, A. F.; Zech, S. G.; Deng, Q.; Chasse, J. M.; McMurry, T. J.; Caravan, P. *J. Am. Chem. Soc.* **2008**, *130*, 6025.
(22) Song, Y.; Kohlmeir, E. K.; Meade, T. J. *J. Am. Chem. Soc.* **2008**, *130*, 6662.
(23) Vistain, L. F.; Rotz, M. W.; Rathore, R.; Preslar, A. T.; Meade, T. J. *Chem. Commun.* **2016**, *52*, 160.
(24) Ahrens, E.; Rothbächer, U.; Jacobs, R.; Fraser, S. *Proc. Natl. Acad. Sci. U. S. A.* **1998**, *95*, 8443.
(25) Lipari, G.; Szabo, A. *J. Am. Chem. Soc.* **1982**, *104*, 4546.
(26) Bloembergen, N.; Purcell, E. M.; Pound, R. V. *Phys. Rev.* **1948**, *73*, 679.
(27) Solomon, I. *Phys. Rev.* **1955**, *99*, 559.
(28) Bloembergen, N.; Morgan, L. *J. Chem. Phys.* **1961**, *34*, 842.

(29) Rast, S.; Borel, A.; Minto; Helm, L.; Belorizky, E.; Fries, P.H.; Merbach, A.E. *J. Am. Chem. Soc.* **2001**, *123*, 2637.
(30) Bertini, I.; Luchinat, C.; Parigi, G.; Ravera, E. *NMR of paramagnetic molecules in biological systems* 2nd ed.; Elsevir, 2017.
(31) Bertini, I.; Galas, O.; Luchiant, C.; Parigi, G.; Spina, G. *J. Magn. Reson.* **1998**, *130*, 33.
(32) Murthy, N.N.; Karlin, K.D.; Bertini, L.; Luchiant, C. *J. Am. Chem. Soc.* **1997**, *119*, 2156.
(33) Holz, R.C.; Bennett, B/; Chen, G.; Ming, L-J. *J. Am. Chem. Soc.* **1998**, *120*, 6329.
(34) Du, K.; Harris, T. D. *J. Am. Chem. Soc.* **2016**, *138*, 7804.
(35) Tóth, É.; Helm, L.; Merbach, A. E.; Hedinger, R.; Hegetschweiler, K.; Jánossy, A. *Inorg. Chem.* **1998**, *37*, 4104.
(36) Moriggi, L.; Aebischer, A.; Cannizzo, C.; Sour, A.; Borel, A.; Bünzli, J.-C. G.; Helm, L. *Dalton Trans.* **2009**, *12*, 2088.
(37) Koullourou, T.; Natrajan, L. S.; Bhavsar, H.; Pope, S. J.; Feng, J.; Narvainen, J.; Shaw, R.; Scales, E.; Kauppinen, R.; Ken-wright, A. M. *J. Am. Chem. Soc.* **2008**, *130*, 2178.
(38) Gómez, V.; Vendier, L.; Corbella, M.; Costes, J.-P. *Inorg. Chem.* **2012**, *51*, 6396.
(39) Costes, J.-P.; Dahan, F.; Dupuis, A.; Laurent, J.-P. *Inorg. Chem.* **1996**, *35*, 2400.
(40) Costes, J.-P.; Dahan, F.; Dupuis, A.; Laurent, J.-P. *Inorg. Chem.* **1997**, *36*, 3429.
(41) Yamaguchi, T.; Costes, J.-P.; Kishima, Y.; Kojima, M.; Sunatsuki, Y.; Bréfuel, N.; Tuchagues, J.-P.; Vendier, L.; Wernsdorfer, W. *Inorg. Chem.* **2010**, *49*, 9125.
(42) Bertini, I.; Galas, O.; Luchinat, C.; Parigi, G.; Spina, G. *J. Magn. Res.* **1998**, *130*, 33.
(43) Costes, J. P.; Donnadieu, B.; Gheorghe, R.; Novitchi, G.; Tuchagues, J. P.; Vendier, L. *Eur. J. Inorg. Chem.* **2008**, 5235.
(44) Romain, C.; Bennington, M.S.; White, A.J.P.; Williams, C.K.; Brooker, S. *Inorg. Chem.* **2015**, *54*, 11842.
(45) Stoll, S.; Schweiger, A. *J. Magn. Reson.* **2006**, *178*, 42.
(46) Magnetic susceptibility data were simulated using the program MagProp: Tregenna-Piggott, P. L. W.; MagProp (part of the NIST DAVE software suite), version 2.0, 2008, http://www.ncnr.nist.gov/dave.
(47) Azuah, R. T.; Kneller, L. R.; Qiu, Y.; Tregenna-Piggott, P. L.; Brown, C. M.; Copley, J. R.; Dimeo, R. M. *J. Res. Natl. Inst. Stand. Technol.* **2009**, *114*, 341.
(48) APEX2, v. 2009 ; Bruker Analytical X-Ray Systems, Inc: Madison, WI, 2009.
(49) Sheldrick, G. SADABS, Program for Empirical Absorption Correction of Area Detector Data. University of Göttingen, Germany. 1996.
(50) Sheldrick, G. M. SHELXTL, Version 6.12; Bruker Analytical X-ray Systems, Inc.: Madison, WI, 2000.
(51) Sheldrick, G. M. *Acta Crystallogr., Sect. A: Found. Adv.* **2015**, *71*, 3.
(52) Meyer, D.; Schaefer, M.; Bonnemain, B. *Invset. Radiol.* **1988**, *23*, S232.
(53) Micskei, K.; Helm, L.; Brucher, E.; Merbach, A. E. *Inorg. Chem.* **1993**, *32*, 3844.
(54) Weil, J. A.; Bolton, J. R. *Electron paramagnetic resonance: elementary theory and practical applications* John Wiley & Sons, 2007.
(55) Freed, J. H.; Bruno, G. V.; Polnaszek, C. F. *J. of Phys. Chem.* **1971**, *75*, 3385.

References for Chapter Five

(1) (a) Coleman, R. E. *Cancer Treat. Rev.* **2001**, *27*, 165. (b) Mundy, G. R. *Nat. Rev. Cancer* **2002**, *2*, 584. (c) Kyle, R. A.; Rajkumar, S. V. *N. Engl. J. Med.* **2004**, *351*, 1860.

(2) (a) Fraser, W. D. *Lancet* **2009**, *374*, 145. (b) Blaine, J.; Chonchol, M.; Levi, M. *Clin. J. Am. Soc. Nephrol.* **2015**, *10*, 1257.

(3) (a) Ralston, S. H. *N. Engl. J. Med.* **2013**, *368*, 644. (b) Tuck, S. P.; Layfield, R.; Walker, J.; Mekkayil, B.; Francis, R. *Rheumatology* **2017**, *56*, 2050.

(4) Minisola, S.; Pepe, J.; Piemonte, S.; Cipriani, C. *BMJ* **2015**, *350*, h2723.

(5) Zeigler, R. *J. Am. Soc. Nephrol.* **2001**, *12*, S3.

(6) Lauffer, R. B. *Chem. Rev.* **1987**, *87*, 901. (b) Caravan, P.; Ellison, J. J.; McMurry, T. J.; Lauffer, R. B. *Chem. Rev.* **1999**, *99*, 2293. (c) Caravan, P. *Chem. Soc. Rev.* **2006**, *35*, 512.

(7) (a) Li, W.; Fraser, S. E.; Meade, T. J. *J. Am. Chem. Soc.* **1999**, *121*, 1413. (b) Li, W.; Parigi, G.; Fragai, M.; Luchinat, C.; Meade, T. J. *Inorg. Chem.* **2002**, *41*, 4018. (c) Atanasijevic, T.; Shusteff, M.; Fam, P.; Jasanoff, A. *Proc. Natl. Acad. Sci. U. S. A.* **2006**, *103*, 14707. (d) Mishra, A.; Fousková, P.; Angelovski, G.; Balogh, E.; Mishra, A. K.; Logothetis, N. K.; Tóth, É. *Inorg. Chem.* **2008**, *47*, 1370. (e) Dhingra, K.; Maier, M. E.; Beyerlein, M.; Angelovski, G.; Logothetis, N. K. *Chem. Commun.* **2008**, *0*, 3444. (f) Angelovski, G.; Fousková P.; Mamedov, I.; Canals, S.; Tóth, É.; Logothetis, N. K. *ChemBioChem* **2008**, *9*, 1729. (g) Que, E. L.; Chang, C. J. *Chem Soc. Rev.* **2010**, *39*, 51. (h) Mamedov, I.; Canals, S.; Henig, J.; Beyerlein, M.; Murayama, Y.; Mayer, H. A.; Logothetis, N. K.; Angelovski, G. *ACS Chem. Neurosci.* **2010**, *1*, 819. (i) Heffern, M. C.; Matosziuk, L. M.; Meade, T. J. *Chem. Rev.* **2014**, *114*, 4496. (j) Kadjane, P.; Platas-Iglesias, C.; Boehm-Sturm, P.; Truffault, V.; Hagberg, G. E.; Hoehn, M.; Logothetis, N. K.; Angelovski, G. *Chem. Eur. J.* **2014**, *20*, 7351. (k) MacRenaris K. W.; Ma, Z.; Krueger, R. L.; Carney, C. E.; Meade, T. J. *Bioconjug. Chem.* **2016**, *27*, 465.

(8) Selected references: (a) Zhang, S.; Michaudet, L.; Burgess, S.; Sherry, A. D. *Angew. Chem., Int. Ed.* **2002**, *41*, 1919. (b) Aime, S.; Castelli, D. D.; Terreno, E. *Angew. Chem., Int. Ed.* **2002**, *41*, 4334. (c) Terreno, E.; Castelli, D. D.; Cravotto, G.; Milone, L.; Aime, S. *Invest. Radiol*. **2004**, *39*, 235. (d) Woods, M.; Woessner, D. E.; Zhao, P.; Pasha, A.; Yang, M.-Y.; Huang, C.-H.; Vasalitiy, O.; Morrow, J. R.; Sherry, A. D. *J. Am. Chem. Soc.* **2006**, *128*, 10155.

(9) Selected references: (a) Dorazio, S. J.; Tsitovich, P. B.; Siter, K. E.; Spernyak, J. A.; Morrow, J. R. *J. Am. Chem. Soc.* **2011**, *133*, 14154. (b) Tsitovich, P. B.; Morrow, J. R. *Inorg. Chim. Acta* **2012**, *393*, 3. (c) Olatunde, A. O.; Dorazio, S. J.; Spernyak, J. A.; Morrow, J. R. *J. Am. Chem. Soc.* **2012**, *134*, 18503. (d) Dorazio, S. J.; Morrow, J. R. *Inorg. Chem.* **2012**, *51*, 7448. (e) Dorazio, S. J.; Olatunde, A. O.; Spernyak, J. A.; Morrow, J. R. *Chem. Commun.* **2013**, *49*, 10025. (f) Du, K.; Harris, T. D. *J. Am. Chem. Soc.* **2016**, *138*, 7804.

(10) (a) Tsitovich, P. B.; Spernyak, J. A.; Morrow, J. R. *Angew. Chem., Int. Ed.* **2013**, *52*, 13977. (b) Tsitovich, P. B.; Burns, P. J.; McKay, A. M.; Morrow, J. R. *J. Inorg. Biochem.* **2014**, *133*, 143. (c) Du, K.; Waters, E. A.; Harris, T. D. *Chem. Sci.* **2017**, *8*, 4424.

(11) (a) Liu, G.; Li, Y.; Sheth, V. R.; Pagel, M. D. *Mol. Imaging* **2012**, *11*, 47. (b) Sheth, V. R.; Li, Y.; Chen, L. Q.; Howison, C. M.; Flask, C. A.; Pagel, M. D. *Magn. Reson. Med.* **2012**, *67*, 760. (c) McVicar, N.; Li, A. X.; Suchý, M.; Hudson, R. H. E.; Menon, R. S.;

Bartha, R. *Magn. Reson. Med.* **2013**, *70*, 1016. (d) Delli Castelli, D.; Ferrauto, G.; Cutrin, J. C.; Terreno, E.; Aime, S. *Magn. Reson. Med.* **2014**, *71*, 326. (e) Rancan, G.; Delli Castelli, D.; Aime, S. *Magn. Reson. Med.* **2016**, *75*, 329. (f) Wu, Y.; Zhang, S.; Soesbe, T. C.; Yu, J.; Vinogradov, E.; Lenkinski, R. E.; Sherry, A. D. *Magn. Reson. Med.* **2016**, *75*, 2432. (g) Thorarinsdottir, A. E.; Du, K.; Collins, J. H. P.; Harris, T. D. *J. Am. Chem. Soc.* **2017**, *139*, 15836. (h) Thorarinsdottir, A. E.; Tatro, S. M.; Harris, T. D. *Inorg. Chem.* **2018**, DOI: 10.1021/acs.inorgchem.8b01896.

(12) (a) Terreno, E.; Delli Castelli, D.; Cravotto, G.; Milone, L.; Aime, S. *Invest. Radiol.* **2004**, *39*, 235. (b) Zhang, S.; Malloy, C. R.; Sherry, A. D. *J. Am. Chem. Soc.* **2005**, *127*, 17572. (c) Li, A. X.; Wojciechowski, F.; Suchý, M.; Jones, C. K.; Hudson, R. H. E.; Menon, R. S.; Bartha, R. *Magn. Reson. Med.* **2008**, *59*, 374. (d) Delli Castelli, D.; Terreno, E.; Aime, S. *Angew. Chem., Int. Ed.* **2011**, *50*, 1798. (e) Jeon, I.-R.; Park, J. G.; Haney, C. R.; Harris, T. D. *Chem. Sci*. **2014**, *5*, 2461.

(13) (a) Trokowski, R.; Ren, J.; Kálmán, F. K.; Sherry, A. D. *Angew. Chem., Int. Ed.* **2005**, *44*, 6920. (b) Srivastava, K.; Ferrauto, G.; Harris, S. M.; Longo, D. L.; Botta, M.; Aime, S.; Pierre, V. C. *Dalton Trans.* **2018**, DOI: 10.1039/C8DT01172A.

(14) (a) Wan, Q. J.; Kubáň, P.; Tanyanyiwa, J.; Rainelli, A.; Hauser, P. C. *Anal. Chim. Acta* **2004**, *525*, 11. (b) Le, T.; Bhushan, V.; Sochat, M.; Chavda, Y.; Zureick, A.; Kalani, M.; Kallianos, K. *First Aid for the USMLE Step 1: 2018 a Student-to-Student Guide*, 28th ed.; McGraw-Hill Education: New York, 2017.

(15) Bar-Shir, A.; Gilad, A. A.; Chan, K. W. Y.; Liu, G.; van Zijl, P. C. M.; Bulte, J. W. M.; McMahon, M. T. *J. Am. Chem. Soc.* **2013**, *135*, 12164.

(16) (a) van Staveren, C. J.; van Eerden, J.; van Veggel, F. C. J. M.; Harkema, S.; Reinhoudt, D. N. *J. Am. Chem. Soc.* **1988**, *110*, 4994. (b) Caneschi, A.; Sorace, L.; Casellato, U.; Tomasin, P.; Vigato, P. A. *Eur. J. Inorg. Chem.* **2004**, 3887. (c) Pierre, V. C.; Harris, S. M.; Pailloux, S. L. *Acc. Chem. Res.* **2018**, *51*, 342.

(17) (a) Bertini, I.; Luchinat, C. *NMR of Paramagnetic Molecules in Biological Systems*; The Benjamin/Cummings Publishing Company, Inc.: Menlo Park, 1986. (b) Bertini, I.; Luchinat, C. *Coord. Chem. Rev.* **1996**, *150*, 1. (c) Bertini, I.; Luchinat, C.; Parigi, G. *Solution NMR of Paramagnetic Molecules: Applications to Metallobiomolecules and Models*; Elsevier Science B.V.: Amsterdam, 2001.

(18) Bonger, K. M.; van den Berg, R. J. B. H. N.; Heitman, L. H.; IJzerman, A. P.; Oosterom, J.; Timmers, C. M.; Overkleeft, H. S.; van der Marel, G. A. *Bioorg. Med. Chem.* **2007**, *15*, 4841.

(19) van Staveren, C. J.; van Eerden, J.; van Veggel, F. C. J. M.; Harkema, S.; Reinhoudt, D. N. *J. Am. Chem. Soc.* **1988**, *110*, 4994.

(20) APEX2, v. 2009 ; Bruker Analytical X-Ray Systems, Inc: Madison, WI, 2009

(21) Sheldrick, G. *SADABS, Program for Empirical Absorption Correction of Area Detector Data;* University of Göttingen, Germany, 1996.

(22) Sheldrick, G. M. SHELXTL, Version 6.12; Bruker Analytical X-ray Systems, Inc.: Madison, WI, 2000

(23) Sheldrick, G. M. *Acta Crystallogr., Sect. A: Found. Adv.* **2015**, *71*, 3.

(24) Chilton, N. F.; Anderson, R. P.; Turner, L. D.; Soncini, A.; Murray, K. S. *J. Comput. Chem.* **2013**, *34*, 1164.

(25) (a) Cole, K. S.; Cole, R. H. *J. Chem. Phys.* **1941**, *9*, 341. (b) Boettcher, C. J. F. Theory of electric polarisation; Elsevier: Amsterdam, 1952. (c) Aubin, S. M.; Sun, Z.; Pardi, L.; Krzysteck, J.; Folting, K.; Brunel, L.-J.; Rheingold, A. L.; Christou, G.; Hendrickson, D. N. *Inorg. Chem.* **1999**, *38*, 5329.
(26) (a) Evans, D. F. *J. Chem. Soc.* **1959**, 2003; (b) Schubert, E. M. *J. Chem. Educ.* **1992**, *69*, 61.
(27) Bain, G. A. and Berry, J. F. *J. Chem. Ed.* **2008**, *85*, 532.
(28) Dixon, W. T.; Ren, J.; Lubag, A. J. M.; Ratnakar, J.; Vinogradov, E.; Hancu, I.; Lenkinski, R. E.; Sherry, A. D. *Magn. Reson. Med.*, **2010**, *63*, 625.
(29) Kuzmič, P *Anal. Biochem.* **1996**, *237*, 260.
(30) Sawyer, D. T.; Sobkowiak, A. J.; Roberts, J. *Electrochemistry for Chemists*, 2nd ed.; John Wiley & Sons: New York, 1995.
(31) (a) Reath, A. H.; Ziller, J. W.; Tsay, C.; Ryan, A. J.; Yang, J. Y. *Inorg. Chem.* **2017**, *56*, 3713. (b) Chantarojsiri, T.; Ziller, J. W.; Yang, J. Y. *Chem. Sci.* **2018**, *9*, 2567.
(32) (a) Shannon, R. D. *Acta Cryst.* **1976**, *A32*, 751. (b) Lang, P. F.; Smith, B. C. *Dalton Trans.* **2010**, *39*, 7786.
(33) Drew, M. G. B.; Harding, C. J.; McKee, V.; Morgan, G. G.; Nelson, J. *J. Chem. Soc., Chem. Commun.* **1995**, *0*, 1035.